공학박사학위논문

진동 생성 메커니즘을 고려한 초기 결함 단계의 베어링 진단 연구

A Study on Diagnosis of Bearings in Incipient Fault Stage Considering Vibration Generation Mechanisms

2023 년 2 월

서울대학교 대학원

기계항공공학부

김 근 수

진동 생성 메커니즘을 고려한 초기 결함 단계의 베어링 진단 연구

A Study on Diagnosis of Bearings in Incipient Fault Stage Considering Vibration Generation Mechanisms

지도교수 윤 병 동

이 논문을 공학박사 학위논문으로 제출함

2022 년 10 월

서울대학교 대학원

기계항공공학부

김 근 수

김근수의 공학박사 학위논문을 인준함

2022 년 12 월

위 원 장 : 김 도 년 (인)

부위원장 : 윤 병 동 (인)

위 원 : 김 윤 영 (인)

위 원 : 안 성 훈 (인)

위 원 : 윤 헌 준 (인)

Abstract

A Study on Diagnosis of Bearings in Incipient Fault Stage Considering Vibration Generation Mechanisms

Keunsu Kim
Department of Mechanical and Aerospace Engineering
The Graduate School
Seoul National University

The failure of rolling element bearings is a common fault in rotating machines. These failures can have catastrophic consequences, including fatal injuries and significant financial losses. To mitigate these risks, researchers have explored various ways to detect and prevent bearing failures as early as possible. One promising approach is the use of condition monitoring data; in this approach, vibration data has been found to be particularly effective for identifying and preventing potential failures. However, the use of vibration signals to diagnose bearings at the incipient fault stage is a challenging task, in part due to the gap between the controlled conditions under which research data is often generated and the actual field conditions in which these bearings operate. In particular, fault-related signals are weak and nonstationary; further, they are usually obscured by noise that arises from environmental factors. Additionally, these signals may be complicated or modulated, making them difficult to discern. To properly address these research issues, this dissertation aims at advancing two research thrusts focused on developing techniques for modeling and

analyzing vibration signals based on physical phenomena.

In Research Thrust 1, a quasi-periodic impulse train model with an impact force function is suggested to brtidge the gap between theory and reality. In this research, a pseudo second-order cyclostationary signal is modeled using the quasi-periodic impulse train model. In order to simulate the dynamic response of a system, considering the physical behaviors in bearings, the impact force function that reflects the change in contact stress is used. Finally, the proposed model is validated by performing signal processing on the synthesized signal, including simulation of the proposed model. The result confirm that an appropriate preprocessing process is essential to diagnose bearing failure at the incipient failure stage, further, that finding the frequency band that contains the failure information is essential for performance improvement.

In Research Thrust 2, a new feature extraction method is proposed for bearing diagnosis using vibration signals, namely the linear power normalized cepstral coefficients (LPNCC). The proposed approach is designed to enhance the bearing signal, which is buried in noise that arises from environmental effects, and which contains mechanical phenomena. The proposed method consists of two sequentially executed steps: 1) extraction of the LPNCC and 2) demodulation analysis that is performed by examining the squared envelope spectra (SES). Combined, this approach is called LPNCC-SES. The performance of the proposed method is examined by applying it to both simulation data and experimental cases. The results show a high level of accuracy and robustness in the diagnostic capabilities of the method, making it suitable for use in maintenance and diagnostic routines.

Keywords: Rolling Element Bearing
Bearing Signal Model
Bearing Diagnostics
Vibration Generation Mechanism
Incipient Fault Stage

Student Number: 2013-20646

Table of Contents

List of Tables

List of Figures

Introduction

1.1 Motivation

Rolling element bearings (REBs) are critical components of an engineering system; REBs, support loads and reduce the friction between moving parts. The failure of any individual bearing can be a significant contributor to the decline in the performance of the system and can even lead to a complete breakdown. To enhance the safety of system operation and prevent a system's performance from deteriorating and/or failing due to a bearing defect, it is necessary to monitor the degradation process of bearings in a timely and effective manner. Also, early and accurate warning of bearing failure conditions is important to determine a desired maintenance strategy, even if the duration of any particular anomaly states can range from a few hours to several months depending on various sources, i.e., applications, operating conditions, and failure threshold [1–3].

Based on prior research, condition monitoring (CM) techniques have been applied to measure defects and track the degradation of REBs in various ways. Among various condition monitoring techniques, vibration-based approaches have been widely adopted due to their effectiveness in detecting abnormal vibrations that

can indicate underlying physical phenomena. These techniques have become a common choice for identifying potential issues and maintaining the operational efficiency of various systems [4–9]. For this reason, numerous technologies related to bearing failure diagnosis and prognosis using vibration signals have been developed and related papers have been published [5,9–14]. However, for several reasons, the use of vibration signals for CM remains a difficult task. First, bearing vibration signals are nonstationary, with statistical properties that are periodically time-varying; this implies second-order cyclostationarity [15]. Second, a fault signal is typically weak in its early stages, and fault information is usually masked by strong background noise [16]. In general, an operational noise is assumed to be a random white noise with a broadband spectrum [17]. Further, fault signals are often masked by discrete frequency noises from external components, (e.g., gears, shafts, and motors) [5]. In addition, vibration signals may show characteristics of amplitude modulation (AM), where the natural frequency of a bearing defect is linked to the resonant frequency of the system structure. For accurate monitoring, the optimal bandwidth must also be chosen to demodulate the high frequency resonant responses associated with the envelope analysis [5]. Consequently, it is necessary to thoroughly understand and address these many kinds of characteristics of fault signals of REBs for effective diagnosis at the incipient fault stage.

1.2 Research Scope and Overview

This doctoral dissertation aims to create a comprehensive approach to modeling and analyzing vibration signals for effective diagnosis of incipient faults in REBs. To achieve this goal, two research thrusts were identified as the focus of this dissertation research: (1) the development of a practical signal model to accurately describe the physical behaviors of nonstationary bearing signals, and (2) the extraction and demodulation of fault-related features using cepstral coefficients to enhance the diagnostic information available in the raw signal. These research thrusts are described in detail below.

Research Thrust 1: Construction a practical signal model to explain physical behaviors

The first research thrust explores a signal model that combines the advantages of both an analytical signal model and a dynamic model. Since signals acquired in actual field settings are complex and the signals originating from various sources are combined, simulations that reproduce these inherent mechanisms through signal models have been often used in prior research [18–21]. From a signal processing point of view, analytic signal models are preferred over full dynamic simulations because, despite their approximation, the analytical results can directly interpret the influence of stochastic parameters on the bearing signal [22]. However, existing analytical models have a problem in that simulation results and actual measurement data do not match because the impulse function is modeled in a simple manner,

without considering the dynamic behavior at the time of impact. Thus in this study, the impact excitation mechanism based on Hertzian contact theory is implemented to reduce the gap between the simulated signal and the real signal. In this research thrust, preprocessing analysis is presented for a simulated bearing signal that is synthesized with other sources (i.e., a deterministic signal from a gear, a sinusoidal inference from a rotating shaft and white noise) to validate characteristics of the simulated results.

Research Thrust 2: Feature extraction and demodulation analysis by enhancing the fault-related information through cepstral coefficients

In practice, many sounds and vibrations are masked by background signals in nature; this reflects the operating conditions and environmental effects of the signal's source. In order to solve this limitation, Kim et al. [23] presented a new feature extraction algorithm called the power normalized cepstral coefficients (PNCC) approach; this method offers auditory physiological modeling for robust speech recognition in noisy environments. Inspired by this idea, this dissertation describes a new feature extraction method for REB diagnosis using vibration signals, namely the linear power normalized cepstral coefficients (LPNCC) approach. The proposed approach intends to enhance the REB signal, which is buried in noise that arises from environmental effects and contains some mechanical phenomena (e.g., mechanical looseness, misalignment). LPNCC can be used for analysis as a reconstructed time signal with the cyclic spectral component emphasized. Therefore, in this study, LPNCC of each channel is regarded as a filtered time signal. Then, demodulation

analysis can be perfomed by examining the squared envelope spectrum (SES); together, this overall procedure provides the LPNCC-SES. Through the LPNCC-SES, it is possible to see as a whole whether each channel divided by the filterbank and the cyclic frequency in the frequency domain is well represented

1.3 Dissertation Layout

This dissertation is organized as follows. Chapter 2 provides the technical background and literature reviews related to vibration-based REB diagnosis. In Chapter 3, a quasi-periodic impulse train model with an impact force function is derived. To validate proposed signal model, a representative study is presented. Chapter 4 introduces the proposed feature extraction method, which is called linear power-normalized cepstral coefficients (LPNCC); this chapter also presents the proposed fault diagnosis method by implementing LPNCC to the squared envelope spectrum (SES), for both simulation data and experimental data. Finally, Chapter 5 summarizes the dissertation and presents the conclusions, along with suggestions for future research.

Technical Background and Literature Review

This chapter provides an overview of vibration-based diagnosis for rolling element bearings (REBs), including the basic knowledge of REBs, the characteristics of bearing vibration signals, and the various techniques used for REB diagnosis. As there have been numerous studies on bearing diagnosis using vibration analysis techniques, the purpose of this chapter is to provide a brief overview of the relevant literature.

2.1 Vibration Signals of Bearing Faults

2.1.1 Rolling Element Bearings

Rolling element bearings (REBs) are a type of mechanical component that utilize rolling elements, such as balls or rollers, to reduce friction and enable motion between two bodies. This allows for smooth and efficient movement with minimal wear and tear on the bearing itself. REBs are used in a wide range of applications and are available in various designs to suit different needs [24]. There are several

types of REBs, each designed and used for a specific application and load, with specific advantages and disadvantages. In general, REBs consist of the following basic elements, which are the inner/outer races, the rolling elements, and the cage (or retainer) as shown in Figure 2-1.

2.1.2 Failure of Rolling Element Bearings

Bearings failures can be classified according to the severity of the failure, with categories including local, extended, and distributed failures [25–27]. It is common for multiple mechanisms to contribute to rolling bearing failure in practice. If the fault is not found early and the bearing is extensively damaged, the evidence is lost and this makes it challenging to identify the root cause. Analysis of the cause of failure is essential for repair and prevention of serious failures in the future. For this reason, industry and academia have standardized failures according to failure modes and mechanisms of rolling bearing [28]. Material fatigue is the most common failure mode for a REB that has been properly installed and operated [29], specifically rolling contact fatigue (RCF) from repeated Hertzian contact pressure between rolling elements and race way. For well-lubricated and properly manufactured bearings, the surface of the metal used in the bearing is strong enough to withstand friction and impact. Therefore, by repeated shear stress rather than tensile force applied to the surface, cracks are formed in an elasto-plastic zone which locate below the surface [24,30]. Once an incipient fault is generated by material fatigue, rolling contact wear is the most frequently seen phenomenon [29].

2.1.3 Bearing Fault Signature and Its Frequencies

During the performance degradation due to wear evolves, the dynamic responses of a surface are generated by topographical changes [31–34]. Thus, we can regard features from vibration measurement as a dynamic response which is bearing health-related index. Consequently, we can make a scenario of whole life of REBs as shown in Figure 2-2 [35]. At the normal state, condition monitored indexes are settled down to flat region after the running-in stage. This steady state takes up most of the lifetime and CM indexes begin to rise sharply when initial defects occur. Anomaly state can be regarded from the point when CM indexes rising can be detected until it reaches to the predetermined failure threshold.

When a rolling element comes across a defect, it may result in a shock that triggers high-frequency vibrations in the structure [36–38]. These resonances can be detected through vibration analysis and used to identify potential issues with the bearing. Monitoring the vibration characteristics of a system can help to identify changes that may indicate the presence of a defect or other issue. More specifically, the state can be classified into four stages according to the surface state and the resulting vibration characteristics, which can be more clearly classified through frequency analysis. The four basic bearing characteristic frequencies (BCFs) and their calculation shown in Figure 2-3. The BCFs of a bearing are determined by factors including the shape and dimensions of the bearing, the location of any faults, and the operating conditions. Many bearing fault diagnosis techniques aim at detecting these frequencies from measured vibration signals. Figure 2-4 shows the relationship between bearing vibration signal spectrum and characteristic frequency according to the degree of failure. A detailed explanation of each stage is as follows:

Stage I: This stage is considered normal state, even small pits or surface impurities of the bearing race appears. During this phase, low frequency rotational frequencies are predominantly observed in Zone 1. Peaks due to fine cracks or impurities on the surface are observed in the ultrasonic range above 10 kHz (Zone 4), but most of them are considered normal. A physical examination of the bearing at this point may not reveal any visible flaws or defects.

Stage II: Stage II begins as the bearing defect starts to "ring" the bearing part, producing a signal related to the natural resonant frequency which regarded as "carrier frequency". Noticeable increases in zone 3 and 4 regional signals are associated with this stage. Success in diagnosing bearing defects in inciepient stage depends on finding the frequency band including the natural frequency of zone 3 and detecting the demodulated bearing characteristic frequency through the envelope method.

Stage III: The size of the defect has grown to a level that can be confirmed with the naked eye after disassembly. The spectrum of the linear scale clearly shows the BCFs in zone 2 and its harmonics and sidebands, and the noise level of the vibration spectrum has increased significantly.

Stage IV: At this stage, immediate bearing replacement is required. Abnormal sound and vibration can be detected without additional measuring equipment. The defects are distributed on the inner/outer race and rolling elements, and the spectral level increases in a wide range.

2.2 Vibration Techniques for Bearing Incipient Fault Diagnosis

2.2.1 Overview of Vibration Techniques for Bearings

As a key component in engineering systems, REBs play a crucial role in supporting loads and mitigating friction between moving parts. For the centuries, engineers have considerably taken care of designing, installing, and operating REB to make engineering system performs well. Especially in operation, condition monitoring (CM) techniques have been widely applied to measure the defects and trail the degradation of REB in various ways, i.e., vibration, acoustic emission, temperature, and wear debris analysis. Thanks to its physical meaning and ease of use, the vibration-based approach is the most popularly utilized method among these techniques [4]. A number of admirable review articles are possible that have addressed the state-of-the-art of the related techniques, among which some representative ones are given in [6,10,12–14,26,39–42]. In particular, a systematic framework of fault diagnosis and prognosis has been presented for mechanical systems in [1,39,42–44]. Through this, the structure of vibration-based fault diagnosis for REBs in incipient stage can be organized by key techniques include vibration modeling, preprocessing, feature extraction, and fault diagnosis, as depicted in Figure 2-5.

Vibration Modeling

Modeling the vibration signals of normal and faulty bearings can provide valuable insights for diagnosis and is often used to develop and evaluate diagnostic techniques. Simulating faulty bearing signals can also help to better understand the mechanisms by which they are generated, particularly in cases where the response exhibits non-

linearity. The development of models for bearing defect signals has been the subject of extensive research, as these models can be used to assess the performance of various diagnostic approaches. Overall, the ability to accurately model faulty bearing signals can be a valuable resource for improving the effectiveness of bearing diagnosis. Bearing signal models for the incipient fault stage can be classified into these categories; periodic/quasi-periodic impulse-train models [19,21,22,45–47], nonlinear multi-body dynamic models [26,36,48–52], and finite element models [18,53–57].

Preprocessing

In the initial stage of a defect, weak bearing signals are frequently concealed by background noises. Also, bearing vibration signals are basically blinded in that all the various components that make up the signal, i.e. the different sources and different transmission paths from each signal starting point to the measurement point [58]. Therefore, it is necessary to increase the signal-to-noise ratio (SNR) of the defect signal signatures of bearing by removing noise and separating/enhancing the bearing related signal from raw signals. One of the most famous and widely used method is wavelet denoising developed by Donoho [59]. However, wavelet denoising is difficult to isolate a stochastic bearing signal when there is a deterministic periodic vibration source such as a gear or shaft. Furthermore, the stochastic nature of the bearing signal brings about it harsh to detect a fault-related signature from signals in incipient bearing fault stage. Therefore, signal separation methods such as autoregressive filtering (AR), self-adaptive noise reduction (SANC), time-synchronous averaging (TSA), or discrete/via random separation (DRS) can be applied here [5]. Recently, cepstrum-based methods have gained popularity because

they are simple to use, do not need any extra input parameters or adjustments, and work well in real-world situation. [60,61].

Feature Extraction & Fault Diagnosis

An fault diagnosis of bearings is composed of feature extraction and fault diagnosis (identification, classification) or their combination. Broadly, methods are classified into model-based techniques including statistical analysis and signal processing, and data-driven techniques encompassing machine learning techniques [1,13,43,62].

By the advantages of vibration analysis, various feature extracting techniques have been developed for several decades. There is no one definitive way to classify feature extraction methods used for diagnosis and prognosis, but Yan, Qiu, and Iyer [63] proposed a taxonomy of vibration-based feature extraction method. Recently, H. Zhou et al. [64] categorized feature extracting techniques into three categories: statistical parameter-based, signal processing-based, and machine learning-based. Additionally, some studies have utilized a combination or hybrid of these approaches.

Basically, most bearing fault diagnostic methods aim to detect fault characteristic frequencies. This means finding the BCFs in the spectrum corresponding to the fault position (inner/outer race, rolling elements, cage). Traditional frequency analysis methods are difficult to extract BCFs accurately. However, demodulation analysis allows the extraction of time-domain signal waveforms envelope traces [5,37]. It is possible to extract envelope signals containing only fault characteristic frequency components that carry high-frequency intrinsic vibration. It is possible to perform a detailed spectral analysis of the envelope signal.

Furthermore, failure detection and identification of data-driven approaches are classification algorithms based on clustering algorithms. Often, this process includes both feature extraction and diagnosis. Common classification algorithms include, the Support Vector Machine (SVM) [65–67], the fuzzy–logic [68–70], the Artificial Neural Network (ANN) [71], and the K-Nearest Neighbor Algorithm (KNN) [72]. Among these techniques, SVMs and ANNs are the most widely used in the field of incipient fault diagnosis. In the last few years, deep learning approaches have gained popularity for their superior performance compared to SVMs, ANNs, and other shallow intelligent models [1,39,73,74].

2.2.2 Cepstrum-Based Fault Diagnosis Techniques

One promising approach to separate the bearing signal from the original signal and to enhance fault-related harmonics or sidebands with consideration of cyclostationarity is to use the cepstrum. The envelope analysis can then be applied to the signal processed through cepstrum analysis to determine the bearing characteristic frequency. Randall [75] presented applicability of the cepstrum in mechanical problems. Two main areas of applicability were introduced, 1) detecting families of harmonics and sidebands and 2) blind separation of the source and transfer function effects. Peeters et al. [60] compared two cepstral editing methods, specifically, an automated cepstrum editing procedure (ACEP) and cepstrum pre-whitening (CPW). It was determined that the ACEP outperforms the CPW for low signal-to-noise ratio (SNR) values with additive white Gaussian noises, while the CPW outperforms the ACEP for low SNR values with additional noise resonance. Moshrefzadeh et al.[61] proposed the generalized CPW by adjusting the magnitude

order in the CPW, so called spectral amplitude modulation (SAM). The SAM was found to show good performances by giving different weights to different frequency components. Recently, Kim et al. [76] proposed the cepstrum-assisted empirical wavelet transform (CEWT) method, which improves the boundary selection of the empirical wavelet filters to include sideband clusters around gear mesh harmonics based on the spectrum.

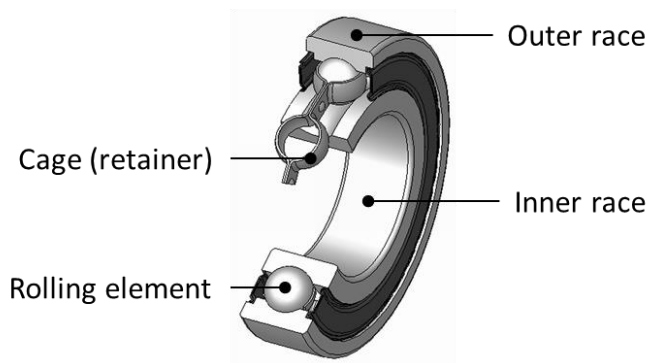

Figure 2-1 Rolling element bearing components

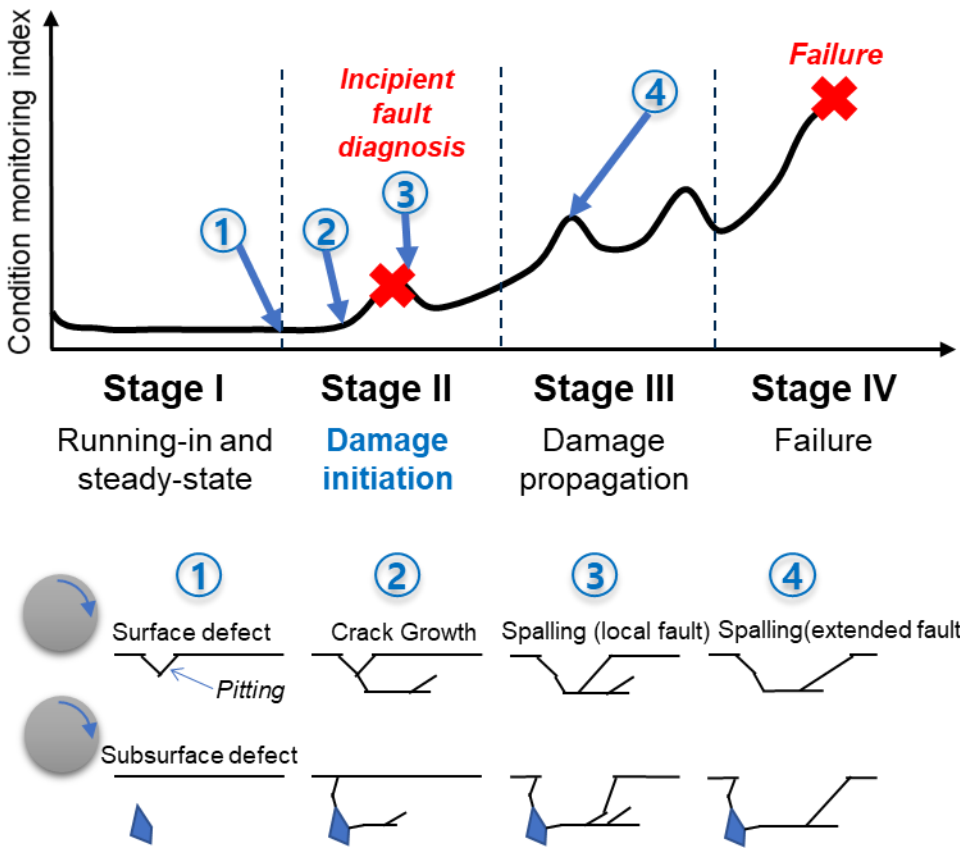

Figure 2-2 A descriptive four-stage degradation model for REBs.

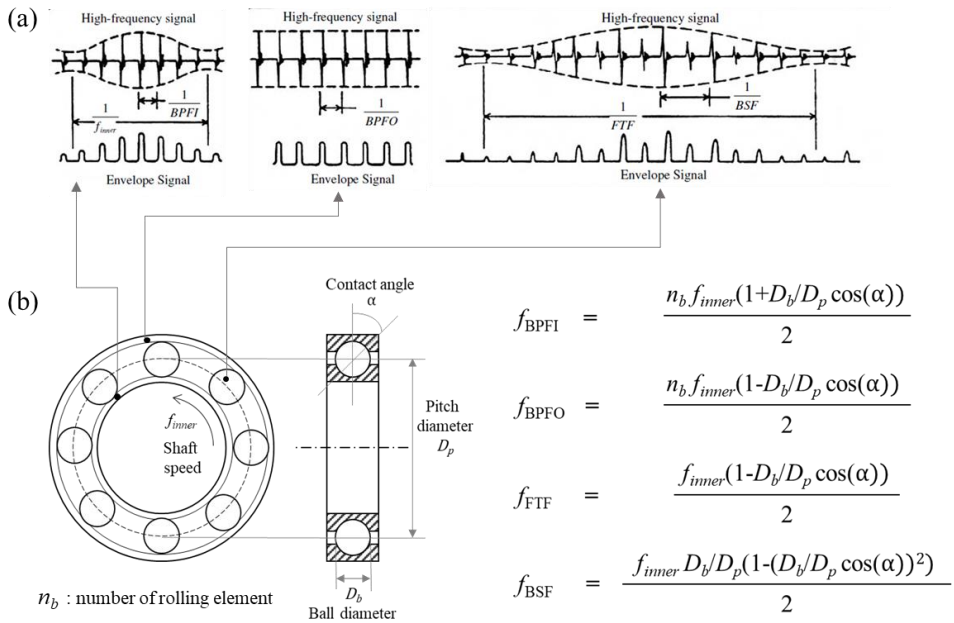

Figure 2-3 (a) Typical vibration signals generated by local faults [77] **(b) bearing characteristic frequencies** [78]

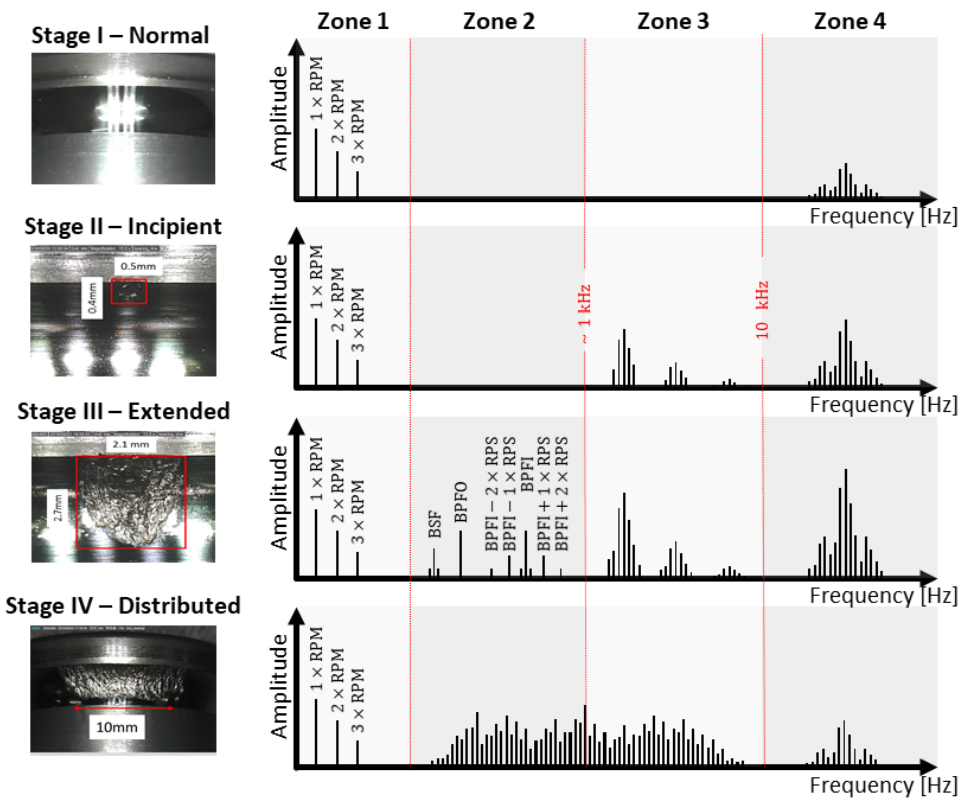

Figure 2-4 Four stages of the vibration spectrum depending on bearing fault growth

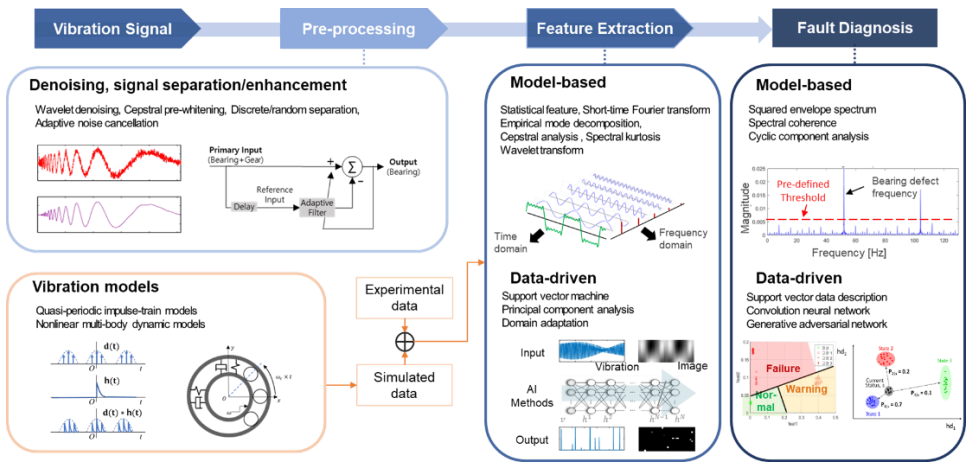

Figure 2-5 Overview of vibration analysis techniques for bearing diagnosis

Quasi Periodic Impulse Train Model with Impact Force Function

This section presents a quasi-periodic impulse train model with impact force function to better understand the complex, non-stationary vibration signals emitted by rolling element bearings with incipient fault. This model aims to bridge the gap between theoretical models and real-world data, providing a useful reference signal for diagnosis and analysis. The pseudo second-order cyclostationary signal is modeled using the quasi-periodic impulse train model, which aims to simulate the dynamic response of a system concerning the size of the defect and operating conditions by incorporating the impact force function, which reflects the change in contact stress. Finally, the proposed model is verified by performing signal processing of the synthesized signal including the simulation of the above model.

3.1 Vibration Modelling of Bearing Fault

3.1.1 General Mathematical Model

If a defect occurs in the bearing, it can cause a periodic impulse that can be observed using a vibration transducer. This impulse signal is carried by the resonant frequency which is determined by both the bearing and the machine [19] as shown as a schematic diagram in Figure 3-2. The displacement response $x(t)$ measured by the transducer can be derived by convolution with the impulse response and the impulse response function $h(t)$. Further, the impulse response is expressed as the product of the impulse function $d(t)$ and excitation force function $f(t)$ as follows mathematically;

$$x(t) = [d(t)\, f(t)] * h(t) \tag{3.1}$$

The impulse function $d(t)$ with amplitude d_0 and impulse period T_d is represented mathematically by the equation

$$d(t) = d_0 \sum_{k=-\infty}^{\infty} \delta(t - kT_d) \tag{3.2}$$

As previously stated, the impulse response function $h(t)$ is determined according to the position of the transducer and the transmission path of the signal. Theoretically, the signal can be modeled as above, but in an actual mechanical system, especially a rotating body system, the equation must be changed in consideration of the physical behavior. The characteristics to be considered and the corresponding formulas will be explained in detail below.

3.1.2 Quasi-periodic Model with Cyclostationary

Vibration signals can be broadly categorized as deterministic and random (stochastic). To be more specific, deterministic signals can be divided into periodic and non-periodic, while random signals can be categorized as stationary or non-stationary. Especially, non-stationary signals that show some cyclical behavior, despite not necessarily being periodic, are referred to as cyclostationary signals. These signals are often produced by hidden periodic mechanisms. [79–81].

In the presence of incipient fault such as pit or spall, vibration signals from REBs exhibit pseudo second-order cyclostationarity due to the uncertainties of REBs' nature such as slippage of the rolling elements/cage, speed fluctuations, variations of the directional load ratio and waviness of contact surface [22] as shown in Figure 3-1. This characteristic is highly indicative when the initial defect occurs and can be used for diagnostic purposes [15].

Attempts proposing to treat the bearing signals as cyclostationary have been fully agreed upon with the cyclostationary model effectively accounting for the need for envelope analysis [16,22,79,81–83]. Especially, Randall et al. [81] discovered that imprecise time interval of the bearing pulses, also known as "jitter," can disrupt the periodicity of the signal which makes bearing signals appear blurry in the signal spectrum. As a result, the cyclostationary model has become a popular choice for developing new diagnostic techniques for bearings. The cyclostationary model takes into account the non-stationary nature of REB's signal and this model can effectively capture the cyclical behavior that may be obscured by jitter [79], as well as being used extensively as a reference to bring existing bearing fault indicators into the framework of cyclostationary. Following these studies, Borghesani et al. [22]

recently organized the existing cyclostationary models for bearing failure, proposed a mixed model, and analyzed the effects. Thus, Equation 3.2 above can be modeled stochastically as

$$d(t) = \sum_{k=-\infty}^{\infty} d_0 \delta(t - kT_d - \tau_k) \tag{3.3}$$

As shown in Figure 3, the jitter that causes cyclostationary can be modeled as a Gaussian distribution or time delay τ , and pseudo cyclostationarity is implemented by modeling the interval between impulses ΔT_d due to the delay of the entire cage as a Gaussian distribution As a result, by combining the two models, a more realistic bearing signal can be simulated through the mixed model.

3.1.3 Excitation Force Function in Dynamic Models

As mentioned earlier in this chapter, excitation due to a defect can be modeled by Equation (3.1 as the product of the impulse function $d(t)$ and excitation force function $f(t)$. Depending on how the excitation force function is designed, the results of the vibration response also appear different. Therefore, Tandon and Choudhury [4] suggested that the shape of the pulse affects the spectrum by modeling the excitation force function in different pulse formats. Also, Behzad et al. proposed a stochastic model that assumes the randomness of the contact surface between the rolling elements and races makes the vibration excitation [46]. With the evidence that the excitation force function is caused by the change in contact stress around the defect, the excitation force function can be modeled as Hertzian contact force function. However, the above models describe the characteristics of the vibration

signature of the faulty bearing but does not incorporate the system's physical properties dynamically into the given model.

In studies of dynamic models, the vibration response has been calculated by equations of motion according to the change in Hertzian contact stress. The displacement can be calculated according to the following governing equations [84] (Figure 3-3). Assuming that the inner and outer races are firmly fixed, each can be regarded rigid. The motion of inner (shaft) and outer race (housing) are modeled as a 2–DOF system with translational motion in x and y directions. Then, the equations of motion of inner race can be denoted as

$$M_s\ddot{x}_s + C_s\dot{x}_s + K_s x_s = -F_x \tag{3.4}$$

$$M_s\ddot{y}_s + C_s\dot{y}_s + K_s y_s = -F_y - M_s g \tag{3.5}$$

and, in a similar way , the equations of motion of outer race can be presented as

$$M_h\ddot{x}_h + C_h\dot{x}_h + K_h x_h = F_x \tag{3.6}$$

$$M_h\ddot{y}_h + C_h\dot{y}_h + K_h y_h = F_y - M_h g \tag{3.7}$$

where M_h and M_s are mass of the housing with outer race (pedestal mass) and the shaft with inner race, C_h and C_s are damping coefficients and K_h and K_s are stiffness constant of the housing and the shaft, respectively. x_h and y_h are x and y displacements of outer race center of mass (also geometric center), x_s and y_s are x and y displacements of inner race center of mass and g is acceleration due to gravity. F_x and F_y is Hertzian contact forces [24] of each x and y directions (Figure 3-3) are defined as

$$F_x = K_b \sum_{j=1}^{Z} \lambda_j \delta_j^n \cos\phi_j \tag{3.8}$$

$$F_y = K_b \sum_{j=1}^{Z} \lambda_j \delta_j^n \sin\phi_j \tag{3.9}$$

where K_b is contact stiffness coefficient and λ is load distribution factor with a value of 0 or 1, Z is the number of rolling elements, ϕ_j is the angle of j-th rolling element's position, and n is load-deformation exponent constant. Deformation of surfaces due to the Hertzian contact between the j-th ball and race defined as

$$\delta_j = (x_s - x_h)\cos\phi_j + (y_s - y_h)\sin\phi_j + cl/2 \tag{3.10}$$

where cl is clearance of bearing.

If a defect occurs, the rolling path of ball will differ from the normal path as it rolls into and out of the defective area, as shown in Figure 3-4. For the purpose of accurate modeling the rolling path and the effect of the defect depth (H) on the displacement, the defect depth must be included in the model. This helps to better understand the physical processes involved and improve the realism of the model. As a result, Eq. (3.8) can be modified with time-varying displacement impulse $H(t)$ which represents the displacement change by the defect as follows.

$$\delta_j = (x_s - x_h)\cos\phi_j + (y_s - y_h)\sin\phi_j + cl/2 + H(t) \tag{3.11}$$

However, since the most dynamic models of interest is the change in contact stiffness and contact stress according to mechanical and kinematic characteristics, signal processing and diagnosis have yet to be focused on. Therefore, in this study, the contact stress function is implemented to the impulse model proposed to facilitate the signal processing technique. More details are provided in the next chapter.

3.2 Quasi Period Impulse Model with Impact Function

3.2.1 Overall Process of Proposed Model

The proposed vibration model is based on a stochastic model of the quasi-periodic impulse time and an excitation force function of the Hertzian contact theory around the defect. The stochastic model was set up as a psuedo second order cyclostationary according to [22,47]. The modeling of the Excitation force function followed the study of [85,86] considering the rolling body rolling and impact around the defect. As shown in Figure 3-5, a brief description of its formulation is given here.

The proposed model is delivered by modifying each function in Equation 3.1. First, the excitation force function, $f(t)$, is constructed in the contact area between rolling elements and races around the defect as a function from the Hertzian contact theory. Derivation of the excitation force function is covered in more detail in the section below. Second, the transfer function $h(t)$ is modelled as 1-DOF damped model with excitation derived as

$$\ddot{x}(t) + 2\zeta\omega_n \dot{x}(t) + \omega_n^{\,2} = m_{eff}^{\,-1} f(t) \tag{3.12}$$

and its transfer function is

$$h(t) = \frac{1}{\omega_n(1-\zeta^2)} \sin\left(2\pi \frac{\omega_n}{(1-\zeta^2)} t\right) \exp(-\zeta\omega_n t) \tag{3.13}$$

where m_{eff}, ζ, ω_n are, respectively, the effective mass, damping and natural frequency coefficients.

3.2.2 Modeling the Excitation Force

The determination of the excitation force is primarily based on the shape of the defect and the speed of the rolling element. As the rolling element moves, the area of contact moves along with it. If a defect is present, no matter its size, it disrupts the normal movement of the contact area, resulting in stimuli to the bearings and surrounding systems in various forms.

The excitation force function is derived mathematically by making the following assumptions [85]: (a) Rolling elements experience pure rolling motion, (b) bearing components are rigid with the exception of the contact area, (c) deformation of the edges occurs according to the Hertzian contact theory, (d) effect of the lubricating film is ignored, (e) interaction between components of bearing is ignored, and (f) size of the defect is smaller than the width and diameter of the rolling element, preventing contact between the rolling element surface and the defect base surface.

As shown in Figure 3-6, the motion of a rolling body around a fault can be divided into three phases. It can be divided into just before entering the fault (*I*), i.e. at the leading edge of the fault, entering the fault (*II*) and exiting the fault (*III*). Then, the periodic force pulse train $f(t)$ with periodic time T_d may be expressed in Fourier series as follows [85],

$$f(t) = a_0 + \sum_n [a_n \cos 2\pi n\omega_T t + b_n \cos n\omega_T t] \tag{3.14}$$

and the coefficients here are defined as

$$
\begin{aligned}
a_0 &= F_s(1-\frac{p_1}{2}-p_2-\frac{p_3}{2})+F_c(1-\frac{p_1}{2}-p_2-\frac{p_3}{2})+F_i(1-\frac{p_1}{2}-p_2-\frac{p_3}{2}) \\
a_n &= \frac{1}{\pi n}\left\{\begin{array}{l}\frac{(F_c-F_s)}{2\pi np_1}(\cos 2\pi np_1-1)+\frac{(F_i-F_c)}{2\pi np_1}(\cos 2\pi n(p_1+p_2)-\cos 2\pi np_1) \\ +\frac{(F_s-F_i)}{2\pi np_1}\{(\cos 2\pi n(p_1+p_2+p_3)-\cos 2\pi n(p_1+p_2)\}\end{array}\right\} \\
b_n &= \frac{1}{\pi n}\left\{\begin{array}{l}\frac{(F_c-F_s)}{2\pi np_1}\sin 2\pi np_1+\frac{(F_i-F_c)}{2\pi np_1}(\sin 2\pi n(p_1+p_2)-\sin 2\pi np_1) \\ +\frac{(F_s-F_i)}{2\pi np_1}\{(\sin 2\pi n(p_1+p_2+p_3)-\sin 2\pi n(p_1+p_2)\}\end{array}\right\}
\end{aligned}
\tag{3.15}
$$

where the meaning of the notations used is as follows: F_s is the force before entry into the defect; F_c is reduced contact force onto the ball in the defect area; F_i is the impact force height; p_1=TTI/T_d, p_2=t_i/T_d, and p_3=t_D/T_d; TTI is time to impact; t_i is the impact duration; t_D is the time to restress; T_d is the time period for BCFs. The parameters for each step are defined in more detail below.

(1) Entry Event: Destressing Phase (*I*)

In this event, distress occurs as losing contact while the ball moves from point A to point B and changes in time and force at this moment are as follows. Duration between the entry and the exit of spall t_{exit} is modeled as [87]

$$
t_{exit} = \frac{2D_p}{\pi f_r(D_p^2-{d_b}^2)}d_{def} = TTI + t_i + t_D \tag{3.16}
$$

where the notations are defined as d_{def} is the width of the defect, d_b is the ball diameter, D_p is the pitch diameter, and f_r is rotational frequency. Assuming the rolling elementss are evenly spaced in the cage and move identically, the TTI can be

approximated as:

$$\mathrm{TTI} \sim \frac{1}{2} t_{exit} \tag{3.17}$$

and the amount of change in contact deformation is Δh in Figure 3-6 can be approximated by the above assumption (e) as follows;

$$\Delta h_{approx} = \frac{d_{def}^2}{4 d_b} \tag{3.18}$$

At this time, the amount of maximum destress force F_c, is determined as follows by referring to Eq. (3.8) and Eq. (3.9).

$$F_c = K_b \delta_c^{3/2} = K_b (\delta_i + \Delta h_{approx})^{3/2} \tag{3.19}$$

(2) Impact Event (*II-II'*)

The effect on bearing components during impact relies on the external load and the relative speed of the balls and races. The process of impact from point B to point C is represented in Figure 3-6, and additional deformation occurs due to collision during impact as shown in Figure 3-7. In this process, the impact time t_i and the impact force F_i can be inferred through the maximum displacement δ_m.

The change in energy due to the collision between two objects in the collision process is as follows [88]:

$$\Delta E_{impact} = \frac{1}{2} m_{eff} (1 - c_r{}^2) \dot{\delta}^{(-)^2} \tag{3.20}$$

$$c_r = -\frac{\dot{\delta}^{(+)}}{\dot{\delta}^{(-)}} \tag{3.21}$$

where c_r is the coefficient of restitution $0 < c_r < 1$, $\dot{\delta}^{(-)} = v_i^{(-)} - v_j^{(-)}$ is relative approach velocity. Then, the collision time and maximum deformation are defined as follows [89]

$$t_i = \int_0^{\delta_m} \frac{d\delta}{\dot{\delta}}, \quad t_i = \frac{\delta_m}{\dot{\delta}^{(-)}(n+1)} Beta\left(\frac{1}{n+1}, \frac{1}{2}\right), \quad n = 3/2 \text{ (for point contact)} \tag{3.22}$$

$$\begin{aligned} \delta_m^{n+1} &= \frac{m(n+1)(\dot{\delta}^{(-)})^2}{2\left(k + \frac{3k(1-c_r)}{2c_r\dot{\delta}^{(-)}} \cdot \frac{2\dot{\delta}^{(-)}}{3}\right)} = \frac{c_r m(n+1)(\dot{\delta}^{(-)})^2}{2k} \\ \delta_m^{n+1} &= \frac{m(n+1)(c_r\dot{\delta}^{(-)})^2}{2\left(k - \frac{3k(1-c_r)}{2c_r\dot{\delta}^{(-)}} \cdot \frac{2c_r\dot{\delta}^{(-)}}{3}\right)} = \frac{c_r m(n+1)(\dot{\delta}^{(-)})^2}{2k} \end{aligned} \tag{3.23}$$

Through the above result, t_i and F_i can be approximated as follows

$$t_i \propto t_{exit} f_r^{1/5} \tag{3.24}$$

$$F_i \propto (F_s - F_c) \cdot (\frac{f_r}{2\pi})^{(6/5)} \tag{3.25}$$

(3) Exit Event: Restressing Phase (*III*)

In the restressing phase, the rolling element is again in contact with the non-defective part of the raceway (Point C to Point D). During this phase, the center of rotation is

assumed to be fixed as the rolling element is assumed to roll out from the compressed trailing edge of the defect. To determine the duration of the restressing phase for the rolling element, time t_D is determined by

$$t_D = t_{exit} - \mathrm{TTI} - t_i \tag{3.26}$$

3.3 Numerical Results and Discussion

To validate the adequacy of the proposed signal model, this dissertation used a synthesized signal by combining signals generated from other sources, as shown in Figure 3-8. The signal composes of four parts: the psuedo second-order cyclostationary component x_c, the deterministic feature pulses x_d, the sinusoidal interference due to shaft x_s, and the white Gaussian noise x_n. Consequently, the synthetic formula of the simulation x_{syn} is as follows.

$$x_{syn} = x_c + x_d + x_s + n(t) \tag{3.27}$$

$$\begin{aligned} x_c &= A_c \cdot d_c(t) * h_c(t) \\ d_c(t) &= \sum_k \delta(t - kT_c - \tau_k) \end{aligned} \tag{3.28}$$

$$\begin{aligned} x_d &= A_d \cdot d_d(t) * h_d(t) \\ d_d(t) &= \sum_k \delta(t - kT_d) \end{aligned} \tag{3.29}$$

$$x_s = A_s \sin(2\pi f_r t) \tag{3.30}$$

where A_c, A_d and A_s are amplitude coefficient of cyclostationary signal, deterministic signal and sinusoidal interference, respectively. The transfer function $h_c(t)$ and $h_d(t)$ of cyclostationary and deterministic component are modelled as 1-DOF damped model refer to Eq. (3.13) with rotational frequency f_r = 25 Hz. As parameter settings for the bearing signal, the bearing frequency f_c = 158 Hz (=1/T_c) with the carrier frequency ω_c = 3500 Hz, and for the deterministic signal, f_d = 60 Hz (=1/T_d) with the carrier frequency ω_d = 3000 Hz.

Also, the single unit impulse $d_c(t)$, is modeled quasi-periodically by reflecting

random motion by the stochastic model in Eq. (3.3). Here, the jitter interval τ_k and the delay time interval ΔT_c due to the slip of the ball including the cage are modelled as independent identically distributed Gauss distribution, respectively, $\tau_k \sim \mathcal{N}(0, \sigma_\tau^2)$, $\sigma_\tau = 1\% \times T_c$ (jitter) and $\Delta T_c \sim \mathcal{N}(\mu_\Delta, \sigma_\Delta^2)$, $\mu_\Delta = T_c$, $\sigma_\Delta = 1\% \times T_c$ (cage slip). There is no solid reference or theoretical background for each jitter and delay interval. However, this value to 1% of defect time interval, ΔT_c, is recognized within a reasonable range [81].

The results of analysis in the freqeuncy domain and envelope spectrum of the synthesized signal are shown in Figure 3-9. In the case of the results in the power spectral density (PSD), it shows a peak at the carrier frequency of 3500 Hz, but the sidebands are smeared while the sideband of f_d harmonics (e.g., Gear Mesh Frequencies, GMFs) appears neatly around the carrier frequency of 3000Hz in the PSD in the deterministic signal case. Through this, the signal characteristics of cyclostationary can be well explained. However, as mentioned above, looking at the results of envelope analysis, it is noted that BCF and harmonic components are detected. In the case of the synthesized signal, the BCF componens are not well seen in the PSD result because the relatively strong GMFs hide them. However, BCF components are detected even among strong GMF components in the envelope spectrum. For this reason, pre-processing and signal separation techniques are essential to detect bearing defect signals.

3.3.1 Necessity of Choosing an Appropriate Preprocessing Method

Conventional denoising methods often rely on the assumption of white noise, which is not applicable in this simulation due to the presence of cyclostationary random signal interference. In this chapter, this effect was compared and considered by applying the following two methods. First, the wavelet denoising method [59], which has excellent performance in removing white noise, was applied. In addition, the cepstral pre-whitening (CPW) method [90], which shows excellent performance in separating the deterministic signal and the bearing signal, was applied. The results of each preprocessed signal were compared through the envelope spectrum and bandpassed results were compared in the bandwidth (3000-4000 Hz) with the bearing carrier frequency of 3500 Hz as the centeral frequency. The time interval of each sample was 10 seconds with a sample rate of 10000 Hz. Coefficient values used in generating each signal of the synthetic signal are summarized in Table 3-1. To compare the results according to the energy of the bearing signal, simulation and analysis were performed for the two cases.

First, it was analyzed at the bearing signal intensity level where the bearing defect frequency was detected even without applying a band pass. The signal-to-noise ratio (SNR) was adopted to represent the intensity of energy of each signal and it is defined as follows

$$\mathrm{SNR}_{\mathrm{target}} = P_{\mathrm{target}} / P_{\mathrm{noise}} \tag{3.31}$$

In this case, the SNR of the deterministic component was set to $\mathrm{SNR}_d = -12$ dB, and the SNR of the sinusoidal inference signal was set to $\mathrm{SNR}_s = -17.5$ dB, and for the bearing signal, the level of SNR_c was set to –13.70 dB. As shown in Figure 3-10,

when bandpass without any preprocessing, harmonics of f_c still appears clearly, but it can be seen that the amplitude of harmonics of f_c are relatively increased compared to before bandpass. On the other hand, in the case of wavelet denoising, hamonics of f_d appears, but the bearing signal does not appear unless band pass is applied, and even performance is lower than before denoising is applied. Also, it can be seen that only harmonic components of the rotation frequency are detected. In the case of CPW, harmonics of f_c are clearly separated, as shown in the left-bottom part of Figure 3-10.

In order to assume a case where the bearing signal is weaker, that is, the size of the defect is smaller than the above case, each technique was applied when the power of the bearing signal was reduced (SNR_c = –15.85 dB) while the power of the other signals is the same. As shown in the envelope spectrum of the original signal in the Figure 3-11, 1X of the BCF is detected finely, and harmonics are also seen in the case of band pass, but the relative peak size is clearly reduced compared to the previous case. In the case of wavelet processing, BCFs were not detected regardless of whether a band pass was applied or not. In the case of CPW processing, it is difficult to detect BCFs when the band pass is not performed, but when the band pass is performed, it can be confirmed that BCFs appear relatively well compared to other results.

From this result, it can be seen that an appropriate preprocessing process is essential to diagnose bearing failure in the incipient failure stage and that effectively finding the frequency band containing failure information is essential for performance improvement.

Table 3-1 Summary of coefficients for the signal generation

Coefficients	Values
Bearing carrier frequency, ω_c	3500 Hz
Bearing defect frequency, f_c (=1/T_c)	158 Hz
Deterministic carrier frequency, ω_d	3000 Hz
Deterministic period frequency, f_d (=1/T_d)	60 Hz
Amplitude of deterministic signal, A_d	2000
Shaft modulation frequency, f_r	25 Hz
Amplitude of shaft modulation, A_s	0.1
Amplitude of noise	0.5

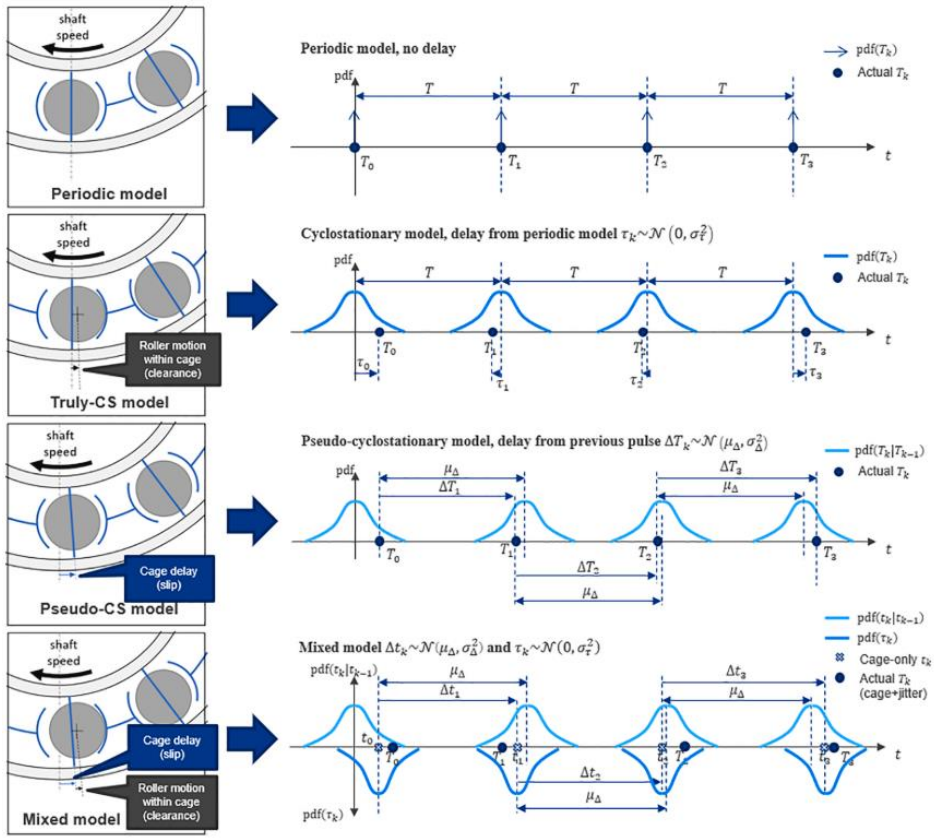

Figure 3-1 Qualitative illustration of the difference in the timing randomness of the models

(Adapted from [22] **with permission)**

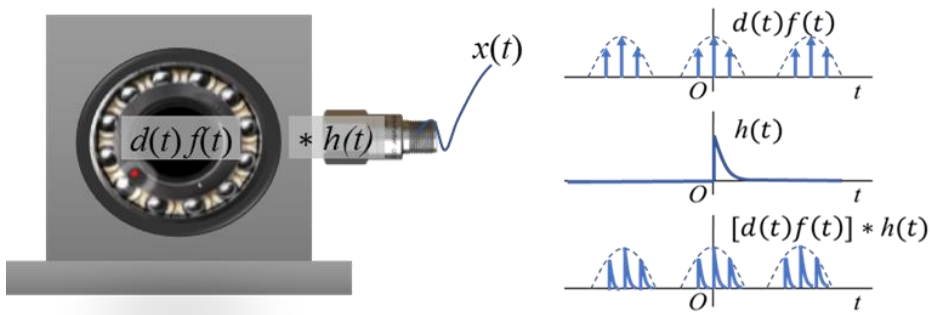

Figure 3-2 Schematic diagram of excitation and response function of the impulse train model for REBs

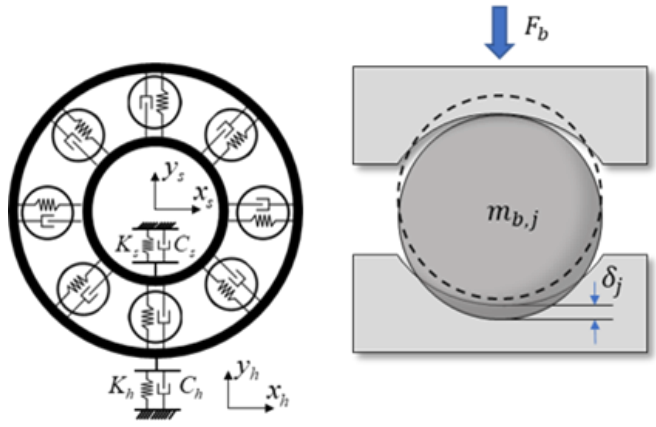

Figure 3-3 Diagram of the multi-body nonlinear dynamic model and Hertzian contact deformation model

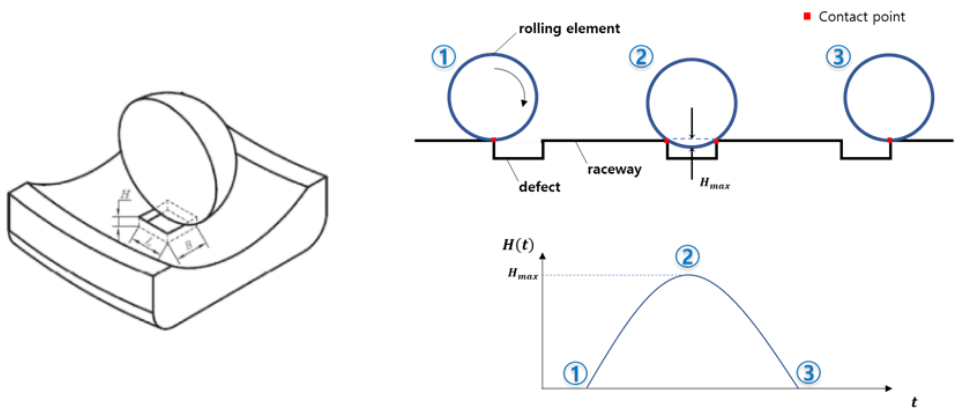

Figure 3-4 Time-varying displacement function $H(t)$ with the defect

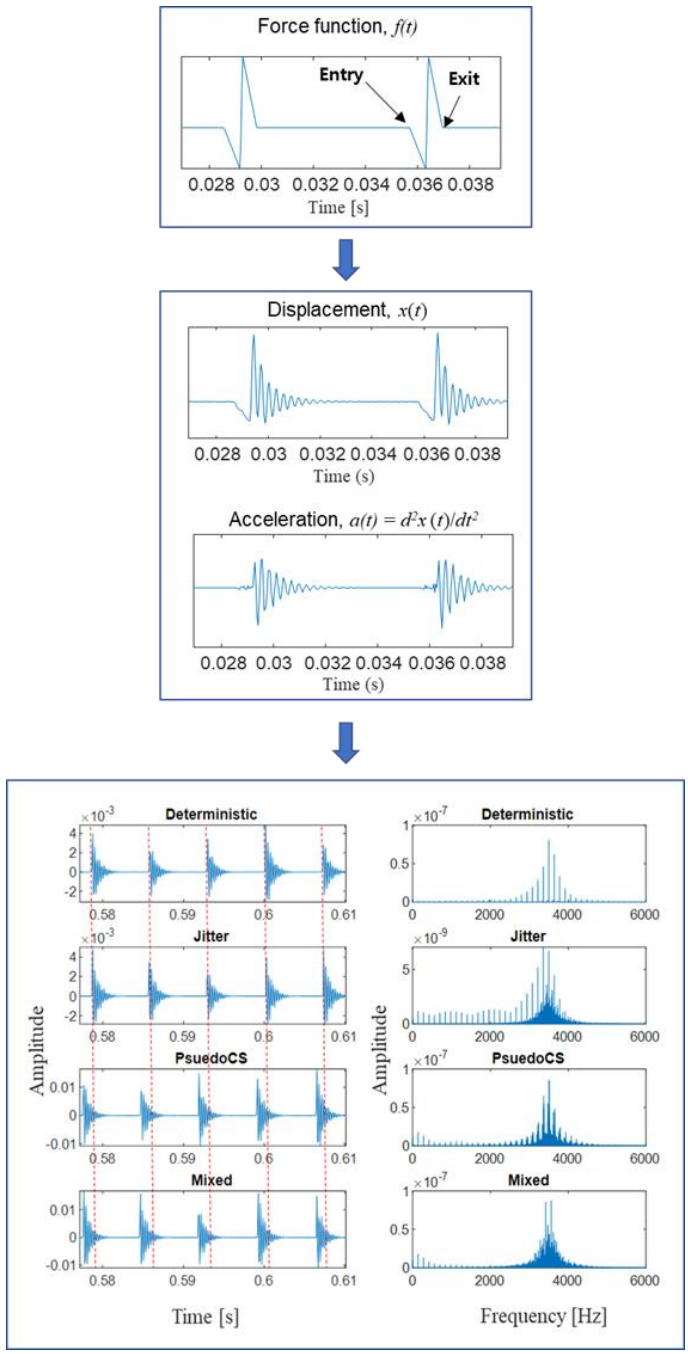

Figure 3-5 Overall process of proposed signal model

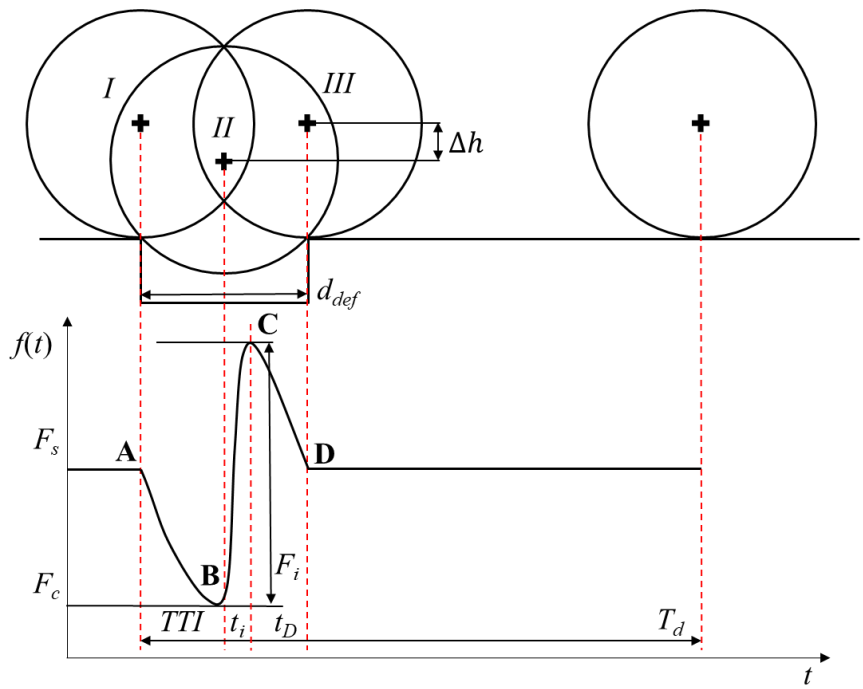

Figure 3-6 Representation of events of roller-raceway contact relationship and time-dependant force excitation model

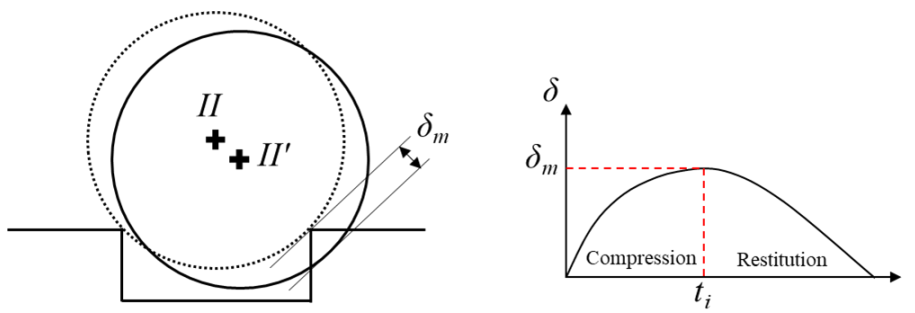

Figure 3-7 Contact process of impact

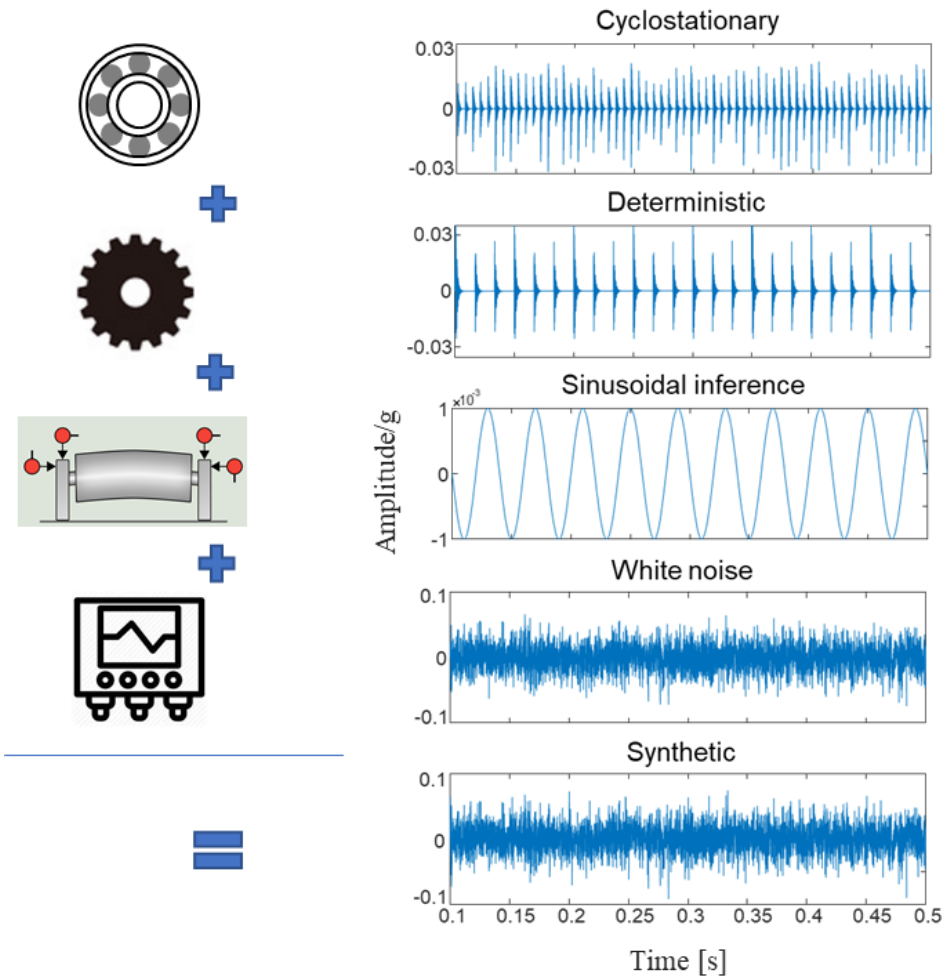

Figure 3-8 Synthetic signals and signals in the time domain

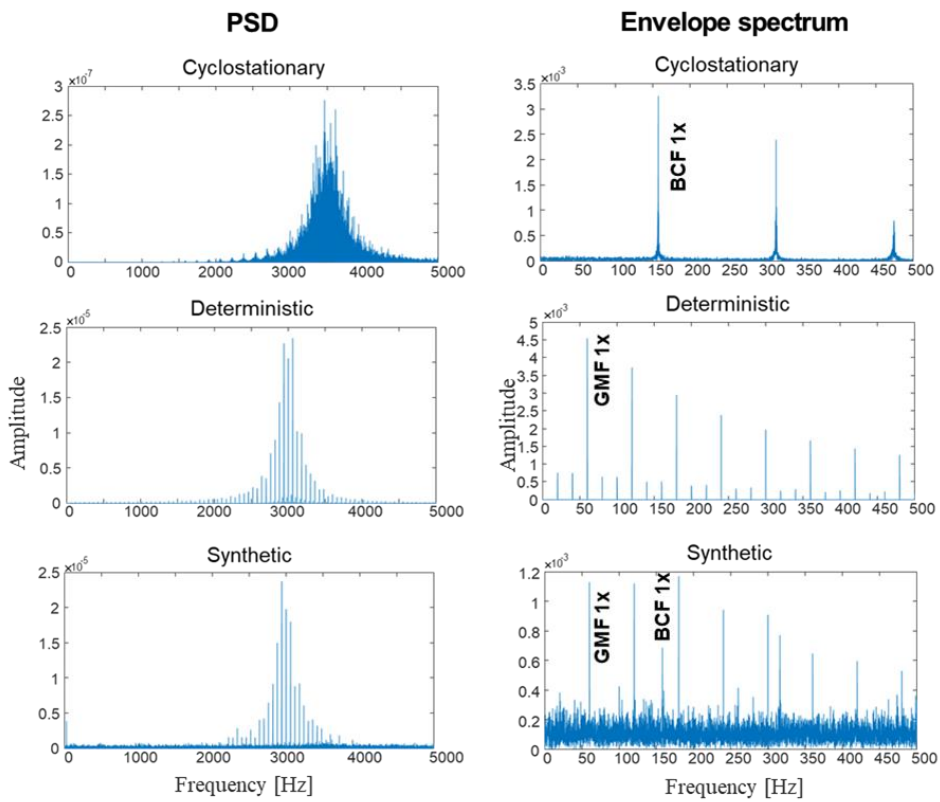

Figure 3-9 Power spectral density and envelope spectrum of cyclostationary, deterministic, and synthesized signals

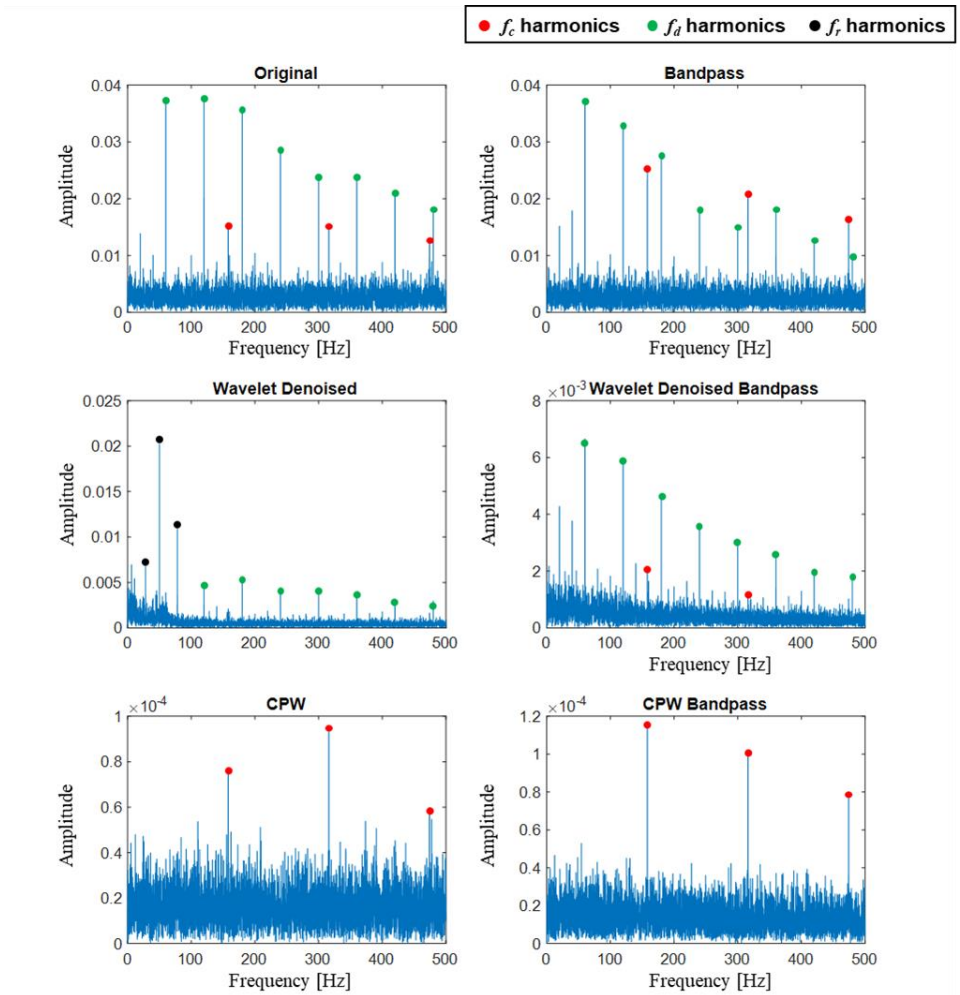

Figure 3-10 Envelope spectrum of applying preprocessing methods and bandpass of SNR_c= -13.70 dB case

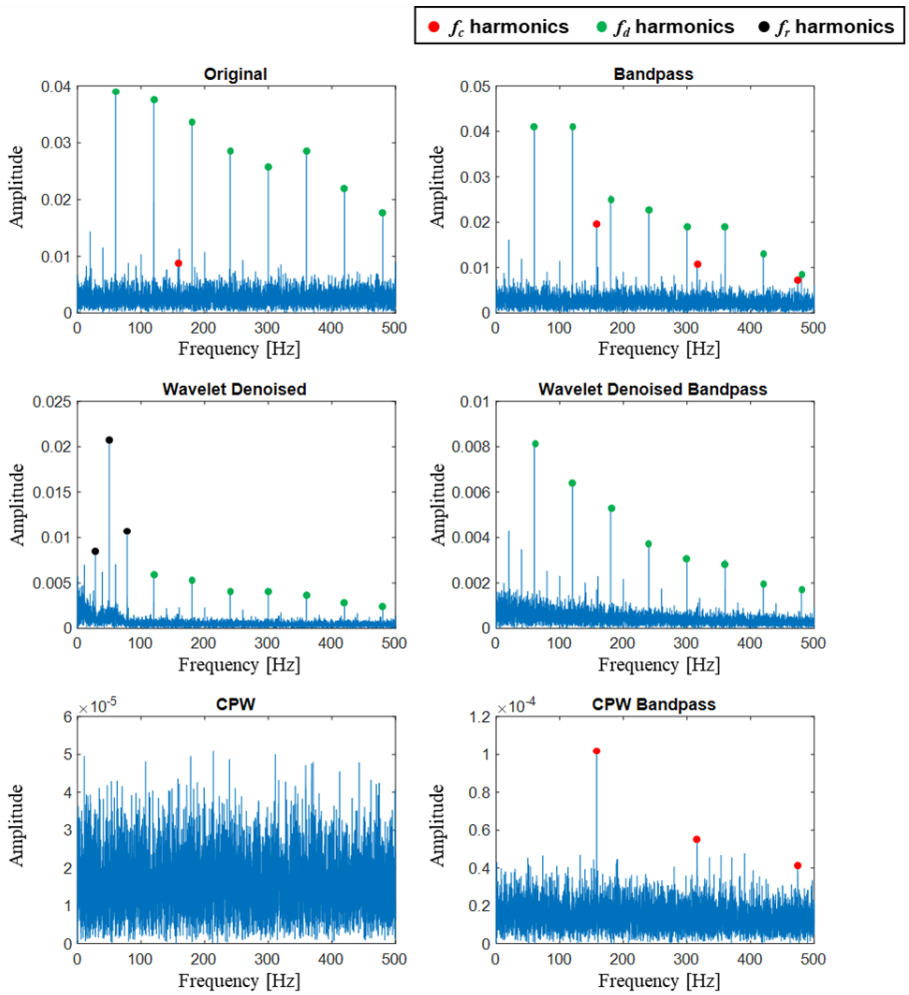

Figure 3-11 Envelope spectrum of applying preprocessing methods and bandpass of SNR_c= -15.85 dB case

Speech Recognition-Inspired Feature Engineering for Bearing Fault Diagnosis

One of the most critical challenges in rolling bearing diagnosis is dealing with weak fault signals that are buried in noises arising from environmental effects. To overcome this problem, the feature extraction method described in this section aims to develop a noise-robust feature extraction method, namely linear power-normalized cepstral coefficients (LPNCC), inspired by speech recognition based on auditory physiology. In this approach, for the cepstra from a feature extraction process, the squared envelope spectrum (SES) are computed to find bearing characteristic frequencies. The performance of the proposed method is examined by studying simulation data and experimental data. It can be concluded from the results that the proposed method has the potential to be utilized for robust bearing diagnosis in various noisy environments.

4.1 Review of Power-Normalized Cepstral Coefficients (PNCC)

4.1.1 Basic Definition of Cepstrum

The term "cepstrum" is a term derived from the word "spectrum". This term is often used to describe the spectrum of a spectrum. Other terms, such as "quefrency", "rahmonics", and "lifter", are also modified versions of related terms, such as "frequency", "harmonics", and "filter", and are used to emphasize their connection to the cepstrum. These terms continue to be widely used in the literature to distinguish their reference to the cepstrum rather than the original spectrum or time signal [75].

For discrete-time signals, the original definition of the (power) cepstrum $c[n]$ of a signal $x[n]$ is the inverse discrete-time Fourier transform (IDTFT) of the log-magnitude of the discrete-time Fourier transform (DTFT), which is as follows [91]:

$$c[n] = \frac{1}{2\pi} \int_{-\pi}^{\pi} \log\left|X(e^{j\omega})\right| e^{j\omega n} d\omega \tag{4.1}$$

where the DTFT of $x[n]$ is defined as:

$$X(e^{j\omega}) = \sum_{n=-\infty}^{\infty} x[n] e^{-j\omega n} \tag{4.2}$$

where j is the imaginary unit, ω depicts the normalized radian frequency and n is a time sample number, known as the "quefrency."

4.1.2 Characteristics of cepstrum in mechanical vibrations

As shown in Figure 2-3 (a), one of the characteristics of a bearing signal is amplitude modulation; in this phenomenon, a high-frequency carrier signal is varied by a low-frequency modulating signal that is mainly produced by the fundamental frequency of the shaft rotation [92]. A vibration signal with amplitude modulation can be represented as [19,92]:

$$x(t) = \sum_{m=1}^{md} \left(\int_{-\infty}^{t} d_m(\tau) q_m(\tau) a_m(\tau) e^{-c(t-\tau)} \cos(2\pi f_c(t-\tau))\, d\tau \right) + A_s \sin(2\pi f_s(t) + \theta_s) \quad (4.3)$$

where the first summation term describes the vibrations of the defect components and the second sinusoidal term defines the modulation that is due to shaft rotation. In the first term of Eq.(4.3), *md* is the number of defects in the bearing, which is typically 1 for a single-component defect condition, $d_m(t)$ depicts the defect impulse train of the contact and is modulating signal that repetitively occurs with the bearing characteristics frequency (BCF), $q_m(t)$ describes the dimension information of defect and the sensitivity of the striking energy, $a_m(t)$ is a characteristic function of the transmission path, and c and f_c represent the decaying (damping effect) rate and the carrier frequency, respectively. In the other term, A_s is the amplitude of the modulating signal, f_s and θ_s depict, respectively, the fundamental frequency and the initial angle of the modulating signal.

In a bearing system, the impulse caused by a defect of a bearing could be represented by bursts of exponentially decaying vibration in the time domain (Figure 4-1 (a)) and by sidebands in the vicinity of the carrier signal in the frequency domain, as shown in Figure 4-1 (b). The carrier signal, which can be found as shown in Figure

4-1 (b), can be a combination of the resonant frequencies of the bearing or even of the overall mechanical system. Furthermore, when logarithmic transformation is applied to the spectrum of the signal, the defect frequencies that are due to bearing defects can be enhanced (Figure 4-1 (c)).

It should be noted that one property of cepstrum is that low quefrencies correspond to slowly varying (in frequency) components in the log-magnitude spectrum, while high quefrencies correspond to rapidly varying components of the log-magnitude spectrum [91]. By applying inverse Fourier transform to the upper log-magnitude spectrum in Figure 4-1 (c) to extract the rahmonic peaks (first rahmonic peak at 6.67 ms = 150 Hz), periodic impulses related to the BCF are found, as shown in Figure 4-1 (d). Accordingly, cepstrum analysis has been used in mechanics and acoustics to detect and quantify families of periodically spaced spectral components; this will not only detect families of harmonics, but also equally spaced modulation sidebands [75].

4.1.3 Power-Normalized Cepstral Coefficients (PNCC)

Since the structure of PNCC is based on that of MFCC, to briefly describe the MFCC extraction process, first, the power spectrum of the input signal is integrated using mel-scale frequency integration. Then, the short-term power spectrum for each filter bank is obtained as defined as:

$$P[m,l] = \frac{1}{A_l} \sum_{k=L_l}^{U_l} \left| X_m[k] H_l[k] \right|^2, \qquad l = 1, ..., L \tag{4.4}$$

where $X_m[k]$ is a discrete Fourier transform (DFT) result for the mth frame and $H_l[k]$ is the weighting function for the lth channel, ranging from DFT index L_l to U_l, and A_l is a normalizing factor for the lth mel-filter, which is defined as:

$$A_l = \sum_{k=L_l}^{U_l} \left| H_l[k] \right|^2 \tag{4.5}$$

So, the nth MFCC for the mth frame is computed by a discrete cosine transform of the logarithmic function of the lth filter output $P[m,l]$ as defined as:

$$\mathrm{MFCC}[m,n] = \frac{1}{L} \sum_{l=1}^{L} \log[P[m,l]] \cos\left[\frac{\pi}{L} (l - 1/2) n \right], \qquad n = 1, ..., N_{\mathrm{MFCC}} \tag{4.6}$$

where the number of cepstrum coefficients, N_{MFCC}, is less than the number of mel-filters, L.

The PNCC introduces an algorithm called the suppression of slowly-varying component and falling edge (SSF) [23,93], which improves the spectral function for robust speech recognition, especially in reverberant environments. Therefore, the frequency spectrum $P[m,l]$ is subjected to the SSF process to reduce noise and

emphasize the fault-related signals. Because typical fault-related features from a bearing are modulated by a slowly-varying vibration signals from rotating components of the system, PNCC can be employed for fault diagnosis of bearing. This processing mimics aspects of both the precedence effect and spectrum modulation. The transfer function $\tilde{S}[m,l]$ modulates the original spectrum signal as follows:

$$T[m,l] = P[m,l]\tilde{S}[m,l] \tag{4.7}$$

The details of the transfer function process can be found in Ref. [23].

In the case of the PNCC processing, the response of the processing is affected by the change in the absolute power, and this effect can be reduced by the mean power normalization, as defined below [23]:

$$\mu[m] = \lambda_\mu \mu[m-1] + \frac{1-\lambda_\mu}{L}\sum_{l=0}^{L-1} T[m,l] \tag{4.8}$$

where $\mu[m]$ is the mean power estimate of the mth frame with the value of 0.999 for the forgetting factor λ_μ, and L is the number of filters, as used in Eq. (4.7). Consequently, the normalized power $U[m,l]$ is obtained by dividing the incoming power $T[m,l]$ by a running average of the overall power $\mu[m]$, with the arbitrary constant k, as follows.

$$U[m,l] = k\frac{T[m,l]}{\mu[m]} \tag{4.9}$$

As a result, a power-law nonlinearity spectrum $V[m,l]$ is calculated as:

$$V[m,l] = U[m,l]^{\eta_p} \tag{4.10}$$

where n_p is the power-law coefficient and $U[m,l]$ is the normalized power. Finally, the structure of PNCC is obtained by replacing the logarithmic function of the filter output $P[m,l]$ with the power-law function of the filter output $V[m,l]$ as follows:

$$\text{PNCC}[m,n] = \frac{1}{L}\sum_{l=1}^{L} \log[V[m,l]] \cos\left[\frac{\pi}{L}(l-1/2)n\right], \qquad n = 1, ..., N_{\text{PNCC}} \tag{4.11}$$

Although the PNCC is effective to show signal characteristics in the time and frequency domains in the presence of noise, however, the PNCC has not been applied much for mechanical systems because it was originally developed for voice recognition, by modeling the auditory mechanism. The proposed method incorporates the PNCC to enable noise-robust feature extraction for REB diagnosis by considering characteristics of vibration signals measured in fields.

4.2 Proposed Feature Extraction Method: Linear Power-Normalized Cepstral Coefficients (LPNCC)

Based on Kim and Stern's work [23], we adopt and revise the power normalized cepstral coefficients (PNCC) algorithm to diagnose a mechanical system by considering the characteristics of the vibration signal measured in a rolling element bearing, as shown in Figure 4-2.

In the case of PNCC, the filterbank is designed to take into account a model of human sound perception performed in the inner ear [91]. As shown in Figure 4-3, as the gammatone filter goes from the high to low frequencies, the frequency band it covers becomes denser because the human voice information is concentrated in the low frequency band. However, unlike a voice signal, the information of a bearing vibration signal is concentrated in the carrier frequency, which is arbitrary placed due to the system configurations. For this reason, Sousa et al. [94] proposed a linear frequency cepstral coefficients (LFCC) which replace the mel-filter of MFCC with a linear filter for anomaly detection in bearings. With reference to this, in this study, we replaced the gammatone filter of PNCC with a linear filter to weight equally for all filterbanks as shown in Figure 4-3.

The method of calculating the spectral power is similar to that shown in Eq. (4.4) to (4.11); however, it is calculated by using a linear-scaled weight function, instead of a nonlinear-scaled weight function. The spectral power $P'[m, l]$ using the summation of the linear triangular filters by virtue of Wojcicki [95], as below:

$$P'[m,l] = \sum_{k=0}^{(K/2)-1} \left| X[m,e^{j\omega_k}] H_{linear,l}(e^{j\omega_k}) \right|^2 \tag{4.12}$$

where m and l represent the frame and channel indices, respectively. The response of the lth linear filter channel at frequency ω_k is $H_{\text{linear},l}(e^{j\omega_k})$, and ω_k is the dimensionless discrete-time frequency $2\pi k/K$, where K is the DFT size. Each analysis band weights the magnitude-squared STFT outputs of positive frequencies by the frequency response associated with L-channel linear filterbank whose center frequencies are uniformly spaced.

With a linear filtered spectral power $P'[m, l]$ instead of $P[m, l]$, the rest of the process proceeds similarly to Eqs. (4.7) to (4.11). Also, we consider the value of the power law coefficient, n_p to be 1/5, which provides better performance for white noise [23] . Finally, the nth LPNCC for the mth frame is computed as follows:

$$\text{LPNCC}[m,n] = \frac{1}{L}\sum_{l=1}^{L} \log[V'[m,l]] \cos\left[\frac{\pi}{L}(l-1/2)n\right], \qquad n = 1, ..., N_{\text{LPNCC}} \tag{4.13}$$

The LPNCC is a useful feature for bearing diagnosis, which does not only contain both time and frequency information of a signal, but is also more robust to noisy environments than traditional MFCC.

4.3 Fault Diagnosis by Implementing LPNCC

Based on the PNCC algorithm, in this study, the LPNCC algorithm is developed to extract fault-related features for REB diagnosis, which is robust to noisy environments. The primary advantage of the LPNCC is that it enhances a REB signal, which is buried in noises that arise from environmental effects and contain mechanical phenomena (e.g., mechanical looseness and misalignment). Figure 4-4 shows the overall procedure for calculating the LPNCC. As shown in Figure 4-4 (b) – LPNCC Extraction, the extracted LPNCC for each channel can be considered as a filtered signal. Then demodulation analysis is performed by examining the squared envelope spectra (SES) of each filtered signal as shown in Figure 4-4 (c) – Demodulation Analysis, where envelope spectrum results at specific channels are represented. Consequently, this procedure gives the LPNCC-SES as shown in Figure 4-4 (d) – Output: Fault Diagnostics. Finally, faults can be discriminated from the selected channel, which is the band containing the carrier frequency. The detailed procedures of the proposed method are described in the following subsection.

4.3.1 Fault Diagnosis Method using LPNCC and Squared Envelope Spectrum (LPNCC-SES)

The LPNCC of each channel extracted through Section 4.2 can be used for analysis as a reconstructed time signal with the cyclic spectral component emphasized. In classical envelope methods, a frequency band including a carrier can be extracted through a pass-filter, and then demodulation is performed on the filtered time signal [15]; usually, demodulation is done by Hilbert transformation. Therefore, in this

study, as shown in the demodulation part of Figure 4-4, cepstral coefficients of each channel are regarded as a filtered time signal. Through the LPNCC-SES, it is possible to see as a whole whether each channel divided by the filterbank and the cyclic frequency in the frequency domain are well represented.

In the final step, fault diagnosis is performed by selecting the channel with the high energy and finding the bearing characteristic frequency of the spectrum. It is thus required to determine whether the peak of the defect frequencies is statistically significant in the spectra of the cyclic spectrum extracted by LPNCC-SES. To define the threshold, Leys et al. [96] presented the moving median absolute deviation (MAD) instead of thresholding by the 3-sigma rule. Depending on the stringency of the user's criteria, highly conservative detection of statistically relevant peaks in the spectra is based on three times the moving Median Absolute Deviation (MAD) of each spectrum, defined as described in Eq. (4.13) [97]

$$MAD = 1.4826 \times m[|\, x - m(x)\,|] \tag{4.14}$$

where $m(x)$ is the median of signal x. Because thresholds are not as sensitive to outliers as standard deviations, MAD is a powerful for outlier detection in probabilistic studies. Therefore, any value above the threshold can be considered statistically relevant candidates for frequency detection. Then, fault-related components can be more easily selected from the detected candidates in frequency domain.

4.3.2 Effect of Linear Filter and Power-normalization

To check the effectiveness of the LPNCC, actual bearing outer ring failure data were compared with linear frequency cepstral coefficients (LFCC) without power-normalization and PNCC with gammatone filter applied.

Figure 4-5 shows the cepstrogram of cepstral coefficients according to each method application and the spectrogram applied with SES. First, in the case of the the results of LFCC, the background noise is not sufficiently removed in each channel, so the effect of the rotation frequency compared to the hidden bearing and other periodic signals is large in about channel 5. Moreover, in the result of the PNCC case, the energy is concentrated in the low-numbered channels (up to channel 10) because the filter band is densely formed in the low-frequency band in a non-linear manner as shown in Figure 4-3. However, since there is no bearing-related resonant frequency in this area, BPFO due to the intended outer ring failure is not seen, and instead, BPFI, which is thought to be caused by modulation due to radial load, is seen in a channel with a lower number. In the case of the LPNCC–SES, energy is concentrated by focusing on bearing-related information in the vicinity of channel 11, and it can be confirmed that the peak of BPFO due to outer race failure is also well observed.

4.4 Experimental Application and Results

In this section, the applicability of the proposed study is studied through a numerical simulation and by examining three case studies. In Section 4.4.1, data description is presented including simulation data with white Gaussian noise and real world data from Case Western Reserve University's (CWRU) bearing data set [98]. In Section 4.4.1.1, the effect of LPNCC is demonstrated at various SNR levels by adding white Gaussian noise (WGN) to the mechanical vibration model defined in Section 4.1.2. Then, three experiments cases are selected from CWRU bearing data set and discussed with comparison of Randall's benchmark study [99]. First, the capability of the proposed method in the presence of impulsive noise is discussed in Section 0. In Section 4.4.2.1.3, the improvement of diagnostic performance is shown with low SNR. In the last case, the potential applicability of the proposed method for use in situations multiple defects is considered, as outlined in Section 4.4.2.1.4

Usually, the characteristic frequency of the inner and outer ring defects appears at about 1 to 5 times the rotation frequency; thus, in this study, the window size is set to observe the range of below 500 Hz using Hamming windows of duration 2 ms with a 0.5 ms frame period, using a DFT size of 1024. Each test case is set up to show the effectiveness of the proposed method in a specific situation.

4.4.1 Case Study with Simulation Model

4.4.1.1. Simulation Data with White Gaussian Noise

In order to demonstrate the proposed method's validity and robustness to noise, we studied a numerical simulation example. Recall that in Eq.(4.3) in Section 4.1.2, a theoretical bearing vibration signal with white Gaussian noise is simply modeled, as follows:

$$x(t) = \int_{-\infty}^{t} A_c e^{-c(t-\tau)} \cos(2\pi f_c(t-\tau))\, d\tau + A_s \sin(2\pi f_s(t) + \theta_s) + WGN \qquad (4.15)$$

The coefficients and their values used to generate the signal are summarized in Table 4-1. The length of the simulated signal is 3 s, with a sample rate 12000 Hz. The defective frequency that represents the bearing characteristic frequency (BCF) is set to 160 Hz to simulate outer race faults without consideration of impulse modulation from load distribution, which occurs in cases of inner race faults and ball faults. According to Peeters et. al. [60], neither the CPW or ACEP technique detect bearing failure for SNR values below -16 dB. In the case of the ACEP method, bearing failure detection was possible for SNR values above -16 dB, and in the case of CPW, failure detection was possible when SNR values exceed -11 dB. In this case, referring to Peeters' work, the SNR level of white noise was set to range from 5 dB to -15 dB.

For the raw signal in the time domain, the value of SNR ranges from 5 dB to -15 dB and the results of envelope analysis for the full bandwidth are shown in Figure 4-6. In the case of an SNR at the 5 dB level, the impulse is clearly visible, even in the raw signal of the time domain. Further, when looking at the results of envelope

analysis, BCF and its sidebands are clearly visible, as shown in Figure 4-6 (a). As the influence of the noise component on the original signal increases, it becomes difficult to observe the impulse in the time domain signal. However, in the frequency domain, as can be seen from the right side of Figure 4-6 (b), the peaks at the BCF are able to be distinguished at the level of -5 dB. However, when the value of the SNR reaches -10 dB, it is difficult to observe distinct peaks, even though the disturbed peak can be seen at 163 Hz near the 1 × BCF, as depicted in Figure 4-6 (c). the BCF are barely identified in the frequency domain by the conventional envelope analysis approach as depicted in Figure 4-6 (d)

4.4.1.2. Denoising Under Gaussian Noise

In Figure 4-7, the LPNCC cepstrogram, which provides a short-time cepstrum computation similar to a spectrogram, is presented for the simulated signal. For the purpose of processing signals with a sample rate of 12000 Hz, a 20-channel linear filterbank whose center frequencies are uniformly spaced between 0 Hz and 6000 Hz was used. As shown in Figure 4-7 (a), strong periodicity is seen in the ninth channel, which means a band of 2400 Hz to 2700 Hz, which is a reasonable result considering that the carrier frequency, f_c is 2500 Hz. Further, impulses seen in this band appear with a quefrency interval of 6.25 ms, corresponding to the defect frequency, 160 Hz. As mentioned in the previous paragraph, in the case of an SNR of -5 dB, a peak in the BCF can be seen in the case of the frequency analysis. Although it is somewhat smeared, periodicity can be observed in Figure 4-7 (b). However, as shown in Figure 4-7 (c) and Figure 4-7 (d), it is still difficult to visually distinguish the periodicity at the SNR levels of -10 dB and -15 dB in the feature

extraction stage. Therefore, in later in this section, fault diagnosis is performed through an LPNCC-based square envelope spectrogram for the cases of -10 dB and -15 dB.

As was mentioned in Section 4.3.1, each LPNCC of the uniformly distributed channel is demodulated through SES technique. The result of the SNR -10 dB case is illustrated with a three-dimensional graph of normalization of LPNCC-SES, as shown in Figure 4-8 (a), where the x, y and z axes represent cyclic frequency, channel from the uniformly distributed frequency filterbank, and normalized amplitude, respectively. A high-energy section, which was not seen well in the cepstrogram, was observed around the 9th channel, and a peak value was observed at a defect frequency of 160 Hz in the 9th channel.

In Figure 4-8 (b), a view of Figure 4-8 (a) from above, the cyclic frequency can be effectively observed. A strong peak at 160 Hz corresponding to 1 × BCF and a peak at 320 Hz of 2 × BCF, which is a harmonic component, is revealed in the 9th channel, which contains the carrier frequency and the nearby channels.

Although the failure has already been sufficiently asserted through the spectrogram, the signal can be more deeply analyzed by examining the spectrum of a specific channel in more detail. By examining the spectrum corresponding to the ninth channel, as shown in Figure 4-8 (c), it is possible to make more confident decisions about fault diagnosis. Here, it can be seen that the diagnosis result is statistically significant by using the 6-MAD, as mentioned in Section 4.3.1, as a criterion for the outlier selection. Also, compared with the result of Figure 4-6(c), the normalized amplitude at 1 × BCF (~163Hz by disturbed result) is 1, where the

MAD value has a value of 0.434. On the other hand, in Figure 4-8 (c), the normalized amplitude of 1 × BCF is the same as 1, but the MAD value is 0.245; this implies that the influence of ambient noise was significantly reduced.

For the SNR of the -15 dB case, which is the most severe noise condition, the above feature extraction process was performed, as shown in Figure 4-9 (a) and (b). In contrast to the case described above, it can be seen the defective frequency information is not clearly visible in the spectrum as the influence of noise increases; further, the prominent peak value is not seen. The only information available from the SES in Figure 4-9 (a) and (b) is that the spectral energy is concentrated in the 7th to 11th channels. As mentioned above, we already know that the carrier frequency value is 2500 Hz for the 9th channel; however, in practice it is difficult to know this information.

Under the assumption that there is no prior information about the carrier frequency, a detailed spectrum of the 7th to 11th channels are sequentially illustrated in Figure 4-10. For the 7th, 8th, and 9th channels, the fault frequency harmonics corresponding to the dotted lines were slightly larger than the 6-MAD threshold, as shown in Figure 4-10 (a-c); however, we cannot confidently say that a fault is diagnosable, even though the most prominent fault-related signals were detected at the BCF harmonics in the 9th channel for the former weaker noise cases. Looking at Figure 4-10 (d) and Figure 4-10 (e), it can be seen that the 1 × BCF component in the 10th and 11th channels are relatively remarkable, compared to the other channels; however, it still does not show a noticeable value in the whole spectrum. Furthermore, there are no components other than the rotation frequency, carrier frequency, and fault frequency; thus, it can be determined that the peak above the threshold that does

not correspond to the BCF harmonics is caused randomly by white noise.

In order to solve a situation to get a clear diagnosis result in a specific channel due to the influence of noise, it is possible to reduce the influence of random noise and to improve the information of the periodic signals associated with faults by averaging the above spectra, as represented in Figure 4-11. In the individual spectrum, the defect frequencies did not appear predominantly because they are buried by noise; however, the 1 × BCF could be clearly identified here, and the subharmonic value of the rotation frequency due to signal disturbance was also found to be around 20 Hz. The peak value at 1 × BCF is 0.458 with the MAD value is 0.400 in Figure 4-11, whereas the BCF are barely identified in the frequency domain by the conventional envelope analysis approach as depicted in Figure 4-6 (d). The results in Figure 4-11 assure that the proposed method successfully extracts fault-related features while mitigating the effect of operational noises. Because the deterministic fault-related features remain in all channels while the noise are randomly distributed in frequency domain, environmental noises also could be diminished by considering spectrum of SES-LPNCC from all channels. In addition, it can be found that the fault-related features with arbitrary carrier frequency could be successfully extracted without loss of information by the proposed linear filterbank.

4.4.1.3. Reseults Under Non-gaussian Noise

In order to verify the effect in a situation where deterministic signals are mixed, the method proposed in Chapter. 3.3 was applied to the synthesized signal. In Figure 4-12, the deterministic signal (e.g., gear) and cyclostationary signal (bearing) each show peaks through the spectrum of LPNCCSES above. The natural frequency of the deterministic signal was set to 3000 Hz and the bearing signal to 3500 Hz, and each of them has peaks in channels 30 and 35, so the signals can be separated and observed well. The spectrum of the 35th channel for more detailed analysis of the result is shown in Figure 4-12 below. Through this, it can be confirmed that only the bearing signal clearly appears beyond the MAD threshold.

4.4.2 Case Study with Experiment Data

4.4.2.1. Experimental Data: Case Western Reserve University Dataset

Over the past decade, CWRU data has been utilized countless times as a standard reference in fields of the bearing diagnosis and prognosis. The experimental setup, as depicted in Figure 4-13, comprises a Reliance Electric motor with 2 hp that rotates a shaft equipped with a torque transducer and an encoder. The shaft is subjected to torque by means of a dynamometer and an electronic control system. To find out the effect of defect size, faults were seeded separately on the ball, the inner race and the outer race of fan-end (FE) bearing and drive-end (DE) bearing, respectively, ranging from 0.007 to 0.040 inches in diameter. Vibration data was obtainedwith a sampling rate of 12000 Hz and 48000 Hz.

4.4.2.1.1. Compared Methods

Smith and Randall [99] presented an essential benchmark in which three diagnostic methods were studied for the CWRU data set, specifically: envelope analysis of the raw signal (M1), cepstrum pre-whitening (CPW) (M2), and discrete/random separation (DRS) followed by spectral kurtosis (SK) (M3). As a result, diagnosability of all CWRU data could be categorized into six classes, as detailed and shown in Table 4 2. After Smith and Randall's study established benchmarks, several studies considering the mechanical properties of CWRU data have been conducted to deal with potentially diagnosable (P) or non-diagnosable (N) datasets [61,100–103].

4.4.2.1.2. Case 1: Impusive Noise

The record 275 DE of CWRU is classified as P1 by M1 and M2, N1 by M3 [99]. This data was measured from the drive-end (DE) position in the condition of an inner-ring defect with a size of 0.014 inch of a 12k fan-end (FE) bearing operated under motor load 1 hp at 1772 RPM. As the transducer acquires acceleration at the drive-end position, the transmitted signal is attenuated through the device, making it difficult to use the signal to investigate the fault signature. In addition, the unexpected ball-pass frequency of the inner race for the drive-end (BPFI-DE), along with its sidebands, are also present in the SES. This might be related to misalignment of the drive-end bearing and not to a defect of the bearing [61]. Correspondingly, as shown in Figure 4-14, it can be seen that lots of impulsive noises are combined in the original signal.

Figure 4-15 displays the results of the LPNCC-SES for this case. By using the normalized amplitude of the LPNCC-SES calculated through the proposed method, the concentration of the spectral energy in the vicinity of the 10th channel could be revealed, as shown in Figure 4-15 (a) and (b). Accordingly, it is determined that the frequency band corresponding to the 10th channel, which has the highest spectral energy density, contains a lot of defect-related information. Therefore, in Figure 4-15 (c), the spectrum corresponding to 10th channel was analyzed to perform fault diagnosis.

The shaft frequency, and its harmonic component indicated by the dotted line, are well observed, and the 4/3 component of the rotation component is also observed in the vicinity of 40 Hz, which is major a characteristic of misalignment.

According to the information provided by the CWRU data center [98], the failure frequency due to an inner race fault of the fan-end bearing is 146.1 Hz, which is very close to 4 × fs (=147.7 Hz); thus, there is a possibility of misdiagnosis. However, the f_{BPFI} of the fan-end bearing indicated by dashed lines was exactly the same, and verification was possible with sufficient resolution. Furthermore, as can be seen more clearly in the vicinity of 290 Hz, the frequency difference between 10 $\times f_s$ (= 295.3 Hz) and 2 $\times f_{BPFI}$ (= 292.2 Hz) is larger, and it can be seen that a peak of 2 $\times f_{BPFI}$ exactly matches at 292.2 Hz.

Otherwise, as mentioned above, the characteristic frequency (BPFI-DE) of the inner race of the drive-end that is observed at 160 Hz and the amplitude of 1 × BPFI-DE is higher than the amplitude of 1 × BPFI-FE.

4.4.2.1.3. Case 2: Low Signal-to-noise Ratio (SNR)

In this case, 204 FE records from the CWRU dataset were chosen to examine the difficulty of extracting defect features in noisy environments, that is, in situations with a low SNR value (SNR = – 6.3229). This record contains the case of an 0.014 in. outer race fault at the drive-end with a 3 hp motor load, 48k sampling rate, and the shaft speed set to 1730 rpm. Also, as in the previous case, the transmitted signal is attenuated because it was measured at the fan-end location, away from the drive-end with the faulty bearing. In particular, there is no method to diagnose this record in the benchmark paper [99], such as evaluating N2, N1, and N1 by M1, M2, and M3, respectively.

The LPNCC-SES spectrogram of this case is depicted in Figure 4-16. The

normalized amplitude in Figure 4-16 (a) appears in large peaks in the 1st channel, and it can be seen that the trend of energy density is high in the 8th -14th channels. The cyclic frequencies that appear strongly in Figure 4-16 (b) are confirmed to be caused by the shaft frequency (fs = 28.8 Hz) and its harmonics; however, it is difficult to specify cyclic frequencies corresponding to the fault characteristic frequency (BPFO-DE = 103.4 Hz) of the outer race fault of the drive-end bearing.

As described in Figure 4-17, it is also difficult to find defect information through spectral analysis in a low-SNR environment. In Figure 4-17 (a), while high amplitude appears in the rotation frequency and harmonic component, it is difficult to observe the peak related to f_{BPFO}. It seems that there is a peak in the vicinity of the $2 \times f_{BPFI}$ (= 206.8 Hz) frequency; however, the peak's value (204.9 Hz) has a considerable difference, as shown in the zoomed figure. From the results of averaging the spectrum of the 8th - 14th channels in Figure 4-17 (b), only a few shaft frequency harmonics can be seen.

The low SNR is also a cause of this result, but this is because the rotation frequency component strongly affects the whole frequency, so the algorithm mainly responds to the shaft frequency. Therefore, LPNCC was analyzed by channel-wise normalizing in order to consider the influence of the failure-related components within each decomposed filter bank. As represented in Figure 4-18 (a), it can be seen that the shaft frequency dominates all channels except for channels 8-12, which have been influenced as much by other cyclic components, such as shaft frequency. This result is more evident in channels 9, 10, and 11, as shown in Figure 4-18 (b).

Figure 4-19 shows that f_{BPFO} can be detected through the channel-wise

normalized spectrum analysis results of channels 9-11, extracted from the above channel-wise normalized LPNCC-SES. In the case of 9th channel, the amplitude of the normalized value of $1 \times f_{BPFO}$ is 1, which shows that it appears clearly compared to other signals, as shown in Figure 4-19 (a). In Figure 4-19 (c), f_{BPFO} and its harmonic components are detected in the 11th channel; however, they are slightly masked due to their inherent weakness.

4.4.2.1.4. Case 3: Multiple Defective Signals

To validate the performance of the proposed method in the presence of multiple defects, record 222 DE of the CWRU dataset is used in this case. This record was originally created for diagnosing when a failure has occurred on a rolling element in a 12k drive-end bearing. According to Smith and Randall [99], results for this data record were classified as P1/Y2/Y2 by three benchmark methods M1, M2, and M3. However, the failure diagnosis result should be recognized additionally for an inner ring failure, which is presumed to be brinelling, which neither M2 nor M3 are able to diagnose [99].

The LPNCC-SES is plotted in Figure 4-20, where the highest spectral energy clearly appears at the 11th channel. Furthermore, we are able to determine a detailed result by examining the spectrum of LPNCC-SES in channel 11, as shown in Figure 4-21 Ball failure, which is originally intended, was diagnosed with the ball spin frequency (f_{BSF} = 141.1 Hz) marked with an asterisk. In addition, an unintended fault in the inner race was spelled out by f_{BPFI} (162.1 Hz) with square marks and $2\times f_{BPFI}$ with circle marks; further, their sidebands spaced at shaft speed (fs = 29.9 Hz) are clearly seen.

4.4.2.2. Experimental Data: Naturally Degradation Data

It can be challenging to analyze a set of data taken from the accelerated life test in SNU-SHRM laboratory [104]. Detecting naturally occurring defects with accelerated life testing is more difficult than detecting artificially-seeded defects because of the increased uncertainty. If it is carried out successfully, it will be possible to develope a failure prognosis technique in the future through quantitative analysis results with continuously degradation data.

Test-bed setup is shown in Figure 4-22. An angular contact ball bearing (NSK 7202A) is used for accelerated life test with supported by two ball bearings (NSK 7205A) and two roller bearings (NSK NF207). The vibration of bearing is measured on bearing housing using a tri-axial accelerometer (PCB, Model 356A15). The temperature of test bearing is sensed by the thermocouple equipped on the bearing outer race. The measured vibration signals were sampled at 10 kHz with 15 seconds interval. At the end of the experiment, spall occurred on the inner-race. In each case, the length and width measured by the laser microscope as shown in Figure 4-23. Four tests were conducted under the same operating conditions, all of which stopped due to spall on the inner ring, and each defect information and life information are summarized in Table 4-3.

Even though tests were conducted under the same conditions, the size and life of the samples showed a significant difference. Also, the size of spalls and lifespan were not proportional, as shown in Table 4-3 and Figure 4-24. However, data utilization was intended for early diagnosis of defects, so 100 observation points were targeted in each case before the inspection was stopped. The results of statistical features for 100 samples prior to the end of the test are depicted in Figure

4-25. In all indicators except the crest factor, a sharp rise in amplitude was observed as it got closer to the endpoint. However, in each case, a simple increase in energy cannot be identified as a bearing failure, and it is challenging to set an alarm point unless a threshold value is determined in advance. Therefore, as shown in Figure 4-26, by observing the amplitude of each frequency component over time through the envelope spectrum, it is possible to track the deterioration of the bearing by checking the growth of energy at the BCFs. However, it is still difficult to distinguish the point that failure begins clearly.

Therefore, to confirm the point of the incipient fault appears, it is helpful to normalize the envelope spectrum at the observed point in time to determine which frequency components has energy concentrated over the entire frequency band. The detection of bearing frequency by tracking the dominant frequency sequence change over time can be physically explained as the initiation of cracks, spalls, or other surface defects within the bearing that cause it to oscilate at a new natural frequency and mode [105]. To confirm this, the envelope spectrum obtained through LPNCC-SES for the second test was normalized, and the frequency components corresponding to the peak points at each measurement point are shown in the Figure 4-27. The black dot marked the maximum 5 points, the blue circle marked the maximum 3 points, and the last point with the most energy was marked with a red asterisk. Through the trend analysis in the time domain of Figure 4-25, the dominant frequency trend at the 60th point before stopping is concentrated in the harmonics of the BCF, while a preset threshold is required to select the anomaly point. Through this, it is possible to select a defect detection point that can be more physically explained through a frequency change of the normalized envelope spectrum. The

results of the normalized envelope spectrum of the proposed method and other signal preprocessing techniques is discussed in more detail below.

The envelope spectrum was normalized with respect to the amplitude of the frequency domain better to see the influence of the BCF. As a result, the dominant frequency component at each sample point changes according to the lifetime. The results of the envelope spectrum without preprocessing, the preprocessing with wavelet denoising and CPW, and the spectrum extracted with LPNCC-SES were compared (Figure 4-28 to Figure 4-31). In the case of LPNCCSES, since it is difficult to extract the spectrum of a specific channel for each sample, the average spectrum value of all channels except for the low-frequency channel was used.

Consequntly, the anomaly detection point could be seen more quickly and clearly by LPNCCSES, especillay for bearing 4 (Figure 4-31). Furthermore, it is robust against outliers from the result of the other method at sample point 42 of bearing 2, an unintended horizontal line is seen due to outliers as shown in Figure 4-29. In all cases, wavelet denoising did not works well relatively for detecting anomalies since other periodic components, i.e. deterministic component, making it difficult to observe the BPFIs. As discussed in the previous chapter 3.3, it was confirmed that the performance of wavelet denoising was lower than that of the case without preprocessing. In the case of preprocssing by CPW, overall performance was good in all cases. In particular, in the case of bearing No. 3 (Figure 4-29), the clearest BPFI 1x (157 Hz) component separation compared to other methods can be observed. However, while BPFI was clearly observed, sideband components were not observed well. However, in the LPNCCSES results, sideband components were also observed at the anormaly detection point around 40 points.

Table 4-1 Summary of coefficients used in the numerical simulation.

Coefficients	Values
Carrier frequency, f_c	2500 Hz
Defect frequency, 1/τ	160 Hz
Amplitude of carrier signal, A_c	5
Amplitude of shaft modulation, A_s	1
Shaft modulation frequency, f_s	30 Hz
Initial angle of shaft frequency shift, θ_s	0°
Damping coefficient, c	0.05

Table 4-2 Categorization of diagnosis outcomes [99]

Diagnosis category	Diagnosis success	Explanation
Y1	Yes	Data clearly diagnosable and showing classic characteristics for the given bearing fault in both the time and frequency domains
Y2	Yes	Data clearly diagnosable but showing non-classic characteristics in either or both of the time and frequency domains
P1	Partial	Data probably diagnosable; e.g., envelope spectrum shows discrete components at the expected fault frequencies; however, they are not dominant in the spectrum
P2	Partial	Data potentially diagnosable; e.g., envelope spectrum shows smeared components that appear to coincide with the expected fault frequencies
N1	No	Data not diagnosable for the specified bearing fault; however, other problems are identifiable (e.g., looseness)
N2	No	Data not diagnosable and virtually indistinguishable from noise, with the possible exception of shaft harmonics in the envelope spectrum

Table 4-3 Summary of SNU test results and defect size information

Test No.	Life Time (Samples)	Defect Profile (μm) L:length; W:width; D:depth	
1	3,183	L	412
		W	731
		D	66
2	1,536	L	616
		W	503
		D	44
3	3,634	L	600
		W	715
		D	80
4	1,873	L	831
		W	551
		D	106

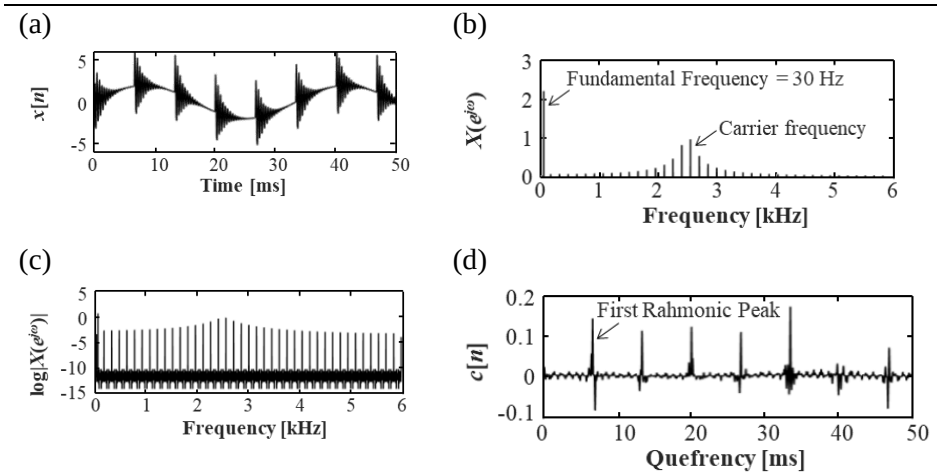

Figure 4-1 Response of a simulated signal with resonance frequency, fc = 2000 Hz, fundamental frequency fs = 30 Hz, damping ratio, c = 0.05, characteristic frequency (impulse) = 150 Hz, sampling rate = 12000 Hz. (a) raw signal, (b) DTFT, (c) log-magnitude of DTFT, and (d) cepstrum

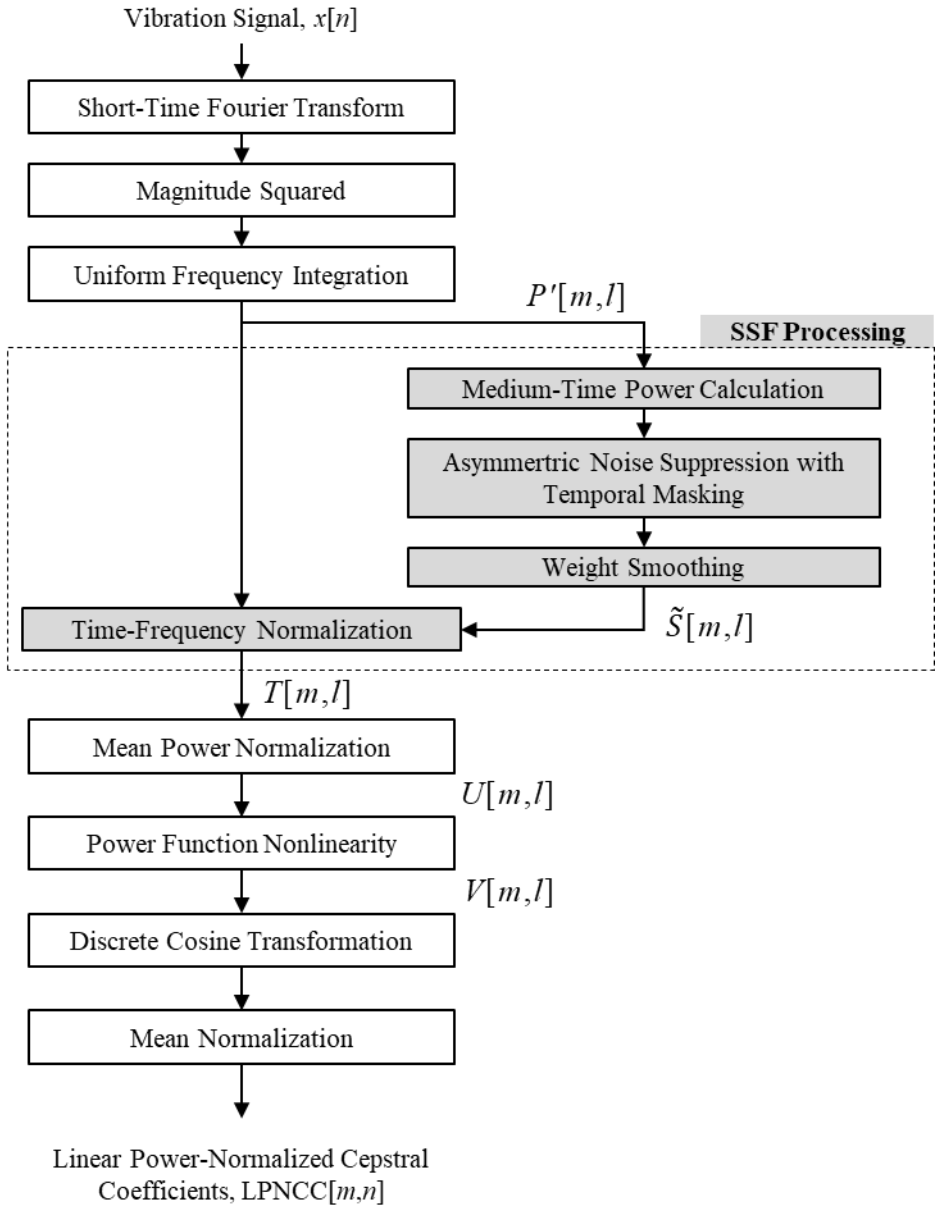

Figure 4-2 Structure of the LPNCC feature extraction algorithm.

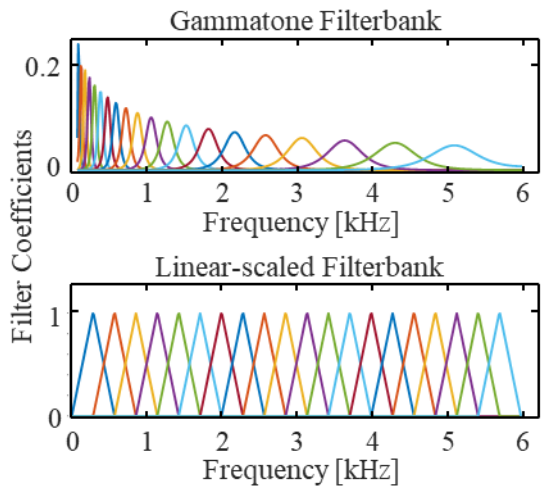

Figure 4-3 Gammatone filterbank and linear-scaled filterbank.

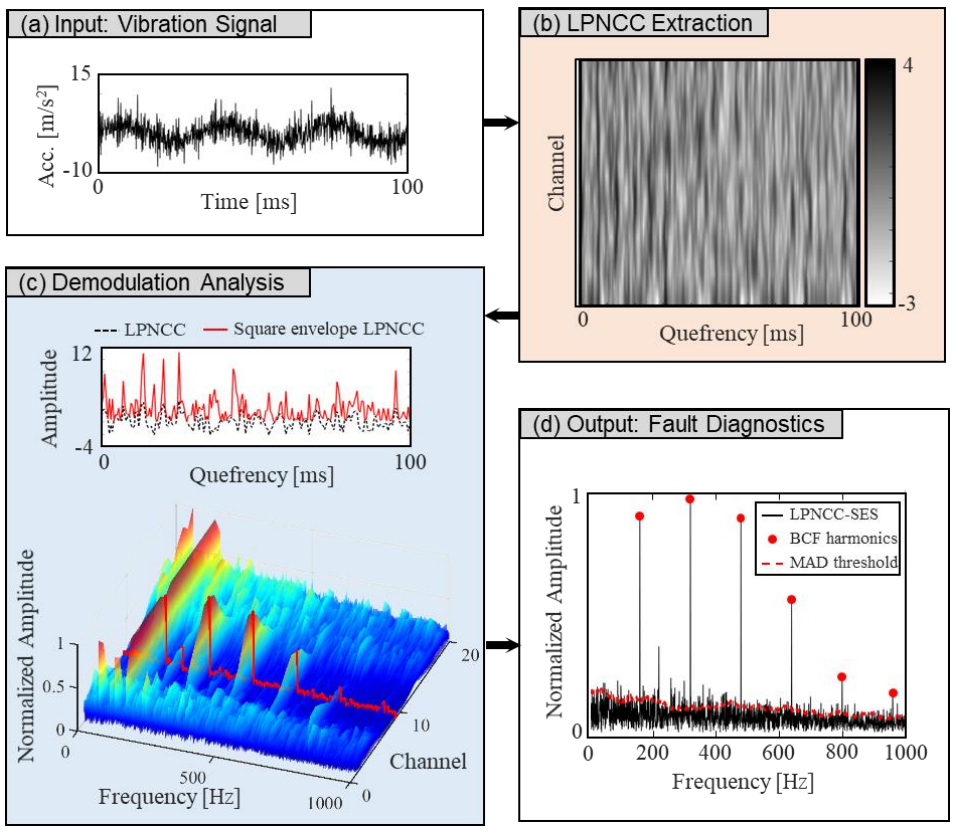

Figure 4-4 Schematic description of the LPNCC-SES.

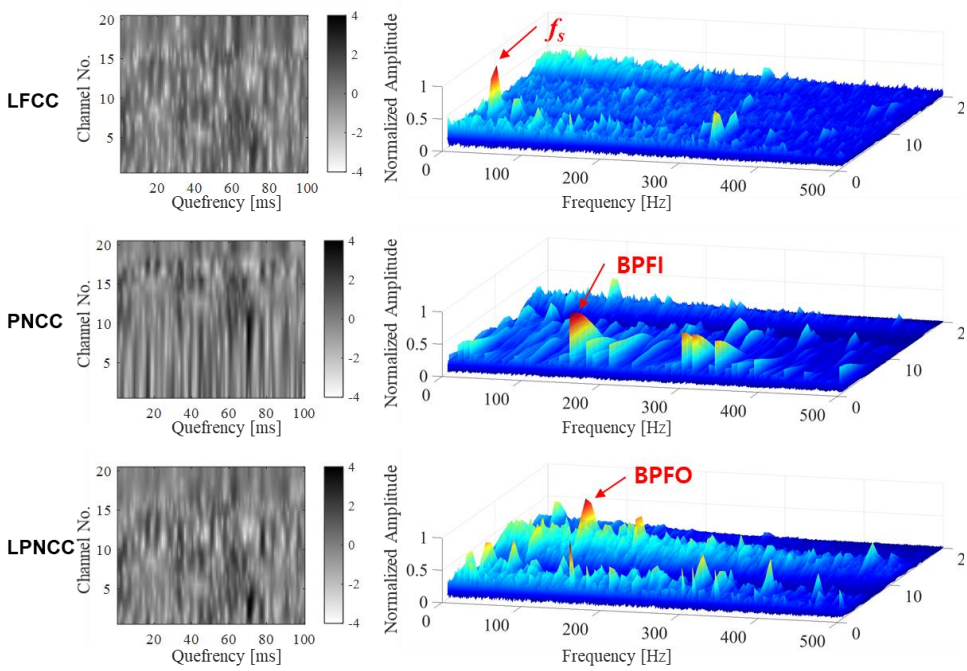

Figure 4-5 Effect of linear filter and power-normalization application

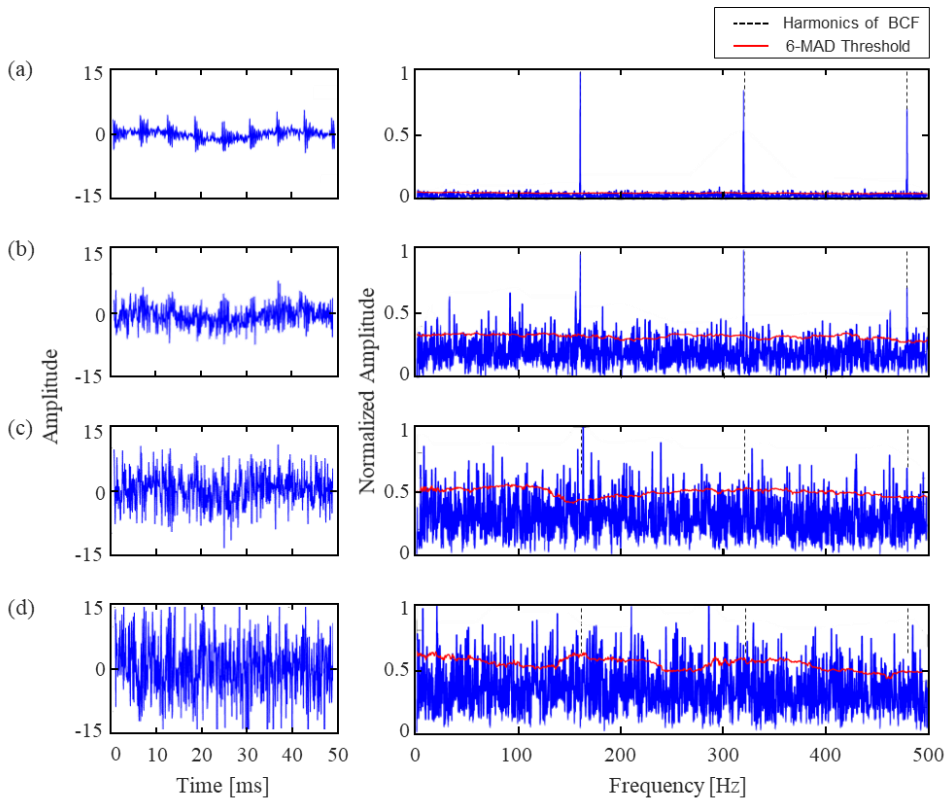

Figure 4-6 The time-domain signal (left) and envelope spectra (right) of simulation signal with various SNR level. (a) SNR = 5 dB, (b) SNR = -5 dB, (c) SNR = -10 dB and (d) SNR = -15 dB

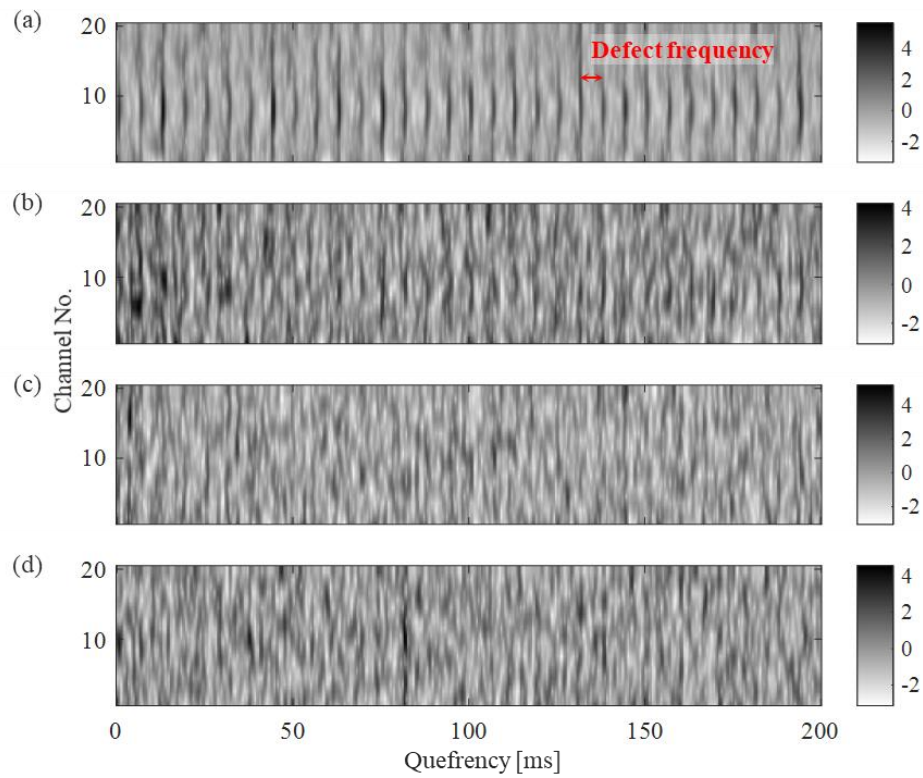

Figure 4-7 LPNCC cepstrogram of simulation signals. (a) SNR = 5 dB, (b) SNR = -5 dB, (c) SNR = -10 dB, and (d) SNR = -15 dB

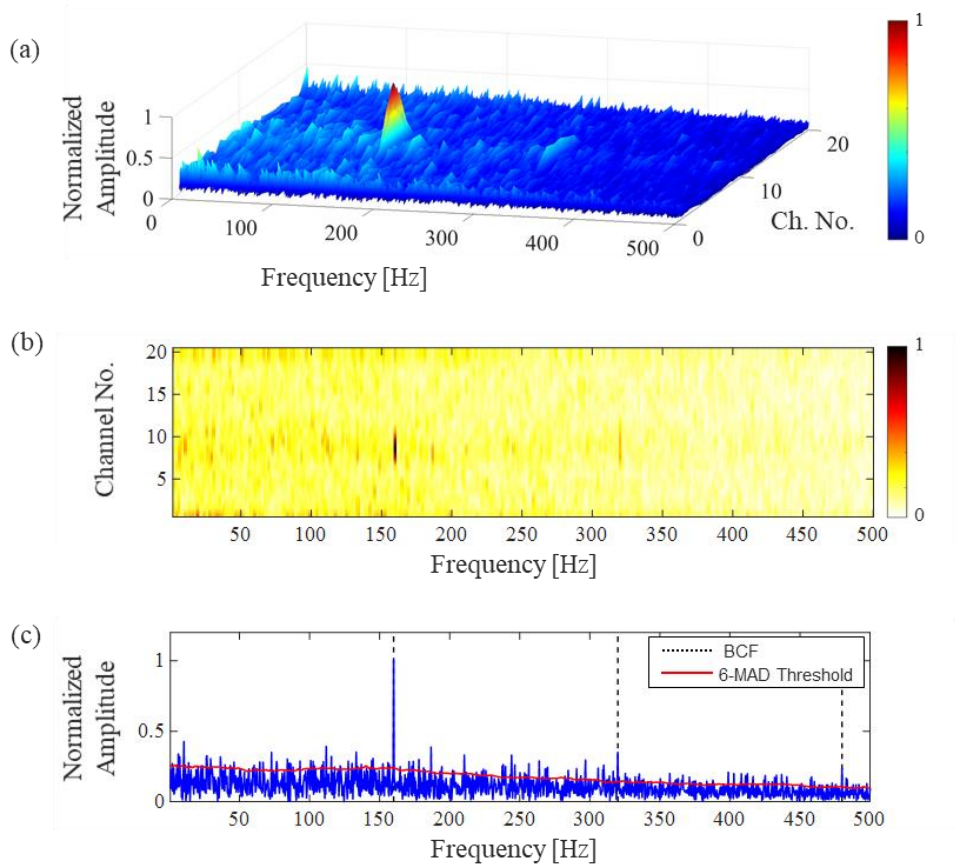

Figure 4-8 Square envelope spectrum of LPNCC (SNR = -10 dB), (a) 3D plot, (b) view of (a) from above, and (c) spectrum of the 9th channel

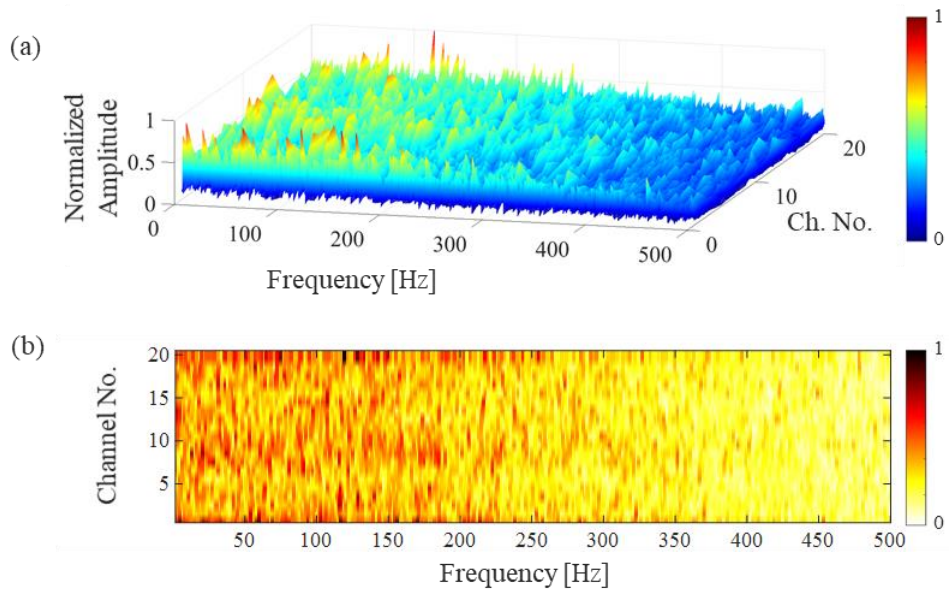

Figure 4-9 Square envelope spectrum of LPNCC (SNR = -15 dB), (a) 3D plot, and (b) view from above

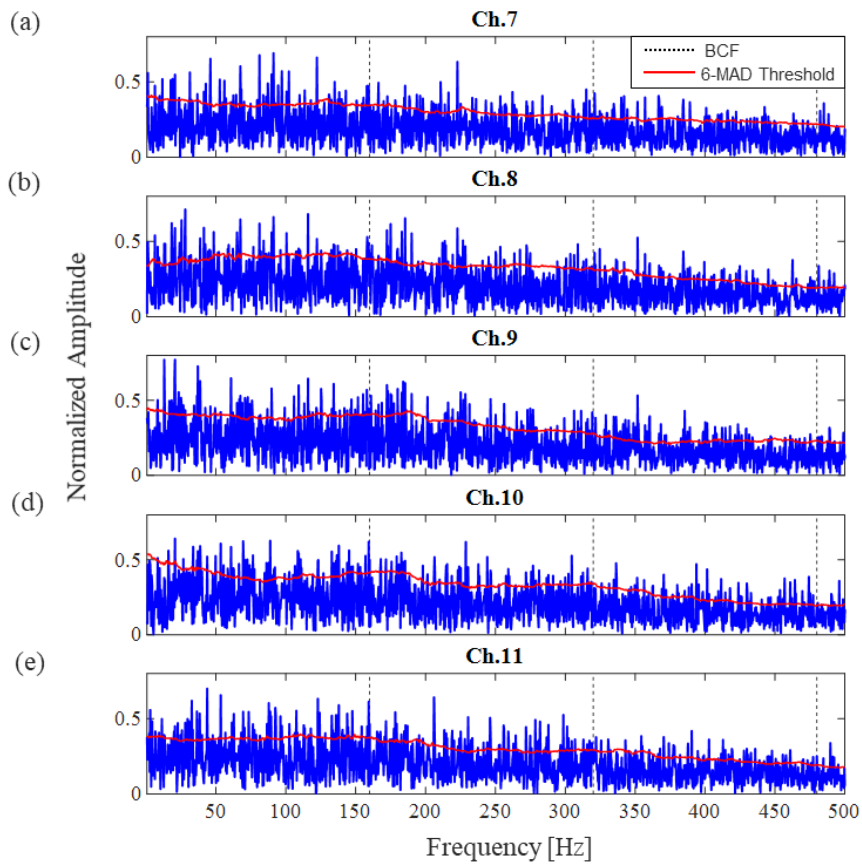

Figure 4-10 SES-LPNCC (SNR = -15 dB) (a) Ch. 7, (b) Ch. 8, (c) Ch. 9, (d) Ch. 10, and (e) Ch.11

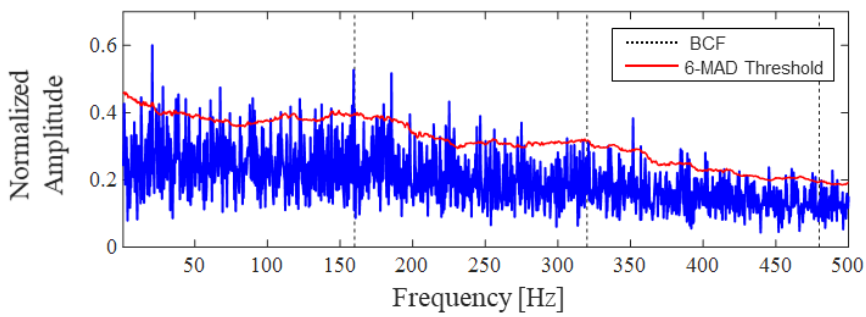

Figure 4-11 Average spectrum of SES-LPNCC (SNR = -15 dB) for Ch.7-11

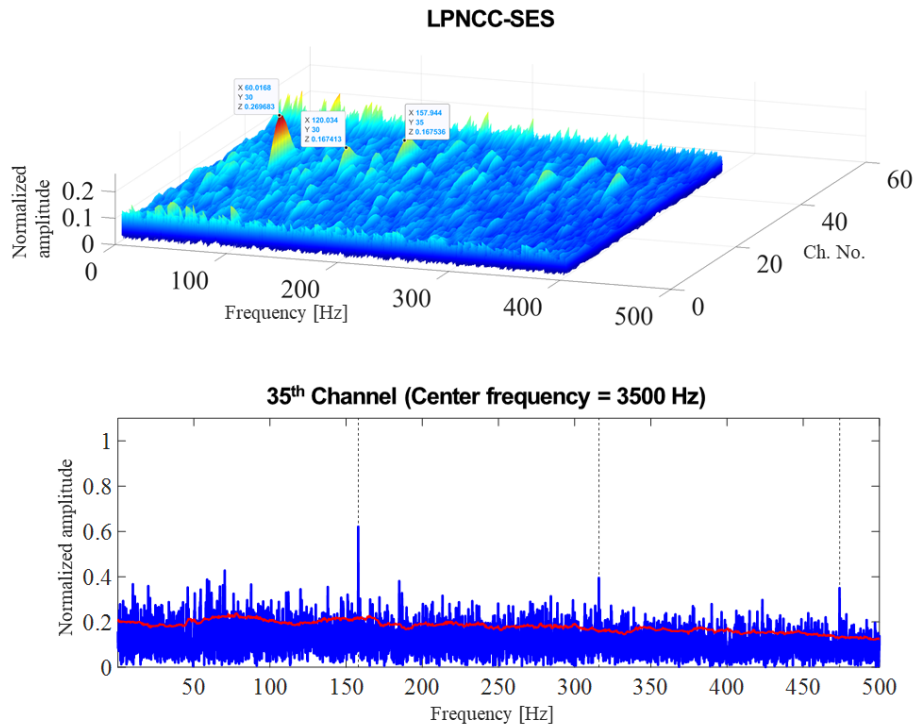

Figure 4-12 Non-Gaussian Case: Square envelope spectrum of LPNCC and spectrum of Ch.35

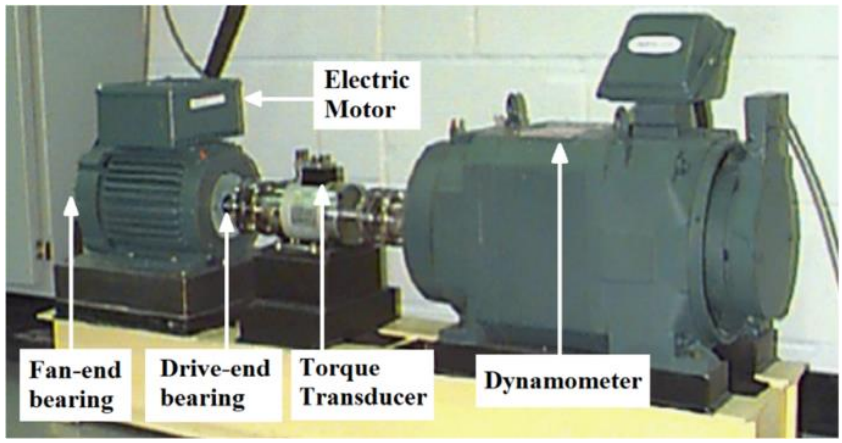

Figure 4-13 Configuration of CWRU test rig [98]**.**

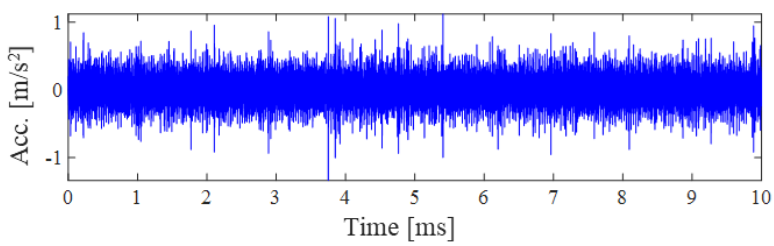

Figure 4-14 The acceleration signal of record 275 DE

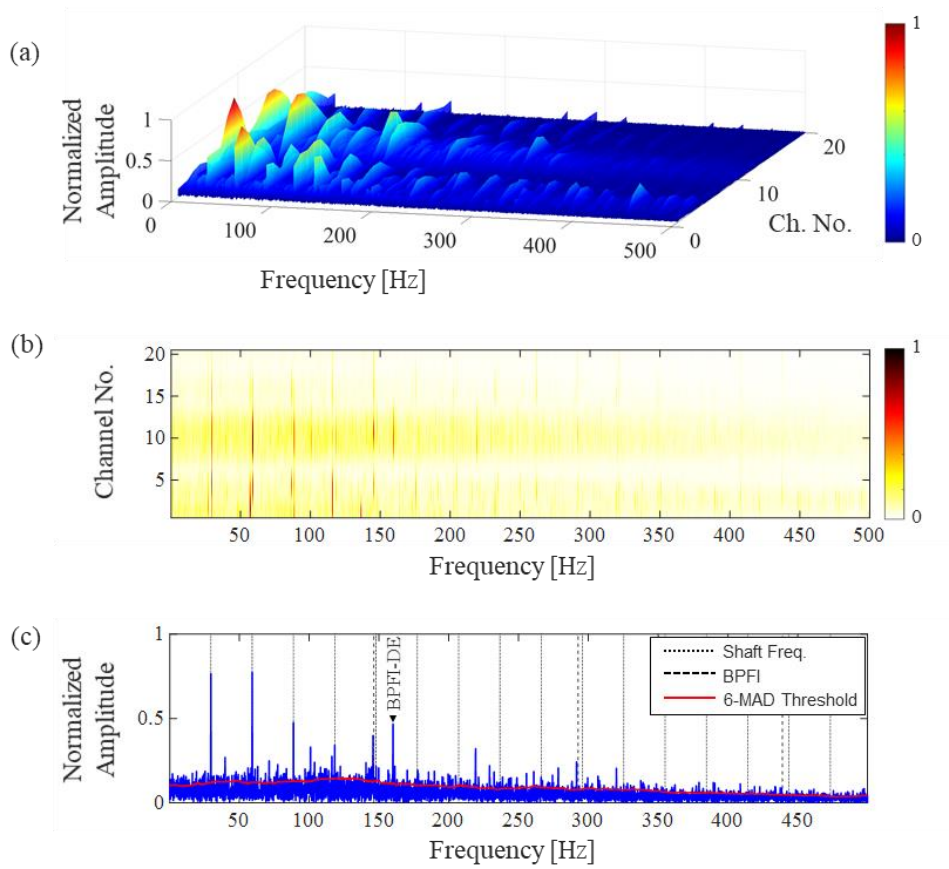

Figure 4-15 Case 1 - 275 DE: Square envelope spectrum of LPNCC, (a) 3D plot, (b) view from above, (c) spectrum of the 10th channel

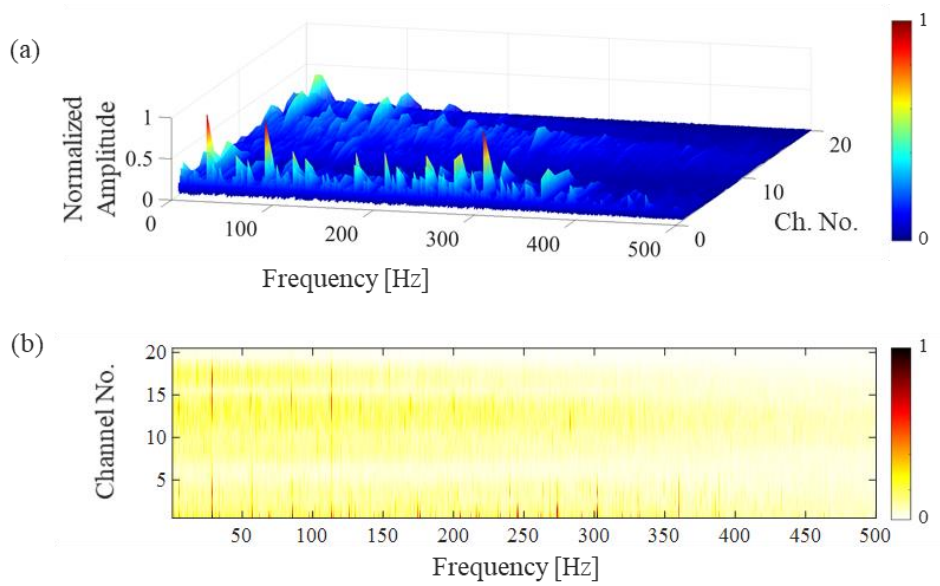

Figure 4-16 Case 2 - 204 FE: Square envelope spectrum of LPNCC, (a) 3D plot, (b) view from above

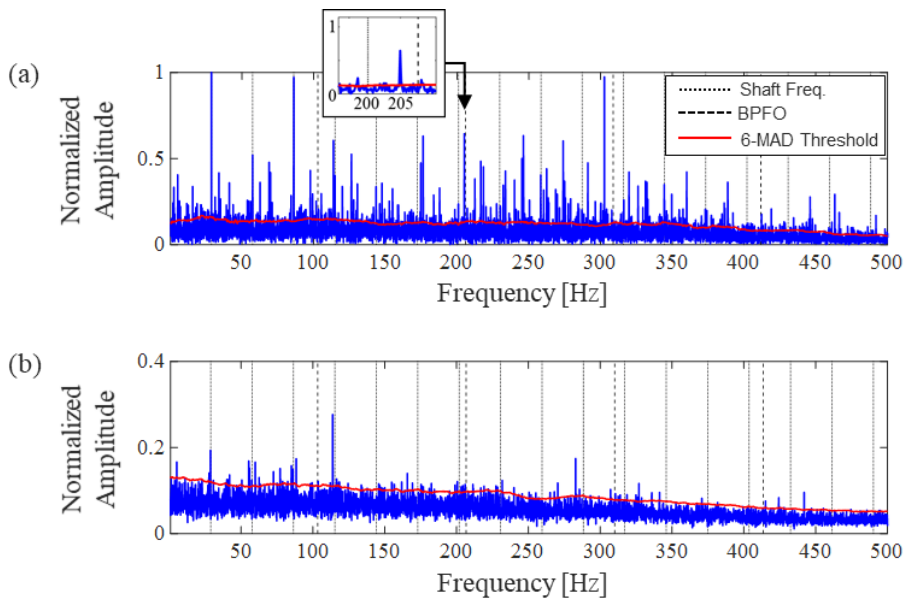

Figure 4-17 LPNCC-SES for case 3 (a) channel 1, (b) averaging of channels 8-14

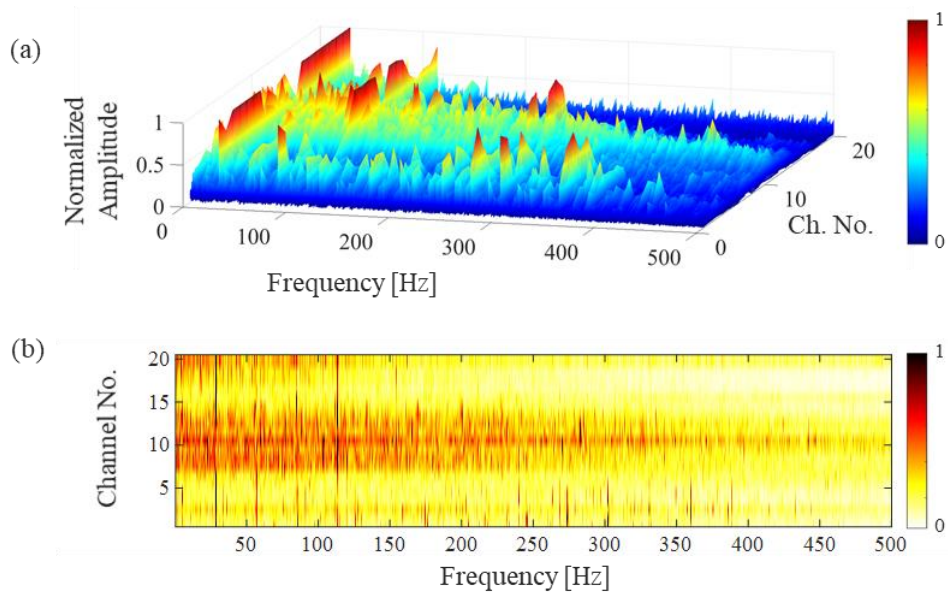

Figure 4-18 Channel-wise normalized LPNCC-SES (a) 3D plot, (b) view from above

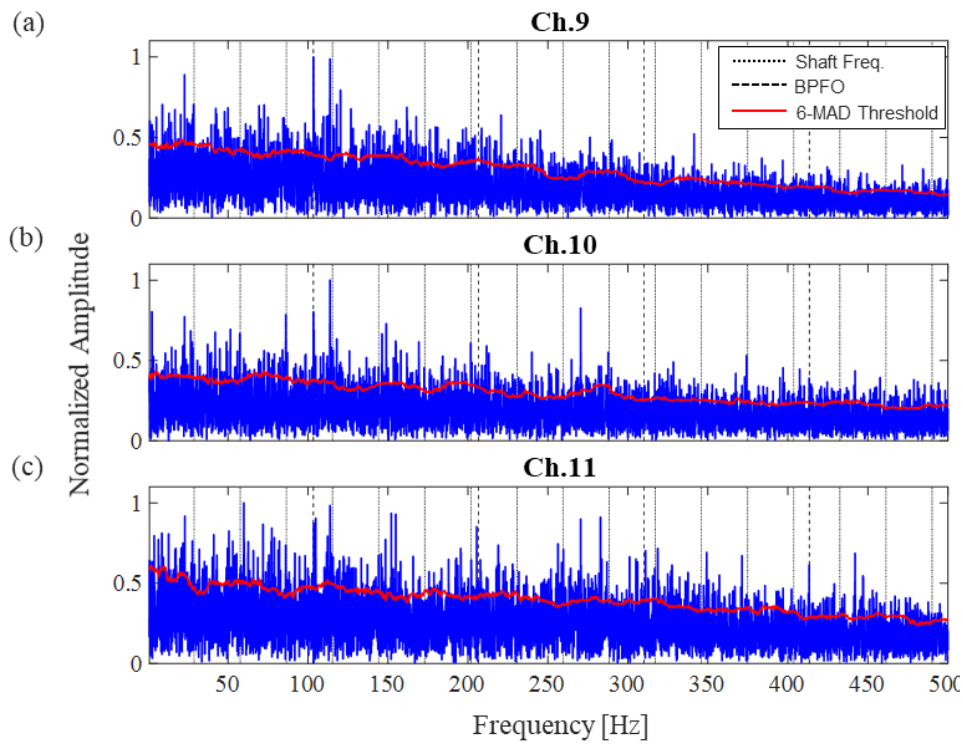

Figure 4-19 Channel-wise normalized spectrum of LPNCC-SES (a) Ch. 9, (b) Ch. 10, (c) Ch. 11

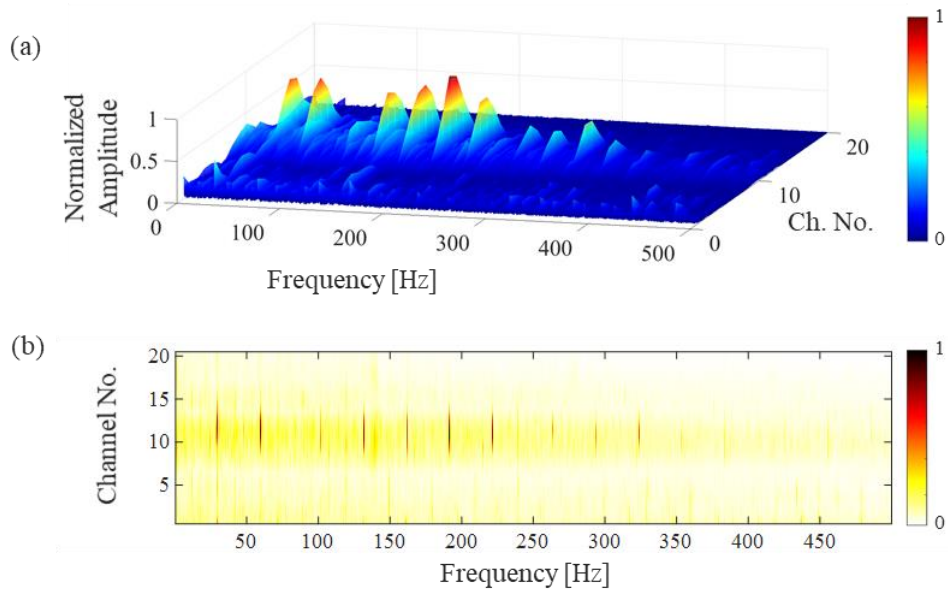

Figure 4-20 Case 3 - 222 DE: Square envelope spectrum of LPNCC (a) 3D plot, (b) view from above

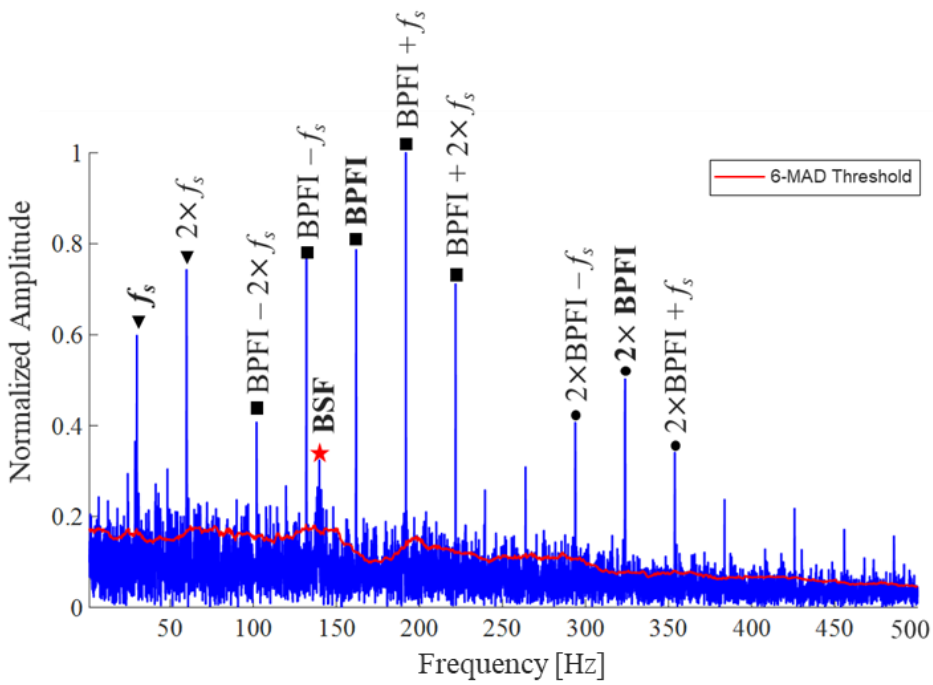

Figure 4-21 Spectrum of LPNCC-SES in the 11th channel

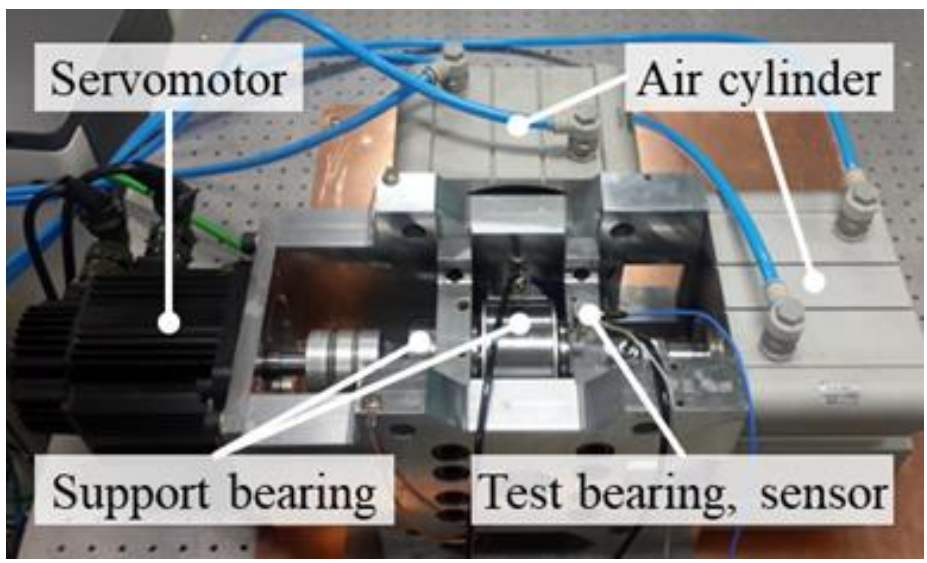

Figure 4-22 Configuration of SNU accelerated life test rig

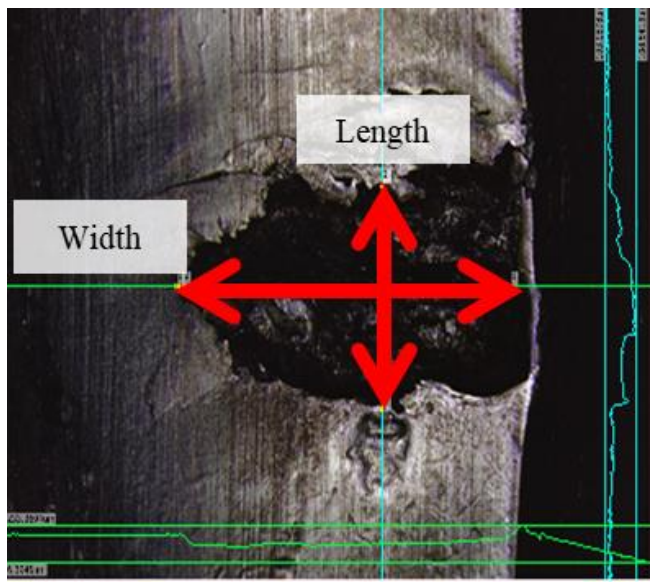

Figure 4-23 Micrograph of spall on the inner ring surface

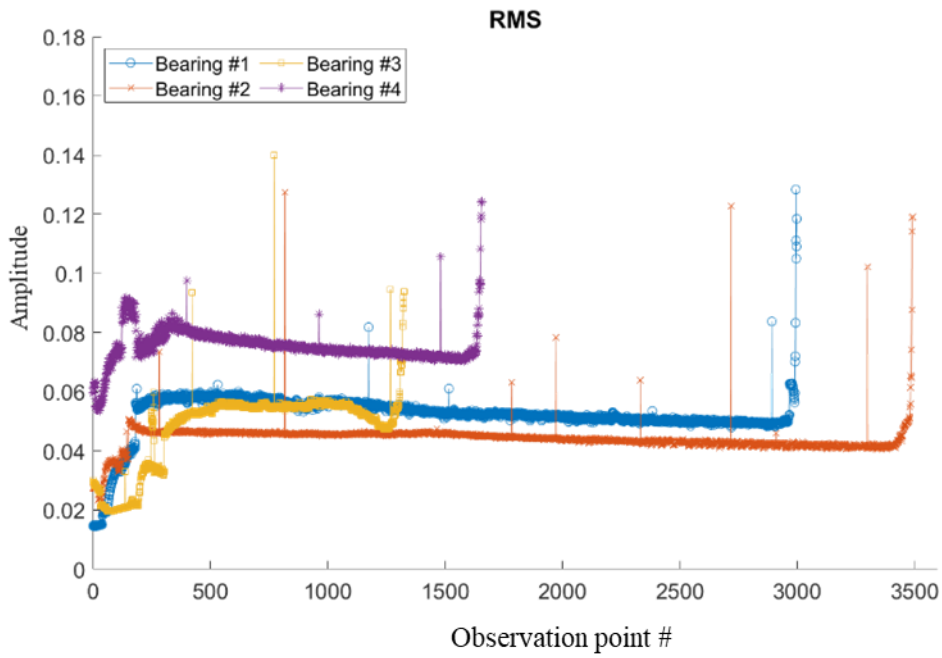

Figure 4-24 RMS trend of bearing signal as a result of accelerated life

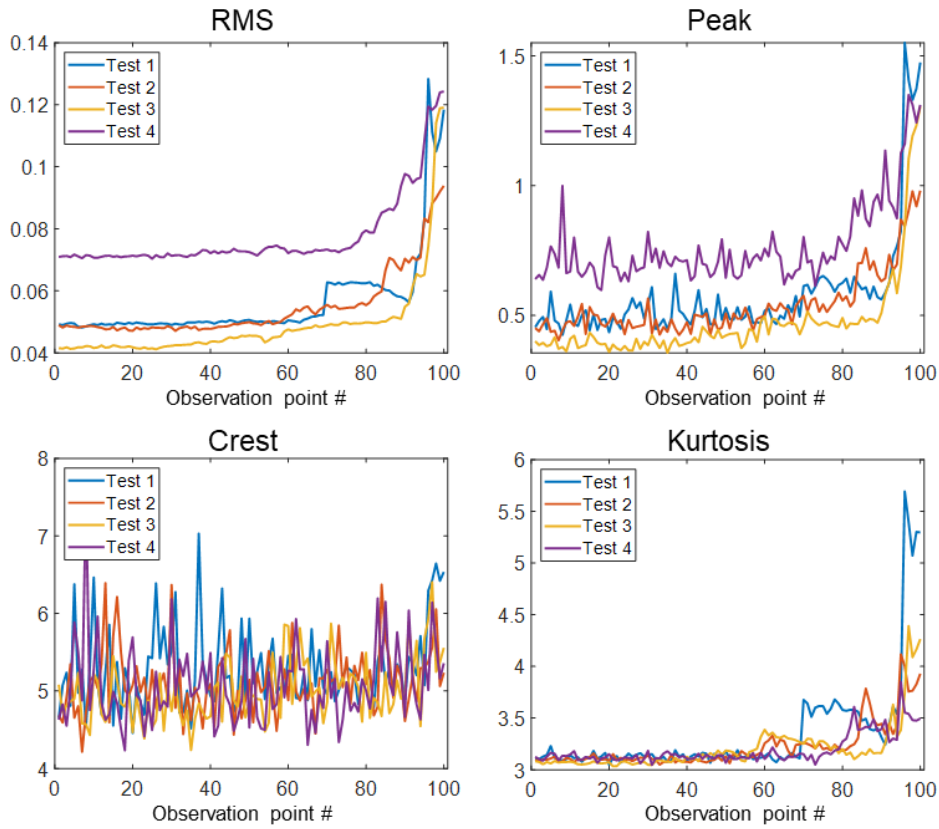

Figure 4-25 The results of statistical features for 100 samples prior to the end of the each test

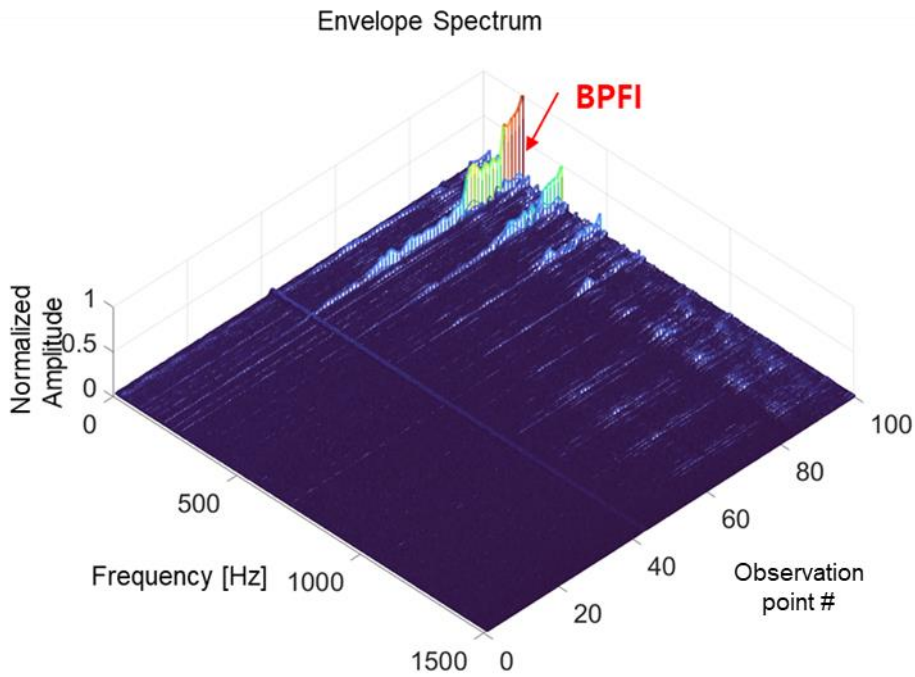

Figure 4-26 Envelope Spectrum of Bearing 2

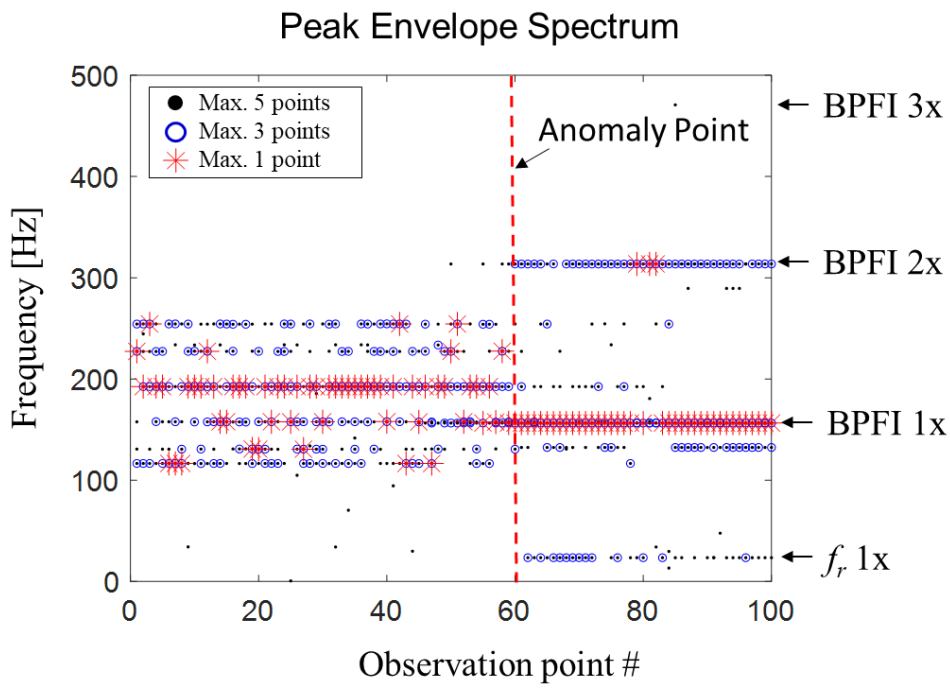

Figure 4-27 Peak envelope spectrum of normalized LPNCC-SES of Bearing 2

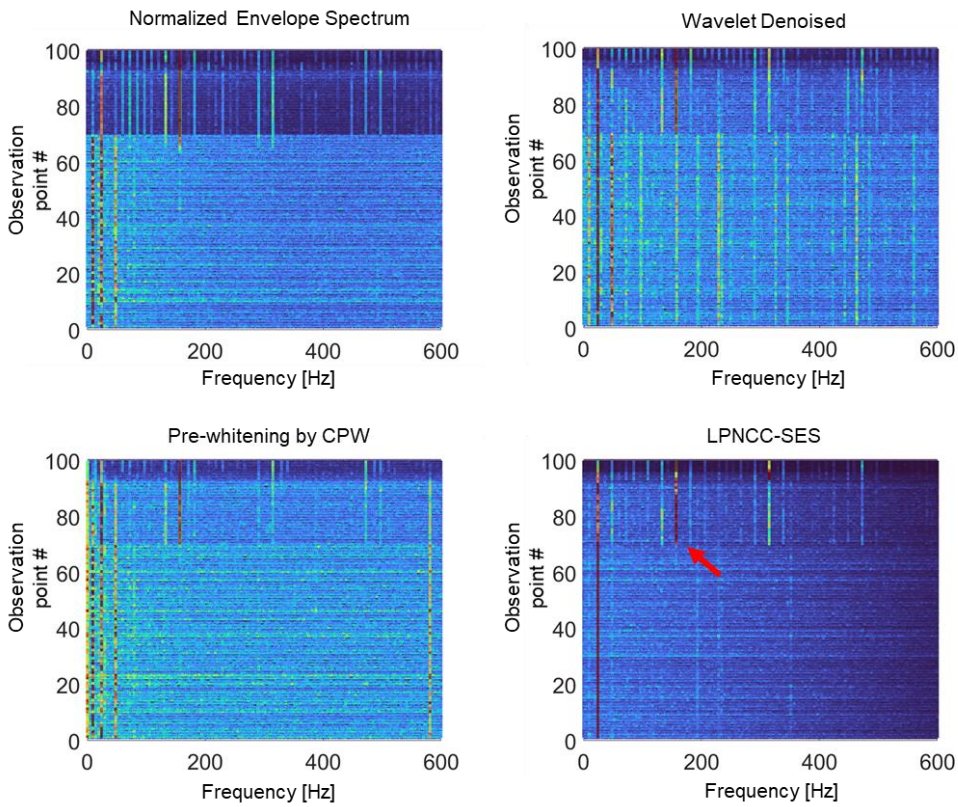

Figure 4-28 Normalized Spectrum of Bearing 1

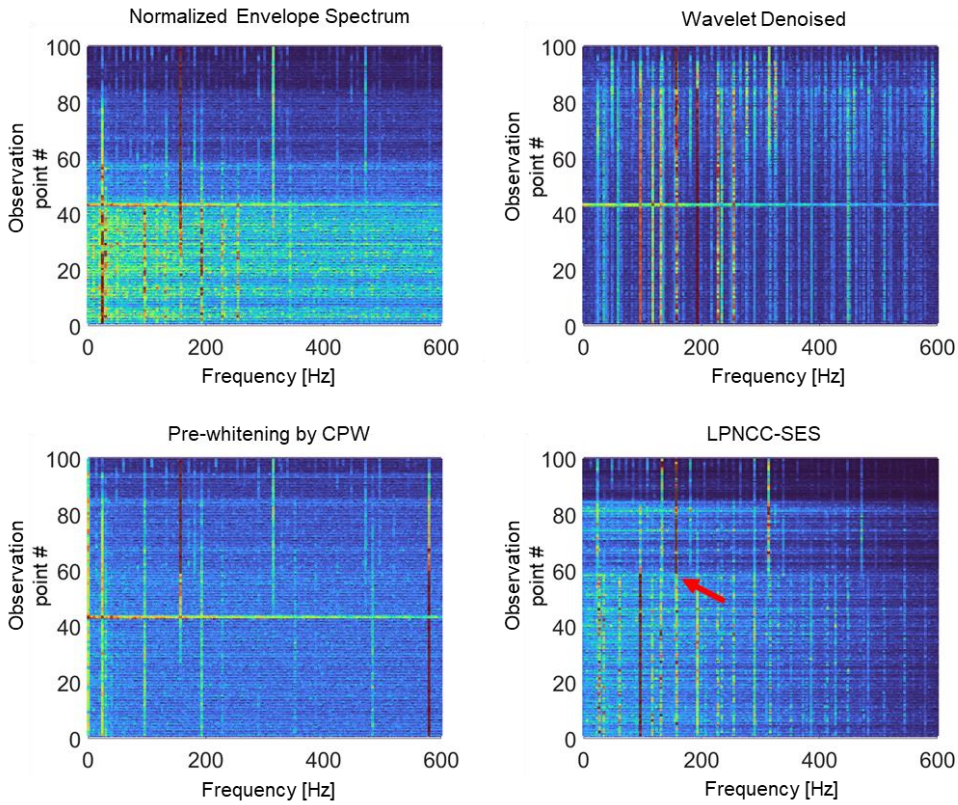

Figure 4-29 Normalized Spectrum of Bearing 2

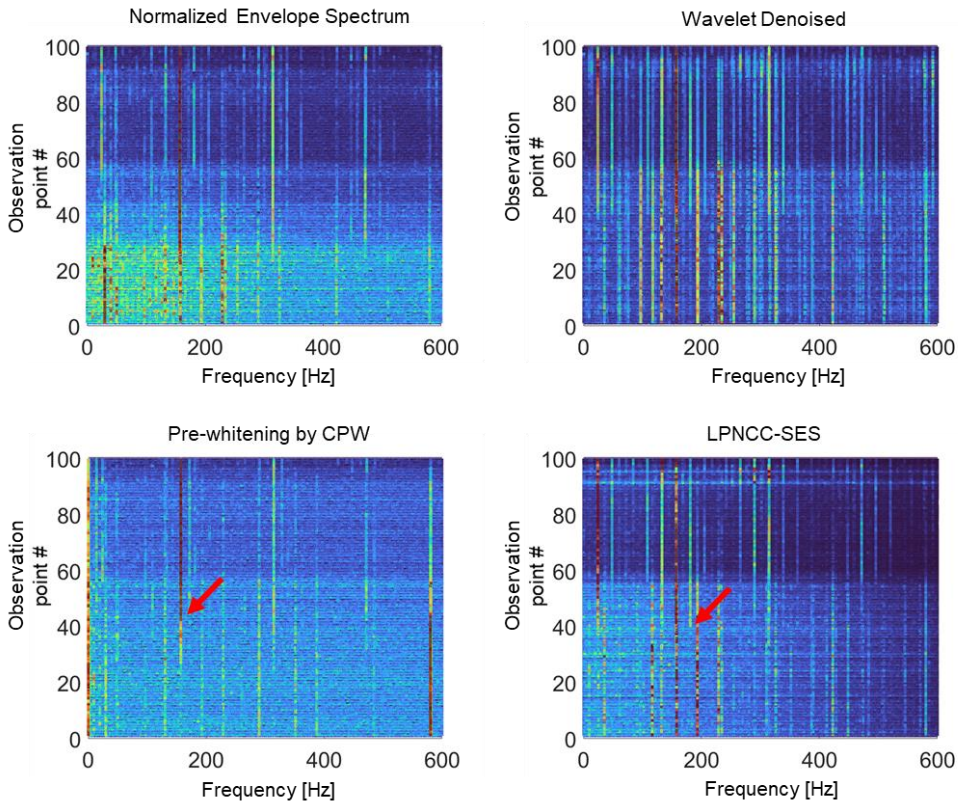

Figure 4-30 Normalized Spectrum of Bearing 3

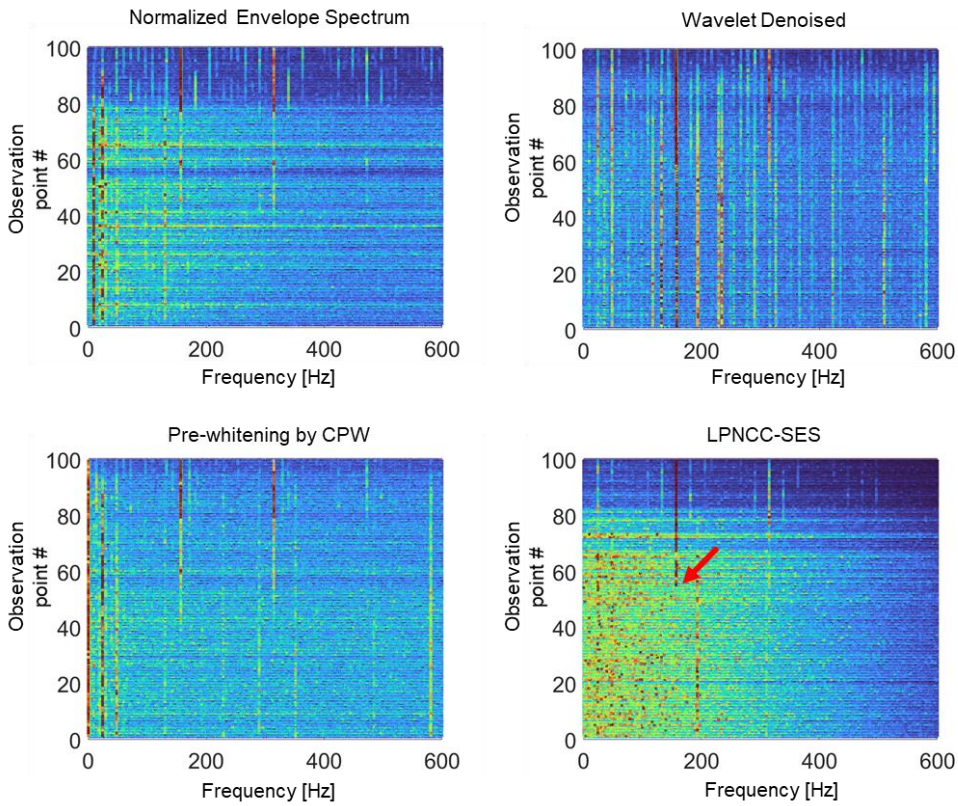

Figure 4-31 Normalized Spectrum of Bearing 4

Conclusions

5.1 Summary of Dissertation

This chapter presents a summary of the contents of this doctoral dissertation. To effectively diagnose in the incipient fault stage of rolling element bearings (REBs), with consideration of the vibration generation mechanism, two main research areas were proposed: signal generation and feature extraction with a demodulation method.

In the first chapter, the motivation for this dissertation and the corresponding research topics were introduced. Chapter 2 provides an overview of vibration-based diagnosis, including an overview of the required he basic knowledge of REBs, the characteristics of REB vibration, and various previously proposed vibration-based diagnosis techniques.

Chapter 3 proposes a quasi-periodic impulse train model with impact force function that can simulate a signal similar to the signal obtained during the incipient fault stage of REBs in practical settings. First, the stochastic nature of REBs' signal was modeled as a pseudo second-order cyclostationary signal using the quasi-periodic impulse train model. Second, the changes of Hertzian contact stress between the rolling element and the races were modeled using the impact force function.

Third, a synthetic signal was generated, including a pseudo second-order cyclostationary signal (bearing), a deterministic signal (gear), a sinuous inference signal (rotating shaft), and Gaussian white noise. Next, the characteristics of proposed signal model were discussed, along with various signal preprocessing methods. Finally, a signal model was proposed; the proposed model is well-suited for simulating the vibration characteristics of REBs during the incipient fault stage with numerical results. Further, through the research conducted, it was concluded that an appropriate preprocessing technique, such as cepstral prewhitening (CPW), is needed to accurately diagnose REB faults in the incipient stages.

Chapter 4 introduces a novel feature extraction method called linear power-normalized cepstral coefficients (LPNCC) and also presents a new fault diagnosis method by implementing LPNCC on the squared envelope spectrum (SES). This approach was inspired by a speech recognition technique that is based on auditory physiology. The process of this speech recognition technique is similar to the vibration signal processing technique, which is based on the vibration generation mechanism of REBs. The performance of the proposed LPNCC-SES method is thoroughly validated and examined in this research through its application to both simulation and real-world data. Of particular note, the proposed method was shown to be successful in diagnosing REBs under low-SNR and various noise conditions, where existing methods have failed. Additionally, using degradation data, the LPNCC-SES approach was demonstrated to be effective for early diagnosis of failures. These results confirm the promise of the LPNCC-SES method for the diagnosis of bearings under noisy operating conditions in the incipient fault stage, and expand the potential of cepstrum coefficients in this context.

5.2 Contributions and Significance

Timely prediction of bearing faults is of great importance to efforts to minimize unscheduled machine downtime in real-world settings. For successive diagnostics of REBs, it is necessary to achieve deeper understanding of their physics and to find more effective features in the measured data. This doctoral dissertation highlights the possibility of improving diagnosis by proposing a signal model and feature extraction and diagnosis techniques. This doctoral research offers the following potential contributions:

Contribution 1: Reduction of the gap between the theoretical signals and the actual signals of REBs

In this study, we examined the use of transient vibrations in rolling bearings as a means of detecting incipient faults. We found that the signals generated by these vibrations are non-stationary in nature; further, we determind that the signals are characterized by cyclostationary and shock impulses that result from changes in the contact stress of the rolling elements and inner/outer races around the defect. To model these physical phenomena effectively, we attempted to combine the strengths of the impulse train model and the dynamic model, two representative existing methods of studying the bearing signal generation model. We derived a quasi-periodic impulse train model with an impact force function to bridge the gap between theory and reality. Simulation of faulty bearing signals was useful for evaluating new diagnostic algorithms that were designed to identify specific features that may only

appear under certain conditions. By using this approach, we were able to improve our understanding of how fault symptoms are produced, particularly when non-linear interactions are present. We validated our signal model by testing it with processing synthesized signals using a signal preprocessing method and a bandpass filter, which helped to further our understanding of bearing signals and explore the potential of using them as reference signals. Overall, these simulations were valuable for improving our understanding of faulty bearing signals and developing effective diagnostic approaches.

Contribution 2: Development of a robust feature extractor that effectively detects weak nonstationary bearing signals

As discussed in Chapter 3, the weak vibration signal emitted by bearings during the incipient fault stage is often masked by background signals, resulting in limitations to traditional denoising methods due to their inability to accommodate the nonstationary nature of the signal. As a result of a comparison of wavelet denoising, cepstral prewhitening, and the proposed LPNCC method utilizing actual data as outlined in Chapter 4, it has been confirmed that the proposed method demonstrates exceptional performance in the diagnosis of early defects in weak, non-stationary rolling bearings. Specifically, for the CWRU dataset cases, the diagnostic potential of the proposed method was demonstrated in instances where the compared techniques have proven ineffective The effectiveness of the proposed approach for incipient fault diagnosis within the SNU degradation dataset was also confirmed.

Contribution 3: In-depth study of bearing defect diagnosis as a bridge between physical behavior and observation

This dissertation presents a novel approach to signal generation and fault diagnosis in rolling bearings, based on a deep understanding of the bearing vibration generation mechanism. The proposed approach is designed to address the challenges posed by the nonlinear relationship between the physical status and monitoring data, as well as the uncertainties inherent in the simple but complex structure of these bearings. Through the development of physics-based and data-driven techniques outlined in Chapters 3 and 4, this research demonstrates how an understanding of the physical behavior and monitored data can inform the development of a suitable diagnosis method. The proposed methods represent a significant advancement in the field of bearing failure diagnosis, offering a valuable example for future research in this area.

5.3 Suggestions for Future Research

This doctoral dissertation presents technical advances that have effectively addressed some of the challenges in vibration-based fault diagnosis for rolling element bearings (REBs) in the incipient fault stage. However, there are still several research topics that require further investigation and development to fully realize the potential of the proposed method. These areas of study include further improving the accuracy and robustness of the proposed diagnostic approach, expanding its applicability to different types of bearings and fault modes, and developing new techniques for extracting and interpreting diagnostic information from vibration signals.

Suggestion 1: Utilization of reference models for signal processing and machine learning techniques

The proposed signal model is a valuable tool for the diagnosis of defects in rolling element bearings. These bearings play a critical role in various industries and their proper functioning is essential for the smooth operation of equipment and machinery. However, detecting defects in these bearings can be challenging due to the complexity of their structure and the non-stationary nature of the signals they generate. The proposed signal model addresses these challenges by generating signals with well-defined characteristics that can be used to train data-driven models for accurate diagnosis and prognosis of defects during their incipient stage. This is particularly valuable in light of the large amounts of data typically required for

training these networks; this requirement makes it challenging to experience the necessary number of defects needed to perform effective training. Thus, further research and development of the proposed signal model has the potential to bring about significant improvements in the efficiency and effectiveness of bearing diagnosis and prognosis.

Suggestion 2: Foundation for constructing a digital twin

The ultimate goal of a digital twin is to optimize the operation of a physical model by utilizing the full potential of engineering simulation technology [106–108]. This requires accurately representing the dynamic response of the system and addressing the inherent stochasticity and nonlinearity of real-world signals. By implementing bi-directional data feedback between the model and the actual system, the model's accuracy can be countinuously improved and the gap between theory and practice can be reduced. However, since there are many difficulties in building an accurate physical model of an actual system, building an appropriate equivalent model can be the immediate goal. It is expected that some of these difficulties can be solved by improving the signal model proposed in this study to better simulate the response of the target system. The result will be a physical model that combines practicality with state-of-the-art simulations, enabling optimal performance and maximizing the benefits of the underlying technology. By continuously adapting the model to reflect real-world conditions, a digital twin can serve as a powerful tool for optimizing the operation of complex systems in a variety of industries, from manufacturing and logistics to energy

Suggestion 3: Automated and quantified optimal parameter selection

The proposed LPNCC-SES approach is a promising method for bearing diagnosis under noisy operating conditions. It should be noted that the performance of the proposed method depends on the setting of parameters of the LPNCC extraction process, such as the power-law coefficient; thus, parameters should be optimized in advance. In actual engineering applications, optimal parameter values can be set empirically, otherwise, the initial values can be preset against white Gaussian noise in general. In particular, the diagnosis of the proposed approach was found to be successful in the case of low-SNR and various noisy environments two situations in which the prior methods were found to have difficulty with accurate diagnosis. In addition, the proposed approach was shown to be effective for early failure diagnosis when applied to degradation data. However, it is needed for the proposed method must manually capture the presence of the fault-related signature. For this reason, an automated detection method that uses a quantitative metric should be incorporated into the proposed method in future work.

REFERENCES

[1] Y. Lv, W. Zhao, Z. Zhao, W. Li, and K. K. H. Ng, "Vibration signal-based early fault prognosis: Status quo and applications," *Adv. Eng. Informatics*, vol. 52, no. April, p. 101609, Apr. 2022.

[2] Q. Zhang, Y. Lv, R. Yuan, Z. Li, and H. Li, "A local transient feature extraction method via periodic low rank dynamic mode decomposition for bearing incipient fault diagnosis," *Meas. J. Int. Meas. Confed.*, vol. 203, no. August, p. 111973, 2022.

[3] P. Jieyang, A. Kimmig, W. Dongkun, Z. Niu, F. Zhi, W. Jiahai, X. Liu, and J. Ovtcharova, "A systematic review of data-driven approaches to fault diagnosis and early warning," *J. Intell. Manuf.*, 2022.

[4] N. Tandon and A. Choudhury, "An analytical model for the prediction of the vibration response of rolling element bearings due to a localized defect," *J. Sound Vib.*, vol. 205, no. 3, pp. 275–292, 1997.

[5] R. B. Randall and J. Antoni, "Rolling element bearing diagnostics-A tutorial," *Mech. Syst. Signal Process.*, vol. 25, no. 2, pp. 485–520, 2011.

[6] A. Rai and S. H. Upadhyay, "A review on signal processing techniques utilized in the fault diagnosis of rolling element bearings," *Tribol. Int.*, vol. 96, pp. 289–306, 2016.

[7] G. Y. Lee, M. Kim, Y. J. Quan, M. S. Kim, T. J. Y. Kim, H. S. Yoon, S. Min, D. H. Kim, J. W. Mun, J. W. Oh, I. G. Choi, C. S. Kim, W. S. Chu, J. Yang, B. Bhandari, C. M. Lee, J. B. Ihn, and S. H. Ahn, "Machine health management in smart factory: A review," *J. Mech. Sci. Technol.*, vol. 32, no. 3, pp. 987–1009, 2018.

[8] H. M. Elattar, H. K. Elminir, and A. M. Riad, “Prognostics: a literature review,” *Complex Intell. Syst.*, vol. 2, no. 2, pp. 125–154, 2016.

[9] D. Wang, K. L. Tsui, and Q. Miao, “Prognostics and Health Management: A Review of Vibration Based Bearing and Gear Health Indicators,” *IEEE Access*, vol. 6, pp. 665–676, 2017.

[10] N. Tandon and A. Choudhury, “Review of vibration and acoustic measurement methods for the detection of defects in rolling element bearings,” *Tribol. Int.*, vol. 32, no. 8, pp. 469–480, 1999.

[11] A. Kumar and R. Kumar, “Role of Signal Processing, Modeling and Decision Making in the Diagnosis of Rolling Element Bearing Defect: A Review,” *J. Nondestruct. Eval.*, vol. 38, no. 1, pp. 1–29, 2019.

[12] S. Singh, C. Q. Howard, and C. H. Hansen, “An extensive review of vibration modelling of rolling element bearings with localised and extended defects,” *J. Sound Vib.*, vol. 357, pp. 300–330, 2015.

[13] J. Lee, F. Wu, W. Zhao, M. Ghaffari, L. Liao, and D. Siegel, “Prognostics and health management design for rotary machinery systems - Reviews, methodology and applications,” *Mech. Syst. Signal Process.*, vol. 42, no. 1–2, pp. 314–334, 2014.

[14] A. K. S. Jardine, D. Lin, and D. Banjevic, “A review on machinery diagnostics and prognostics implementing condition-based maintenance,” *Mech. Syst. Signal Process.*, vol. 20, no. 7, pp. 1483–1510, 2006.

[15] J. Antoni, “Cyclic spectral analysis of rolling-element bearing signals: Facts and fictions,” *J. Sound Vib.*, vol. 304, no. 3–5, pp. 497–529, 2007.

[16] Y. Ming, J. Chen, and G. Dong, “Weak fault feature extraction of rolling bearing based on cyclic Wiener filter and envelope spectrum,” *Mech. Syst.*

Signal Process., vol. 25, no. 5, pp. 1773–1785, 2011.

[17] C. S. Park, Y. C. Choi, and Y. H. Kim, "Early fault detection in automotive ball bearings using the minimum variance cepstrum," *Mech. Syst. Signal Process.*, vol. 38, no. 2, pp. 534–548, 2013.

[18] S. Singh, U. G. Köpke, C. Q. Howard, and D. Petersen, "Analyses of contact forces and vibration response for a defective rolling element bearing using an explicit dynamics finite element model," *J. Sound Vib.*, vol. 333, no. 21, pp. 5356–5377, 2014.

[19] P. D. McFadden and J. D. Smith, "Model for the vibration produced by a single point defect in a rolling element bearing," *J. Sound Vib.*, vol. 96, no. 1, pp. 69–82, 1984.

[20] H. Cao, L. Niu, S. Xi, and X. Chen, "Mechanical model development of rolling bearing-rotor systems: A review," *Mech. Syst. Signal Process.*, vol. 102, pp. 37–58, 2018.

[21] D. Brie, "Modelling of the spalled rolling element bearing vibration signal: an overview and some new results," *Mech. Syst. Signal Process.*, vol. 14, no. 3, pp. 353–369, 2000.

[22] P. Borghesani, W. A. Smith, R. B. Randall, J. Antoni, M. El Badaoui, and Z. Peng, "Bearing signal models and their effect on bearing diagnostics," *Mech. Syst. Signal Process.*, vol. 174, no. April, p. 109077, 2022.

[23] C. Kim and R. M. Stern, "Power-Normalized Cepstral Coefficients (PNCC) for Robust Speech Recognition," *IEEE/ACM Trans. Audio Speech Lang. Process.*, vol. 24, no. 7, pp. 1315–1329, 2016.

[24] M. N. K. Tedric A. Harris, *Rolling Bearing Analysis. Essential Concepts of Bearing Technology*. 2006.

[25] M. Zhao, J. Lin, Y. Miao, and X. Xu, “Detection and recovery of fault impulses via improved harmonic product spectrum and its application in defect size estimation of train bearings,” *Meas. J. Int. Meas. Confed.*, vol. 91, pp. 421–439, 2016.

[26] J. Liu and Y. Shao, “Overview of dynamic modelling and analysis of rolling element bearings with localized and distributed faults,” *Nonlinear Dyn.*, vol. 93, no. 4, pp. 1765–1798, 2018.

[27] B. Dolenc, P. Boškoski, and D. Juričić, “Distributed bearing fault diagnosis based on vibration analysis,” *Mech. Syst. Signal Process.*, vol. 66–67, pp. 521–532, 2016.

[28] “ISO 15243:2017 Rolling bearings — Damage and failures — Terms, characteristics and causes,” *International Organization for Standardization*, 2017. [Online]. Available: https://www.iso.org/standard/59619.html.

[29] F. Sadeghi, B. Jalalahmadi, T. S. Slack, N. Raje, and N. K. Arakere, “A review of rolling contact fatigue,” *J. Tribol.*, vol. 131, no. 4, pp. 1–15, 2009.

[30] C. Santus, M. Beghini, I. Bartilotta, and M. Facchini, “Surface and subsurface rolling contact fatigue characteristic depths and proposal of stress indexes,” *Int. J. Fatigue*, vol. 45, pp. 71–81, 2012.

[31] I. El-Thalji and E. Jantunen, “Dynamic modelling of wear evolution in rolling bearings,” *Tribol. Int.*, vol. 84, pp. 90–99, 2015.

[32] N. F. Mohd Yusof and Z. M. Ripin, “Analysis of Surface Parameters and Vibration of Roller Bearing,” *Tribol. Trans.*, vol. 57, no. 4, pp. 715–729, 2014.

[33] J. Liu and Y. Shao, “A new dynamic model for vibration analysis of a ball bearing due to a localized surface defect considering edge topographies,” *Nonlinear Dyn.*, vol. 79, no. 2, pp. 1329–1351, 2015.

[34] A. Moazen Ahmadi, D. Petersen, and C. Howard, “A nonlinear dynamic vibration model of defective bearings - The importance of modelling the finite size of rolling elements,” *Mech. Syst. Signal Process.*, vol. 52–53, no. 1, pp. 309–326, 2015.

[35] I. El-Thalji and E. Jantunen, “A summary of fault modelling and predictive health monitoring of rolling element bearings,” *Mech. Syst. Signal Process.*, vol. 60, pp. 252–272, 2015.

[36] C. S. Sunnersjö, “Varying compliance vibrations of rolling bearings,” *J. Sound Vib.*, vol. 58, no. 3, pp. 363–373, 1978.

[37] P. D. McFadden and J. D. Smith, “Vibration monitoring of rolling element bearings by the high-frequency resonance technique - a review,” *Tribol. Int.*, vol. 17, no. 1, pp. 3–10, 1984.

[38] M. F. While, “Rolling Element Bearing Vibration Transfer Characteristics: Effect of Stiffness.,” *J. Appl. Mech. Trans. ASME*, vol. 46, no. 3, pp. 677–684, 1979.

[39] M. Hamadache, J. H. Jung, J. Park, and B. D. Youn, “A comprehensive review of artificial intelligence-based approaches for rolling element bearing PHM: shallow and deep learning,” *JMST Adv.*, vol. 1, no. 1–2, pp. 125–151, 2019.

[40] W. Zhou, T. G. Habetler, and R. G. Harley, “Bearing condition monitoring methods for electric machines: A general review,” *2007 IEEE Int. Symp. Diagnostics Electr. Mach. Power Electron. Drives, SDEMPED*, pp. 3–6, 2007.

[41] A. Heng, S. Zhang, A. C. C. Tan, and J. Mathew, “Rotating machinery prognostics: State of the art, challenges and opportunities,” *Mech. Syst. Signal Process.*, vol. 23, no. 3, pp. 724–739, 2009.

[42] I. Shin, J. Lee, J. Y. Lee, K. Jung, D. Kwon, B. D. Youn, H. S. Jang, and J. H. Choi, “A Framework for Prognostics and Health Management Applications toward Smart Manufacturing Systems,” *Int. J. Precis. Eng. Manuf. - Green Technol.*, vol. 5, no. 4, pp. 535–554, 2018.

[43] P. Wang, B. D. Youn, and C. Hu, “A generic probabilistic framework for structural health prognostics and uncertainty management,” *Mech. Syst. Signal Process.*, vol. 28, pp. 622–637, 2012.

[44] K. Saini, S. S. Dhami, and Vanraj, “Predictive Monitoring of Incipient Faults in Rotating Machinery: A Systematic Review from Data Acquisition to Artificial Intelligence,” *Arch. Comput. Methods Eng.*, no. 0123456789, 2022.

[45] P. D. McFadden and J. D. Smith, “The vibration produced by multiple point defects in a rolling element bearing,” *J. Sound Vib.*, vol. 98, no. 2, pp. 263–273, 1985.

[46] M. Behzad, A. R. Bastami, and D. Mba, “A new model for estimating vibrations generated in the defective rolling element bearings,” *J. Vib. Acoust. Trans. ASME*, vol. 133, no. 4, pp. 1–8, 2011.

[47] J. Antoni and R. B. Randall, “A stochastic model for simulation and diagnostics of rolling element bearings with localized faults,” *J. Vib. Acoust. Trans. ASME*, vol. 125, no. 3, pp. 282–289, 2003.

[48] J. M. Marín, H. Rubio, J. C. García-Prada, and O. Reinoso, “Modeling and simulation of 5 and 11 DOF ball bearing system with localized defect,” *J. Test. Eval.*, vol. 42, no. 1, 2014.

[49] J. Liu, “A dynamic modelling method of a rotor-roller bearing-housing system with a localized fault including the additional excitation zone,” *J. Sound Vib.*, vol. 469, p. 115144, 2020.

[50] A. P. Patil, B. K. Mishra, and S. P. Harsha, “Raceway defect analysis of rolling element bearing for detecting slip and correlating the force on rolling element with peak acceleration due to impact,” *Measurement*, vol. 179, no. December 2020, p. 109394, 2021.

[51] M. A. Alfares and A. A. Elsharkawy, “Effects of axial preloading of angular contact ball bearings on the dynamics of a grinding machine spindle system,” *J. Mater. Process. Technol.*, vol. 136, no. 1–3, pp. 48–59, 2003.

[52] D. S. Shah and V. N. Patel, “A Review of Dynamic Modeling and Fault Identifications Methods for Rolling Element Bearing,” *Procedia Technol.*, vol. 14, pp. 447–456, 2014.

[53] L. Niu, H. Cao, H. Hou, B. Wu, Y. Lan, and X. Xiong, “Experimental observations and dynamic modeling of vibration characteristics of a cylindrical roller bearing with roller defects,” *Mech. Syst. Signal Process.*, vol. 138, p. 106553, 2020.

[54] Z. Shi, J. Liu, and S. Dong, “A numerical study of the contact and vibration characteristics of a roller bearing with a surface crack,” *Proc. Inst. Mech. Eng. Part L J. Mater. Des. Appl.*, vol. 234, no. 4, pp. 549–563, Apr. 2020.

[55] M. Tadina and M. Boltežar, “Improved model of a ball bearing for the simulation of vibration signals due to faults during run-up,” *J. Sound Vib.*, vol. 330, no. 17, pp. 4287–4301, 2011.

[56] Y. Cao and Y. Altintas, “Modeling of spindle-bearing and machine tool systems for virtual simulation of milling operations,” *Int. J. Mach. Tools Manuf.*, vol. 47, no. 9, pp. 1342–1350, 2007.

[57] J. Liu, Z. Shi, and Y. Shao, “An investigation of a detection method for a subsurface crack in the outer race of a cylindrical roller bearing,” *Eksploat. i*

Niezawodn., vol. 19, no. 2, pp. 211–219, 2017.

[58] R. B. Randall, N. Sawalhi, and M. Coats, "A comparison of methods for separation of deterministic and random signals," *Int. J. Cond. Monit.*, vol. 1, no. 1, pp. 11–19, 2011.

[59] D. L. Donoho, "De-noising by soft-thresholding," *IEEE Trans. Inf. Theory*, vol. 41, no. 3, pp. 613–627, May 1995.

[60] C. Peeters, P. Guillaume, and J. Helsen, "A comparison of cepstral editing methods as signal pre-processing techniques for vibration-based bearing fault detection," *Mech. Syst. Signal Process.*, vol. 91, pp. 354–381, 2017.

[61] A. Moshrefzadeh, A. Fasana, and J. Antoni, "The spectral amplitude modulation: A nonlinear filtering process for diagnosis of rolling element bearings," *Mech. Syst. Signal Process.*, vol. 132, pp. 253–276, 2019.

[62] C. Hu, B. D. Youn, and P. Wang, "Ensemble of data-driven prognostic algorithms with weight optimization and k-fold cross validation," *Proc. ASME Des. Eng. Tech. Conf.*, vol. 3, no. PARTS A AND B, pp. 1023–1032, 2010.

[63] W. Yan, H. Qiu, and N. Iyer, "Feature Extraction for Bearing Prognostics and Health Management (Phm)-a Survey (Preprint) Stinfo Copy Air Force Research Laboratory Materials and Manufacturing Directorate Wright-Patterson Air Force Base, Oh 45433-7750 Air Force Materiel Command United S," 2008.

[64] H. Zhou, X. Huang, G. Wen, Z. Lei, S. Dong, P. Zhang, and X. Chen, "Construction of health indicators for condition monitoring of rotating machinery: A review of the research," *Expert Syst. Appl.*, vol. 203, no. April, p. 117297, 2022.

[65] A. Widodo and B. S. Yang, “Support vector machine in machine condition monitoring and fault diagnosis,” *Mech. Syst. Signal Process.*, vol. 21, no. 6, pp. 2560–2574, 2007.

[66] Y. Yang, D. Yu, and J. Cheng, “A fault diagnosis approach for roller bearing based on IMF envelope spectrum and SVM,” *Meas. J. Int. Meas. Confed.*, vol. 40, no. 9–10, pp. 943–950, 2007.

[67] V. Vakharia, V. K. Gupta, and P. K. Kankar, “A comparison of feature ranking techniques for fault diagnosis of ball bearing,” *Soft Comput.*, vol. 20, no. 4, pp. 1601–1619, 2016.

[68] J. Zhang, W. Ma, J. Lin, L. Ma, and X. Jia, “Fault diagnosis approach for rotating machinery based on dynamic model and computational intelligence,” *Meas. J. Int. Meas. Confed.*, vol. 59, pp. 73–87, 2015.

[69] M. Hu, G. Wang, K. Ma, Z. Cao, and S. Yang, “Bearing performance degradation assessment based on optimized EWT and CNN,” *Meas. J. Int. Meas. Confed.*, vol. 172, no. December 2020, p. 108868, 2021.

[70] A. Rai and J. M. Kim, “A Novel Health Indicator Based on Information Theory Features for Assessing Rotating Machinery Performance Degradation,” *IEEE Trans. Instrum. Meas.*, vol. 69, no. 9, pp. 6982–6994, 2020.

[71] M. Amar, I. Gondal, and C. Wilson, “Vibration spectrum imaging: A novel bearing fault classification approach,” *IEEE Trans. Ind. Electron.*, vol. 62, no. 1, pp. 494–502, 2015.

[72] X. Wen, G. Lu, J. Liu, and P. Yan, “Graph modeling of singular values for early fault detection and diagnosis of rolling element bearings,” *Mech. Syst. Signal Process.*, vol. 145, p. 106956, 2020.

[73] J. Singh, M. Azamfar, F. Li, and J. Lee, “A systematic review of machine learning algorithms for prognostics and health management of rolling element bearings: fundamentals, concepts and applications,” *Meas. Sci. Technol.*, vol. 32, no. 1, 2021.

[74] F. Jia, Y. Lei, J. Lin, X. Zhou, and N. Lu, “Deep neural networks: A promising tool for fault characteristic mining and intelligent diagnosis of rotating machinery with massive data,” *Mech. Syst. Signal Process.*, vol. 72–73, pp. 303–315, 2016.

[75] R. B. Randall, “A history of cepstrum analysis and its application to mechanical problems,” *Mech. Syst. Signal Process.*, vol. 97, pp. 3–19, 2017.

[76] Y. Kim, J. M. Ha, K. Na, J. Park, and B. D. Youn, “Cepstrum-assisted empirical wavelet transform (CEWT)-based improved demodulation analysis for fault diagnostics of planetary gearboxes,” *Meas. J. Int. Meas. Confed.*, vol. 183, no. March, 2021.

[77] R. B. Randall, “State of the art in monitoring rotating machinery,” *Proc. 2002 Int. Conf. Noise Vib. Eng. ISMA*, no. March, pp. 1457–1477, 2002.

[78] I. Howard, “A review of rolling element bearing vibration ‘detection, diagnosis and prognosis,’” 1994.

[79] J. Antoni, “Cyclostationarity by examples,” *Mech. Syst. Signal Process.*, vol. 23, no. 4, pp. 987–1036, 2009.

[80] W. A. Gardner, A. Napolitano, and L. Paura, “Cyclostationarity: Half a century of research,” *Signal Processing*, vol. 86, no. 4, pp. 639–697, 2006.

[81] R. B. Randall, J. Antoni, and S. Chobsaard, “The relationship between spectral correlation and envelope analysis in the diagnostics of bearing faults and other cyclostationary machine signals,” *Mech. Syst. Signal Process.*, vol.

15, no. 5, pp. 945–962, 2001.

[82] Z. Mo, J. Wang, H. Zhang, and Q. Miao, “Weighted Cyclic Harmonic-to-Noise Ratio for Rolling Element Bearing Fault Diagnosis,” *IEEE Trans. Instrum. Meas.*, vol. 69, no. 2, pp. 432–442, 2020.

[83] J. Antoni, F. Bonnardot, A. Raad, and M. El Badaoui, “Cyclostationary modelling of rotating machine vibration signals,” *Mech. Syst. Signal Process.*, vol. 18, no. 6, pp. 1285–1314, 2004.

[84] C. Mishra, A. K. Samantaray, and G. Chakraborty, “Ball bearing defect models: A study of simulated and experimental fault signatures,” *J. Sound Vib.*, vol. 400, pp. 86–112, 2017.

[85] S. Khanam, J. K. Dutt, and N. Tandon, “Impact force based model for bearing local fault identification,” *J. Vib. Acoust. Trans. ASME*, vol. 137, no. 5, pp. 1–13, 2015.

[86] S. Sassi, B. Badri, and M. Thomas, “A numerical model to predict damaged bearing vibrations,” *JVC/Journal Vib. Control*, vol. 13, no. 11, pp. 1603–1628, 2007.

[87] H. Zhang, P. Borghesani, W. A. Smith, R. B. Randall, M. R. Shahriar, and Z. Peng, “Tracking the natural evolution of bearing spall size using cyclic natural frequency perturbations in vibration signals,” *Mech. Syst. Signal Process.*, vol. 151, p. 107376, 2021.

[88] H. M. Lankarani and P. E. Nikravesh, “Continuous contact force models for impact analysis in multibody systems,” *Nonlinear Dyn.*, vol. 5, no. 2, pp. 193–207, 1994.

[89] J. Zhang, W. Li, L. Zhao, and G. He, “A continuous contact force model for impact analysis in multibody dynamics,” *Mech. Mach. Theory*, vol. 153, 2020.

[90] P. Borghesani, P. Pennacchi, R. B. Randall, N. Sawalhi, and R. Ricci, “Application of cepstrum pre-whitening for the diagnosis of bearing faults under variable speed conditions,” *Mech. Syst. Signal Process.*, vol. 36, no. 2, pp. 370–384, 2013.

[91] L. Rabiner and R. Schafer, *Theory and applications of digital speech processing*. Prentice Hall Press, 2010.

[92] Y. T. Sheen, “An analysis method for the vibration signal with amplitude modulation in a bearing system,” *J. Sound Vib.*, vol. 303, no. 3–5, pp. 538–552, 2007.

[93] C. Kim and R. M. Stern, “Nonlinear enhancement of onset for robust speech recognition,” *Proc. 11th Annu. Conf. Int. Speech Commun. Assoc. INTERSPEECH 2010*, no. September, pp. 2058–2061, 2010.

[94] R. Sousa, J. Antunes, F. Coutinho, E. Silva, J. Santos, and H. Ferreira, “Robust cepstral-based features for anomaly detection in ball bearings,” *Int. J. Adv. Manuf. Technol.*, vol. 103, no. 5–8, pp. 2377–2390, 2019.

[95] Kamil Wojcicki, “Triangular Filterbank,” *MATLAB Central File Exchange*, 2021. .

[96] C. Leys, C. Ley, O. Klein, P. Bernard, and L. Licata, “Detecting outliers: Do not use standard deviation around the mean, use absolute deviation around the median,” *J. Exp. Soc. Psychol.*, vol. 49, no. 4, pp. 764–766, 2013.

[97] A. Mauricio, W. A. Smith, R. B. Randall, J. Antoni, and K. Gryllias, “Improved Envelope Spectrum via Feature Optimisation-gram (IESFOgram): A novel tool for rolling element bearing diagnostics under non-stationary operating conditions,” *Mech. Syst. Signal Process.*, vol. 144, p. 106891, 2020.

[98] K. A. Loparo, “Case Western Reserve University Bearing Data Center,”

Bearings Vibration Data Sets, Case Western Reserve University, 2012. .

[99] W. A. Smith and R. B. Randall, “Rolling element bearing diagnostics using the Case Western Reserve University data: A benchmark study,” *Mech. Syst. Signal Process.*, vol. 64–65, pp. 100–131, 2015.

[100] A. Moshrefzadeh and A. Fasana, “The Autogram: An effective approach for selecting the optimal demodulation band in rolling element bearings diagnosis,” *Mech. Syst. Signal Process.*, vol. 105, pp. 294–318, 2018.

[101] H. Wang, K. Chen, and L. Lin, “Bearing fault diagnosis based on the active energy conversion of generalized stochastic resonance in fluctuating-frequency linear oscillator,” *Meas. Sci. Technol.*, vol. 32, no. 12, 2021.

[102] Q. Ni, J. C. Ji, K. Feng, and B. Halkon, “A fault information-guided variational mode decomposition (FIVMD) method for rolling element bearings diagnosis,” *Mech. Syst. Signal Process.*, vol. 164, no. May 2021, 2022.

[103] J. H. Lee, “A weighting function for improvement of spectral coherence based envelope spectrum,” *Mech. Syst. Signal Process.*, vol. 160, p. 107929, 2021.

[104] S. J. Kim, K. Kim, T. Hwang, J. Park, H. Jeong, T. Kim, and B. D. Youn, “Motor-current-based electromagnetic interference de-noising method for rolling element bearing diagnosis using acoustic emission sensors,” *Meas. J. Int. Meas. Confed.*, vol. 193, no. February, p. 110912, 2022.

[105] E. Sutrisno, H. Oh, A. S. S. Vasan, and M. Pecht, “Estimation of remaining useful life of ball bearings using data driven methodologies,” *PHM 2012 - 2012 IEEE Int. Conf.on Progn. Heal. Manag. Enhancing Safety, Effic. Availability, Eff. Syst. Through PHM Technol. Appl. Conf. Progr.*, vol. 2, pp.

1–7, 2012.

[106] F. Tao, M. Zhang, Y. Liu, and A. Y. C. Nee, “Digital twin driven prognostics and health management for complex equipment,” *CIRP Ann.*, vol. 67, no. 1, pp. 169–172, 2018.

[107] F. Peng, L. Zheng, Y. Peng, C. Fang, and X. Meng, “Digital Twin for rolling bearings: A review of current simulation and PHM techniques,” *Meas. J. Int. Meas. Confed.*, vol. 201, no. July, p. 111728, 2022.

[108] P. Aivaliotis, K. Georgoulias, Z. Arkouli, and S. Makris, “Methodology for enabling digital twin using advanced physics-based modelling in predictive maintenance,” *Procedia CIRP*, vol. 81, pp. 417–422, 2019.

국문 초록

진동 생성 메커니즘을 고려한 초기 결함 단계의 베어링 진단 연구

구름 베어링은 회전 기계 및 왕복동 기계의 핵심적인 요소부품으로 회전하거나 진동하는 구조를 지지하며 구성품 간의 하중을 전달한다. 따라서 구름 베어링의 고장은 시스템 전체의 고장으로 이어져 치명적인 인명 피해는 물론 막대한 재정적 손실을 초래할 수 있다. 이에 따라 조기에 베어링의 고장을 관측하고 진단하기 위해 상태관측 데이터를 활용한 많은 연구가 진행되어 왔으며 특히 진동신호를 활용한 진단이 널리 수행되었다. 베어링 초기 결함을 진단을 하는데 있어 어려움을 겪게 하는 이유로 환경 영향으로 인해 발생하는 잡음에 묻혀 있는 약한 결함 신호 및 베어링의 결함 관련 신호의 복잡한 변조를 들 수있다. 이러한 문제를 극복하기 위해 본 연구에서는 베어링 결함신호의 생성원리에에 기반한 신호 모델을 제안하였다. 베어링 신호는 본질적으로 비정상성을 띄며 또한 실제 현장에서 획득한 신호는 복잡하고 다양한 소스에서 발생하는 신호가 조합된다. 이론과 현실 사이의 격차를 해소하기 위해 해석적 신호 모델에 헤르츠 접촉 이론에 기반한 충격 메커니즘을 구현하였다. 시뮬레이션된 베어링 신호에

기어의 결정론적 신호, 회전축의 사인파 신호 및 가우시안 노이즈와 합성된 신호에 대한 전처리 분석을 통해 제안 모델의 타당성을 검증하였다. 이 후, 다양한 잡음 환경에서 여러 변조된 음성 신호를 효과적으로 판별하는 음성인식 방법을 기계시스템에 적용한 고장특징 추출 방법을 새로이 제안하여 캡스트럼에 기반한 특징인자를 추출하였다. 추출된 인자로부터 시간-주파수 영역에서 스펙트럼을 계산하여 효과적으로 베어링의 특성 주파수를 검출하였다. 제안된 방법의 검증을 위해 다양한 잡음 환경에서의 시뮬레이션 데이터와 실험데이터를 사용하였다. 또한 가속수명시험을 통한 데이터를 통하여 조기진단의 효과를 검증하였다.

주요어: 구름베어링
신호모델링
베어링 고장진단
진동생성메커니즘
조기결함

학 번: 2013-20646